

# **Introduction to Gravitational Lensing**

**With python examples**

**Massimo Meneghetti**

Copyright © 2017 Massimo Meneghetti

PUBLISHED BY MASSIMO MENEGHETTI

[HTTP://PICO.BO.ASTRO.IT/MASSIMO/TEACHING.HTML](http://PICO.BO.ASTRO.IT/MASSIMO/TEACHING.HTML)

Licensed under the Creative Commons Attribution-NonCommercial 3.0 Unported License (the “License”). You may not use this file except in compliance with the License. You may obtain a copy of the License at <http://creativecommons.org/licenses/by-nc/3.0>. Unless required by applicable law or agreed to in writing, software distributed under the License is distributed on an “AS IS” BASIS, WITHOUT WARRANTIES OR CONDITIONS OF ANY KIND, either express or implied. See the License for the specific language governing permissions and limitations under the License.

*First printing, March 2017*

# Contents

Part One: Generalities		
<b>1</b>	<b>Light deflection .....</b>	<b>9</b>
1.1	Deflection of a light corpuscle .....	9
1.2	Deflection of light according to General Relativity .....	11
1.2.1	Fermat principle and light deflection .....	11
1.2.2	Deflection of light in the strong field limit .....	17
1.3	Deflection by an ensemble of point masses .....	17
1.4	Deflection by an extended mass distribution .....	18
1.5	Python applications .....	19
1.5.1	Deflection by a black-hole .....	19
1.5.2	Deflection by an extended mass distribution .....	22
1.6	Problems .....	26
<b>2</b>	<b>The general lens .....</b>	<b>29</b>
2.1	Lens equation .....	29
2.2	Lensing potential .....	31
2.3	First order lens mapping .....	33
2.4	Magnification .....	37
2.5	Lensing to the second order .....	37
2.5.1	Complex notation .....	38
2.6	Occurrence of images .....	39

<b>2.7</b>	<b>Python applications</b>	<b>42</b>
2.7.1	Implementing a ray-tracing algorithm .....	42
2.7.2	Derivation of the lensing potential .....	44
<b>2.8</b>	<b>To be done</b>	<b>46</b>

## II

## Part Two: Applications

<b>3</b>	<b>Microlensing</b> .....	<b>49</b>
3.1	The point mass lens .....	49
3.2	<b>Microlensing light-curve</b>	53
3.2.1	Light-curve fitting .....	55
3.3	<b>Photometric microlensing: optical depth and event rates</b>	56
3.3.1	Optical depth .....	56
3.3.2	Event rate .....	59
3.4	<b>Astrometric microlensing</b>	60
3.5	<b>Multiple point masses</b>	65
3.5.1	Generalities .....	65
3.5.2	Binary lenses .....	67
3.6	<b>Planetary microlensing</b>	71
3.7	<b>Python applications</b>	76
3.7.1	Standard microlensing light curve .....	76
3.7.2	Fitting the standard light curve .....	79
3.7.3	Astrometric microlensing effect .....	84
3.7.4	Critical lines and caustics of a binary lens .....	84
3.7.5	Solving the lens equation of the binary lens .....	84
3.7.6	Light curve in a binary microlensing event .....	84
3.8	<b>Planetary microlensing</b>	84
<b>4</b>	<b>Extended lenses</b> .....	<b>85</b>
4.1	<b>Axially symmetric lenses</b>	85
4.2	<b>Power-law lens</b>	90
4.2.1	Lenses with $1 < n < 2$ .....	90
4.2.2	Lenses with $n > 2$ .....	94
4.2.3	Singular Isothermal Sphere .....	95
4.3	<b>Softened (Isothermal) Lenses</b>	97
4.4	<b>Time delays</b>	101
4.5	<b>Other profiles</b>	103
4.5.1	The Navarro-Frenk-White model .....	103
4.5.2	The Pseudo-Isothermal model .....	106
4.6	<b>Elliptical lenses</b>	106
4.6.1	Singular Isothermal Ellipsoid .....	106
4.6.2	Non-singular elliptical models .....	110
4.6.3	Pseudo-elliptical models .....	111

<b>4.7</b>	<b>Environment</b>	<b>111</b>
<b>4.8</b>	<b>Substructures</b>	<b>112</b>
<b>4.9</b>	<b>Mass-sheet degeneracy</b>	<b>112</b>
<b>4.10</b>	<b>Python applications</b>	<b>112</b>
4.10.1	Multiple images by SIE lenses .....	112
4.10.2	Images of extended sources .....	112
	<b>Bibliography .....</b>	<b>113</b>
	<b>Index .....</b>	<b>115</b>
<b>A</b>	<b>Python tutorial .....</b>	<b>115</b>
<b>A.1</b>	<b>Installation</b>	<b>115</b>
<b>A.2</b>	<b>Documentation</b>	<b>115</b>
<b>A.3</b>	<b>Running python</b>	<b>115</b>
<b>A.4</b>	<b>Your first python code</b>	<b>116</b>
<b>A.5</b>	<b>Variables</b>	<b>116</b>
<b>A.6</b>	<b>Strings</b>	<b>116</b>
<b>A.7</b>	<b>Lists</b>	<b>117</b>
<b>A.8</b>	<b>Tuples</b>	<b>117</b>
<b>A.9</b>	<b>Dictionaries</b>	<b>118</b>
<b>A.10</b>	<b>Blocks and Indentation</b>	<b>118</b>
<b>A.11</b>	<b>IF / ELIF / ELSE</b>	<b>118</b>
<b>A.12</b>	<b>While loops</b>	<b>118</b>
<b>A.13</b>	<b>For loops</b>	<b>119</b>
<b>A.14</b>	<b>Functions</b>	<b>119</b>
<b>A.15</b>	<b>Classes</b>	<b>119</b>
<b>A.16</b>	<b>Modules</b>	<b>121</b>
<b>A.17</b>	<b>Importing packages</b>	<b>121</b>





# Part One: Generalities

<b>1</b>	<b>Light deflection .....</b>	<b>9</b>
1.1	Deflection of a light corpuscle	
1.2	Deflection of light according to General Relativity	
1.3	Deflection by an ensemble of point masses	
1.4	Deflection by an extended mass distribution	
1.5	Python applications	
1.6	Problems	
<b>2</b>	<b>The general lens .....</b>	<b>29</b>
2.1	Lens equation	
2.2	Lensing potential	
2.3	First order lens mapping	
2.4	Magnification	
2.5	Lensing to the second order	
2.6	Occurrence of images	
2.7	Python applications	
2.8	To be done	



# 1. Light deflection

## 1.1 Deflection of a light corpuscle

The idea that light could be bent by gravity was mentioned by Isaac Newton in a note at the end of *Optiks*, published in 1704. Further calculations were made about a century later by the German astronomer Johann Georg Von Soldner (1776-1833), who ended up quantifying that the deflection of a photon grazing the surface of the sun would amount to about 0.9".

What were the assumptions under which this result was obtained? We should first of all introduce the framework within which the idea was proposed. This is the so called "Corpuscular Theory of Light", which assumes that photons are not mass-less.

In this framework, the derivation of the deflection angle of a photon by a body with mass  $M$  is rather straightforward. It can be done in many ways, but we re-propose here a simple calculation by Victor J. Stenger (2013), which is based on four ingredients:

- Newton's law of gravity;
- Newton's second law of motion;
- Einstein's principle of equivalence;
- Einstein's special relativity.

Newton's law of gravity says that the gravitational force between two bodies with masses  $m$  and  $M$  is

$$\vec{F} = \frac{GmM}{r^3} \vec{r}, \quad (1.1)$$

where  $r$  is the distance between the bodies, and  $G$  is the gravitational constant.

Newton's second law of motion states that

$$\vec{F} = \frac{d\vec{p}}{dt} = m\vec{a} \quad (1.2)$$

where  $\vec{p}$  and  $\vec{a}$  are the momentum and the acceleration of the body with inertial mass  $m$ , respectively.

Because of the principle of equivalence, the gravitational mass  $m$  in Eq. 1.1 equals the inertial mass  $m$  in Eq. 1.2.

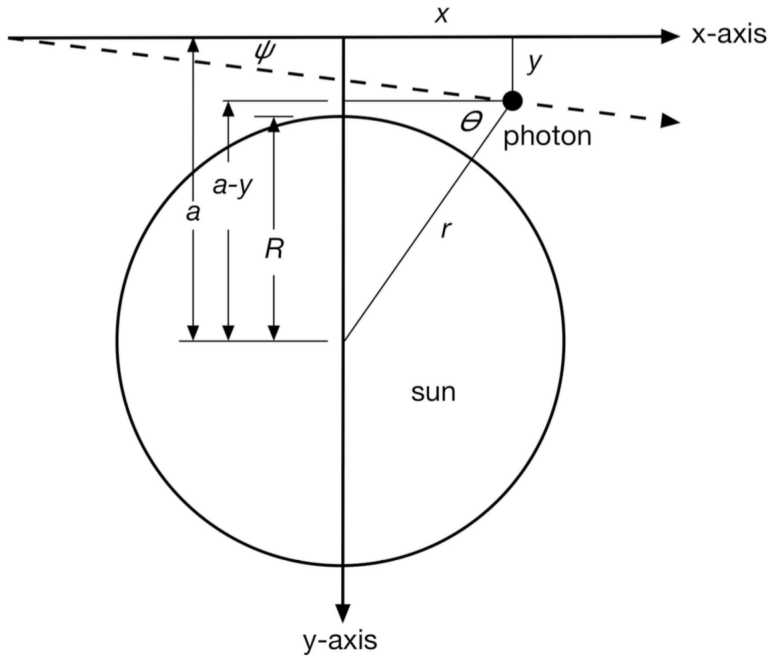


**Figure 1.1.1:** Schematic view of a photon grazing the surface of the Sun (from V. J. Stenger, 2013).

From Einstein's special relativity, we have that the inertial mass of a photon with energy  $E$  is  $E/c^2$ , where  $c$  is the speed of light.

Let assume that a photon with initial momentum  $\vec{p}$  grazes the surface of the Sun, as shown in Fig. 1.1.1. The photon travels along the  $x$ -axis, while the  $y$ -axis was chosen to pass through the center of the sun, whose mass is  $M$  and whose radius is  $R$ . Let  $a$  be the impact parameter of the photon, i.e. the minimal distance of the un-deflected trajectory of the photon from the center of the Sun. When the photon is at the position  $(x, y)$ , the distance from the Sun is

$$r = \sqrt{x^2 + (a - y)^2}. \quad (1.3)$$

Let's assume that the momentum of the photon does not change significantly along its path. The components of the gravitational force acting on the photon are

$$\begin{aligned} F_x &= \frac{dp}{dt} \cos \theta &= \frac{G M p}{c[x^2 + (a - y)^2]} \cos \theta = \frac{G M p}{c} \frac{x}{[x^2 + (a - y)^2]^{3/2}}, \\ F_y &= \frac{dp}{dt} \sin \theta &= \frac{G M p}{c[x^2 + (a - y)^2]} \sin \theta = \frac{G M p}{c} \frac{a - y}{[x^2 + (a - y)^2]^{3/2}}. \end{aligned} \quad (1.4)$$

Now, let's assume that  $dx = c dt$ . We can then write:

$$\frac{dp_i}{dt} = \frac{dp_i}{dx} \frac{dx}{dt} = c \frac{dp_i}{dx}, \quad (1.5)$$

which allows to re-write Eqs. 1.4 as

$$\begin{aligned} \frac{dp_x}{dx} &= \frac{G M p}{c^2} \frac{x}{[x^2 + (a - y)^2]^{3/2}}, \\ \frac{dp_y}{dx} &= \frac{G M p}{c^2} \frac{a - y}{[x^2 + (a - y)^2]^{3/2}}. \end{aligned} \quad (1.6)$$

These equations allow us to calculate by how much does the momentum change along the  $x$  and the  $y$  axes as the  $x$  coordinate of the photon changes. Along the  $x$ -axis:

$$\Delta p_x = \frac{G M p}{c^2} \int_{-\infty}^{\infty} \frac{x}{[x^2 + (a-y)^2]^{3/2}} dx = 0. \quad (1.7)$$

Thus, the photon momentum is un-changed along the  $x$ -axis. On the contrary, along the  $y$ -axis, the photon momentum changes by

$$\begin{aligned} \Delta p_y &= \frac{G M p}{c^2} \int_{-\infty}^{\infty} \frac{a-y}{[x^2 + (a-y)^2]^{3/2}} dx \\ &= \frac{G M p}{c^2} \left[ \frac{x}{(a-y) \sqrt{x^2 + (a-y)^2}} \right]_{-\infty}^{+\infty} \\ &= \frac{2 G M p}{c^2} \frac{1}{a-y}, \end{aligned} \quad (1.8)$$

which can be used to compute the deflection angle

$$\psi = \frac{\Delta p_y}{p} = \frac{2 G M}{c^2} \frac{1}{a-y}. \quad (1.9)$$

If the photon impact parameter is  $a - y = R_\odot$ , Eq. 1.9 reduces to

$$\psi = \frac{\Delta p_y}{p} = \frac{2 G M}{c^2 R_\odot} \approx 0.875'', \quad (1.10)$$

when inserting  $M = M_\odot = 1.989 \times 10^{30}$  kg and  $R_\odot = 6.96 \times 10^8$  m. Thus, using Newtonian gravity and assuming that photons are light corpuscles, we obtain that a photon grazing the surface of the Sun is deflected by  $0.875''$ . We will see shortly that this value is just half of what predicted by Einstein in the framework of his Theory of General Relativity.

## 1.2 Deflection of light according to General Relativity

### 1.2.1 Fermat principle and light deflection

Starting from the field equations of general relativity, light deflection can be calculated by studying geodesic curves. It turns out that light deflection can equivalently be described by Fermat's principle, as in geometrical optics. This will be our starting point.

**Exercise 1.1 — Derive the Snell's law from Fermat principle.** In its simplest form the Fermat's principle says that light waves of a given frequency traverse the path between two points which takes the least time. The speed of light in a medium with refractive index  $n$  is  $c/n$ , where  $c$  is its speed in a vacuum. Thus, the time required for light to go some distance in such a medium is  $n$  times the time light takes to go the same distance in a vacuum.

Referring to Fig. 1.2.1, the time required for light to go from A to B becomes

$$t = [\{h_1^2 + y^2\}^{1/2} + n\{h_2^2 + (w-y)^2\}^{1/2}]/c.$$

We find the minimum time by differentiating  $t$  with respect to  $y$  and setting the result to zero, with the result that

$$\frac{y}{\{h_1^2 + y^2\}^{1/2}} = n \frac{w-y}{\{h_2^2 + (w-y)^2\}^{1/2}}.$$

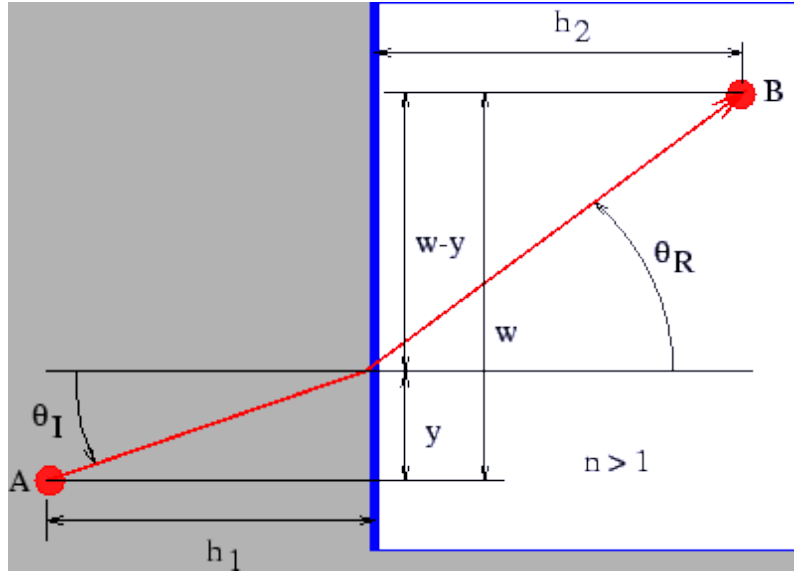


**Figure 1.2.1:** Definition sketch for deriving Snell's law of refraction from Fermat's principle. The shaded area has refractive index  $n > 1$

However, we note that the left side of this equation is simply  $\sin \theta_I$ , while the right side is  $n \sin \theta_R$ , so that the minimum time condition reduces to

$$\sin \theta_I = n \sin \theta_R$$

We recognize this result as Snell's law. ■

Taking inspiration from the Exercise above, we attempt to treat the deflection of light in a general relativity framework as a refraction problem. We need an refractive index  $n$  because Fermat's principle says that light will follow the path which makes extremal the travel time,

$$t_{\text{travel}} = \int \frac{n}{c} dl . \quad (1.11)$$

As in geometrical optics, we thus search for the path,  $\vec{x}(l)$ , for which

$$\delta \int_A^B n(\vec{x}(l)) dl = 0 , \quad (1.12)$$

where the starting point  $A$  and the end point  $B$  are kept fixed.



### Deflection in the Minkowski's space-time

In order to find the refractive index, we make a first approximation: we assume that the lens is weak, and that it is small compared to the overall dimensions of the optical system composed of source, lens and observer. With "weak lens", we mean a lens whose Newtonian gravitational potential  $\Phi$  is much smaller than  $c^2$ ,  $\Phi/c^2 \ll 1$ . Note that this approximation is valid in virtually all

cases of astrophysical interest. Consider for instance a galaxy cluster: its gravitational potential is  $|\Phi| < 10^{-4}c^2 \ll c^2$ . In addition, we also assume that the light deflection occurs in a region which is small enough that we can neglect the expansion of the universe.

In this case, the metric of (locally flat) unperturbed space-time is the Minkowski metric,

$$\eta_{\mu\nu} = \begin{pmatrix} 1 & 0 & 0 & 0 \\ 0 & -1 & 0 & 0 \\ 0 & 0 & -1 & 0 \\ 0 & 0 & 0 & -1 \end{pmatrix},$$

whose line element is

$$ds^2 = \eta_{\mu\nu} dx^\mu dx^\nu = (dx^0)^2 - (d\vec{x})^2 = c^2 dt^2 - (d\vec{x})^2. \quad (1.13)$$

Now, we consider a weak lens perturbing this metric, such that

$$\eta_{\mu\nu} \rightarrow g_{\mu\nu} = \begin{pmatrix} 1 + \frac{2\Phi}{c^2} & 0 & 0 & 0 \\ 0 & -(1 - \frac{2\Phi}{c^2}) & 0 & 0 \\ 0 & 0 & -(1 - \frac{2\Phi}{c^2}) & 0 \\ 0 & 0 & 0 & -(1 - \frac{2\Phi}{c^2}) \end{pmatrix}$$

for which the line element becomes

$$ds^2 = g_{\mu\nu} dx^\mu dx^\nu = \left(1 + \frac{2\Phi}{c^2}\right) c^2 dt^2 - \left(1 - \frac{2\Phi}{c^2}\right) (d\vec{x})^2. \quad (1.14)$$

**■ Example 1.1 — Schwarzschild metric in the weak field limit.** Assuming a spherically symmetric and static potential, the Einstein's field equations can be solved to obtain the *Schwarzschild metric*. The line element is written in spherical coordinates as

$$ds^2 = \left(1 - \frac{2GM}{Rc^2}\right) c^2 dt^2 - \left(1 - \frac{2GM}{Rc^2}\right)^{-1} dR^2 - R^2 (\sin^2 \theta d\phi^2 + d\theta^2).$$

To obtain a simpler expression, it is convenient to introduce the new radial coordinate  $r$ , defined through

$$R = r \left(1 + \frac{GM}{2rc^2}\right)^2$$

and the cartesian coordinates  $x = r \sin \theta \cos \theta$ ,  $y = r \sin \theta \sin \phi$ , and  $z = r \cos \theta$ , so that  $dl^2 = dx^2 + dy^2 + dz^2$ . After some algebra, the metric can then be written in the form

$$ds^2 = \left(\frac{1 - GM/2rc^2}{1 + GM/2rc^2}\right)^2 c^2 dt^2 - \left(1 + \frac{GM}{2rc^2}\right)^4 (dx^2 + dy^2 + dz^2).$$

In the weak field limit,  $\Phi/c^2 = -GM/rc^2 \ll 1$ ,

$$\begin{aligned} \left(\frac{1 - GM/2rc^2}{1 + GM/2rc^2}\right)^2 &\approx \left(1 - \frac{GM}{2rc^2}\right)^4 \\ &\approx \left(1 - \frac{2GM}{rc^2}\right) \\ &= \left(1 + \frac{2\Phi}{c^2}\right) \end{aligned}$$

and

$$\begin{aligned} \left(1 + \frac{GM}{2rc^2}\right)^4 &\approx \left(1 + 2\frac{GM}{rc^2}\right) \\ &= \left(1 - \frac{2\Phi}{c^2}\right). \end{aligned}$$

Therefore, the Schwarzschild metric in the weak field limit equals

$$ds^2 = \left(1 + \frac{2\Phi}{c^2}\right) c^2 dt^2 - \left(1 - \frac{2\Phi}{c^2}\right) dl^2,$$

thus recovering Eq. 1.14. ■

### Effective refractive index

Light propagates at zero eigentime,  $ds = 0$ , from which we obtain

$$\left(1 + \frac{2\Phi}{c^2}\right) c^2 dt^2 = \left(1 - \frac{2\Phi}{c^2}\right) (d\vec{x})^2. \quad (1.15)$$

The light speed in the gravitational field is thus

$$c' = \frac{|d\vec{x}|}{dt} = c \sqrt{\frac{1 + \frac{2\Phi}{c^2}}{1 - \frac{2\Phi}{c^2}}} \approx c \left(1 + \frac{2\Phi}{c^2}\right), \quad (1.16)$$

where we have used that  $\Phi/c^2 \ll 1$  by assumption. The refractive index is thus

$$n = c/c' = \frac{1}{1 + \frac{2\Phi}{c^2}} \approx 1 - \frac{2\Phi}{c^2}. \quad (1.17)$$

With  $\Phi \leq 0$ ,  $n \geq 1$ , and the light speed  $c'$  is smaller than in absence of the gravitational potential.

### Deflection angle

The refractive index  $n$  depends on the spatial coordinate  $\vec{x}$  and perhaps also on time  $t$ . Let  $\vec{x}(l)$  be a light path. Then, the light travel time is

$$t_{travel} \propto \int_A^B n[\vec{x}(l)] dl, \quad (1.18)$$

and the light path follows from

$$\delta \int_A^B n[\vec{x}(l)] dl = 0. \quad (1.19)$$

This is a standard variational problem, which leads to the well known Euler equations. In our case we write

$$dl = \left| \frac{d\vec{x}}{d\lambda} \right| d\lambda, \quad (1.20)$$

with a curve parameter  $\lambda$  which is yet arbitrary, and find

$$\delta \int_{\lambda_A}^{\lambda_B} d\lambda n[\vec{x}(\lambda)] \left| \frac{d\vec{x}}{d\lambda} \right| = 0 \quad (1.21)$$

The expression

$$n[\vec{x}(\lambda)] \left| \frac{d\vec{x}}{d\lambda} \right| \equiv L(\dot{\vec{x}}, \vec{x}, \lambda) \quad (1.22)$$

takes the role of the Lagrangian, with

$$\dot{\vec{x}} \equiv \frac{d\vec{x}}{d\lambda}. \quad (1.23)$$

Finally, we have

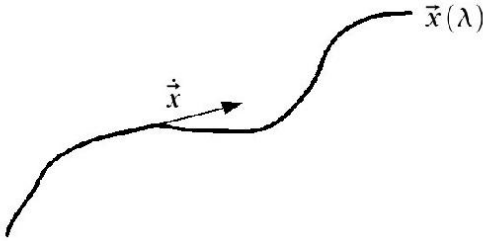
$$\left| \frac{d\vec{x}}{d\lambda} \right| = |\dot{\vec{x}}| = (\dot{\vec{x}}^2)^{1/2}. \quad (1.24)$$

The Euler equation writes:

$$\frac{d}{d\lambda} \frac{\partial L}{\partial \dot{\vec{x}}} - \frac{\partial L}{\partial \vec{x}} = 0. \quad (1.25)$$

Now,

$$\frac{\partial L}{\partial \vec{x}} = |\dot{\vec{x}}| \frac{\partial n}{\partial \vec{x}} = (\vec{\nabla} n) |\dot{\vec{x}}|, \frac{\partial L}{\partial \dot{\vec{x}}} = n \frac{\dot{\vec{x}}}{|\dot{\vec{x}}|}. \quad (1.26)$$



Evidently,  $\dot{\vec{x}}$  is a tangent vector to the light path, which we can assume to be normalized by a suitable choice for the curve parameter  $\lambda$ . We thus assume  $|\dot{\vec{x}}| = 1$  and write  $\vec{e} \equiv \dot{\vec{x}}$  for the unit tangent vector to the light path. Then, we have

$$\frac{d}{d\lambda} (n\vec{e}) - \vec{\nabla} n = 0, \quad (1.27)$$

or

$$n\dot{\vec{e}} + \vec{e} \cdot [(\vec{\nabla} n)\dot{\vec{x}}] = \vec{\nabla} n,$$

$$\Rightarrow n\dot{\vec{e}} = \vec{\nabla} n - \vec{e}(\vec{\nabla} n \cdot \vec{e}). \quad (1.28)$$

The second term on the right hand side is the derivative along the light path, thus the whole right hand side is the gradient of  $n$  perpendicular to the light path. Thus

$$\dot{\vec{e}} = \frac{1}{n} \vec{\nabla}_{\perp} n = \vec{\nabla}_{\perp} \ln n. \quad (1.29)$$

As  $n = 1 - 2\Phi/c^2$  and  $\Phi/c^2 \ll 1$ ,  $\ln n \approx -2\Phi/c^2$ , and

$$\dot{\vec{e}} \approx -\frac{2}{c^2} \vec{\nabla}_{\perp} \Phi. \quad (1.30)$$

The total deflection angle of the light path is now the integral over  $-\dot{\vec{e}}$  along the light path,

$$\hat{\alpha} = \vec{e}_{in} - \vec{e}_{out} = \frac{2}{c^2} \int_{\lambda_A}^{\lambda_B} \vec{\nabla}_{\perp} \Phi d\lambda, \quad (1.31)$$

or, in other words, the integral over the "pull" of the gravitational potential perpendicular to the light path. Note that  $\vec{\nabla}\Phi$  points away from the lens center, so  $\hat{\alpha}$  points in the same direction.

### Born approximation

As it stands, the equation for  $\hat{\alpha}$  is not useful, as we would have to integrate over the actual light path. However, since  $\Phi/c^2 \ll 1$ , we expect the deflection angle to be small. Then, we can adopt the *Born approximation*, familiar from scattering theory, and integrate over the unperturbed light path.

Suppose, therefore, that a light ray starts out into  $+\vec{e}_z$ -direction and passes a lens at  $z = 0$ , with impact parameter  $b$ . The deflection angle is then given by

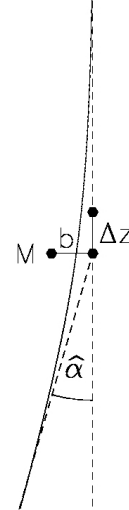
$$\hat{\alpha}(b) = \frac{2}{c^2} \int_{-\infty}^{+\infty} \vec{\nabla}_{\perp} \phi dz \quad (1.32)$$

■ **Example 1.2 — Deflection by a point mass.** If the lens is a point mass, then

$$\Phi = -\frac{GM}{r} \quad (1.33)$$

with  $r = \sqrt{x^2 + y^2 + z^2} = \sqrt{b^2 + z^2}$ ,  $b = \sqrt{x^2 + y^2}$  and

$$\vec{\nabla}_{\perp} \phi = \left( \begin{array}{c} \partial_x \Phi \\ \partial_y \Phi \end{array} \right) = \frac{GM}{r^3} \left( \begin{array}{c} x \\ y \end{array} \right). \quad (1.34)$$



The deflection angle is then

$$\begin{aligned} \hat{\alpha}(b) &= \frac{2GM}{c^2} \left( \begin{array}{c} x \\ y \end{array} \right) \int_{-\infty}^{+\infty} \frac{dz}{(b^2 + z^2)^{3/2}} \\ &= \frac{4GM}{c^2} \left( \begin{array}{c} x \\ y \end{array} \right) \left[ \frac{z}{b^2(b^2 + z^2)^{1/2}} \right]_0^{\infty} \\ &= \frac{4GM}{c^2 b} \left( \begin{array}{c} \cos \phi \\ \sin \phi \end{array} \right), \end{aligned} \quad (1.35)$$

with

$$\left( \begin{array}{c} x \\ y \end{array} \right) = b \left( \begin{array}{c} \cos \phi \\ \sin \phi \end{array} \right) \quad (1.36)$$

Notice that  $R_s = \frac{2GM}{c^2}$  is the Schwarzschild radius of a (point) mass  $M$ , thus

$$|\hat{\alpha}| = \frac{4GM}{c^2 b} = 2 \frac{R_s}{b}. \quad (1.37)$$

Also notice that  $\hat{\alpha}$  is linear in  $M$ , thus the superposition principle can be applied to compute the deflection angle of an ensemble of lenses. ■

### Deflection of light by the Sun's gravitational field

Note that the deflection angle found here in the framework of general relativity is very similar to the result found in the Newtonian limit for a photon grazing the surface of the Sun. However, we find here an extra factor two.

The reason for the factor of 2 difference is that both the space and time coordinates are bent in the vicinity of massive objects — it is four-dimensional space–time which is bent by the Sun.

The famous eclipse expedition of 1919 to Sobral, Brazil, and the island of Principe, in the Gulf of Guinea, led by Eddington, Dyson, and Davidson was a turning point in the history of relativity: it confirmed that masses bend light by the amount that is predicted by General Relativity.

For further reading on the Eddington expedition, we refer the reader to Smith (2015).

### 1.2.2 Deflection of light in the strong field limit

For the vast majority of gravitational lenses in the universe, the weak field limit holds. However, compact objects such as neutron stars and black holes can also act as lenses. In these cases, the approximations introduced above break down, as photons travel through very strong gravitational fields. In the following, we briefly discuss the deflection angle of a static (i.e. non-rotating) compact lens.

For a general static, spherically symmetric metric in the form

$$ds^2 = A(R)dt^2 - B(R)dR^2 - C(R)(d\theta^2 + \sin^2\theta d\phi^2) \quad (1.38)$$

the analysis of the geodesic equations leads to the following expression for the deflection angle:

$$\hat{\alpha} = -\pi + \frac{2G}{c^2} \int_{R_m}^{\infty} u \sqrt{\frac{B(R)}{C(R)[C(R)/A(R) - u^2]}} dR, \quad (1.39)$$

where  $u$  is the impact parameter of the unperturbed photon and  $R_m$  is the minimal distance of the deflected photon from the lens (Bozza, 2010). It can be shown that

$$u^2 = \frac{C(R_m)}{A(R_m)}. \quad (1.40)$$

Note that, in the case of the Schwarzschild metric,  $A(R) = 1 - 2GM/Rc^2$ ,  $B(R) = A(R)^{-1}$ , and  $C(R) = R^2$ .

In the weak field limit ( $R \geq R_m \gg 2GM/c^2$ , i.e. for impact parameters much larger than the lens Schwarzschild radius), Eq. 1.39 reduces to the well known equation

$$\hat{\alpha} = \frac{4GM}{c^2 u}. \quad (1.41)$$

The exact solution of Eq. 1.39 was calculated by Darwin (1959) to be

$$\hat{\alpha} = -\pi + 4 \frac{G}{c^2} \sqrt{R_m/s} F(\varphi, m), \quad (1.42)$$

where  $F(\varphi, m)$  is the elliptic integral of the first kind, and

$$s = \sqrt{(R_m - 2M)(R_m + 6M)} \quad (1.43)$$

$$m = (s - R_m + 6M)/2s \quad (1.44)$$

$$\varphi = \arcsin \sqrt{2s/(3R_m - 6M + s)} \quad (1.45)$$

Fig. 1.2.2 shows how the deflection angle varies as a function of the impact parameter of the photon. At large distances, Eq. 1.42 is well approximated by the solution in the weak field limit. For small impact parameters, the solutions in the strong and in the weak field limit differ significantly. In particular, the deflection angle in Eq. 1.42 diverges for  $u = 3\sqrt{3}GM/c^2$  (or  $R_m = 3GM/c^2$ ). Before reaching that point, the deflection angle exceeds  $2\pi$ , meaning that the photon loops around the lens before leaving it.

## 1.3 Deflection by an ensemble of point masses

The deflection angle in Eq. 1.37 depends linearly on the mass  $M$ . This result was obtained by linearizing the equations of general relativity in the weak field limit. Under these circumstances, the superposition principle holds and the deflection angle of an array of lenses can be calculated as the sum of all contributions by each single lens.

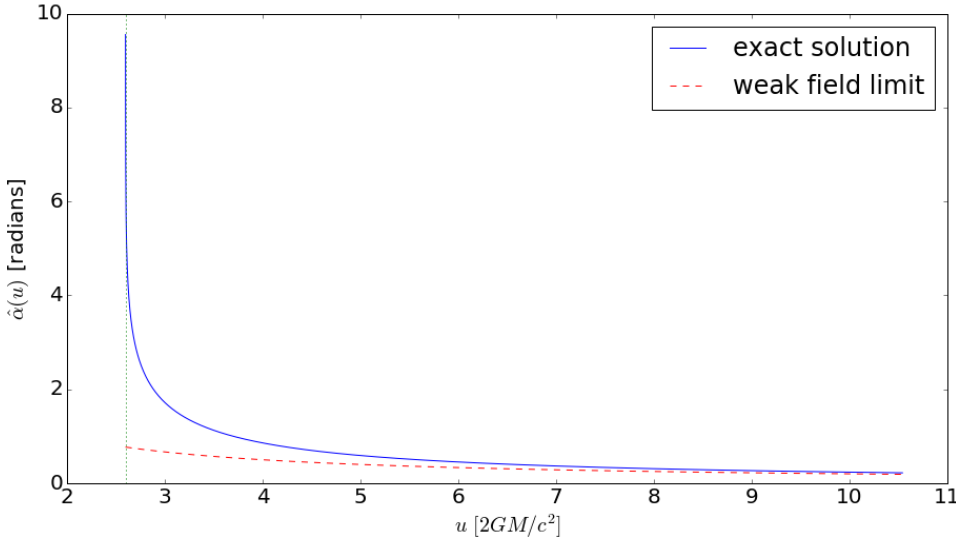


**Figure 1.2.2:** Deflection angle by a compact lens as a function of the photon impact parameter. Shown are the exact solution of the geodesic equations for a Schwarzschild metric (solid line) and the solution in the weak field approximation (dashed line). The dotted vertical line shows the impact parameter,  $u = 3\sqrt{3}GM/c^2$ , for which the exact solution diverges, indicating that the photon keeps looping around the lens.

Suppose we have a sparse distribution of  $N$  point masses on a plane, whose positions and masses are  $\vec{\xi}_i$  and  $M_i$ ,  $1 \leq i \leq N$ . The deflection angle of a light ray crossing the plane at  $\vec{\xi}$  will be:

$$\hat{\alpha}(\vec{\xi}) = \sum_i \hat{\alpha}_i(\vec{\xi} - \vec{\xi}_i) = \frac{4G}{c^2} \sum_i M_i \frac{\vec{\xi} - \vec{\xi}_i}{|\vec{\xi} - \vec{\xi}_i|^2}. \quad (1.46)$$

Note that the formula above is similar to that we would use to compute the gravitational force between point masses on the plane. While the force depends on the inverse squared distance, the deflection angle scales as  $\xi^{-1}$ . In the case of many lenses, the computation of the deflection angle using Eq. 1.46 can become very computationally expensive, as it costs  $O(N^2)$ . However, as it is usually done to solve numerically  $N$ -body problems, algorithms employing meshes or hierarchies (such as the so-called tree algorithms (Barnes and Hut, 1986)) can significantly reduce the cost of calculations (e.g. to  $O(N \log N)$ ). For some application of these algorithms in the computation of the deflection angles, we refer the reader to the works of Aubert, Amara, and Metcalf (2007) and Meneghetti et al. (2010).

## 1.4 Deflection by an extended mass distribution

We now consider more realistic lens models, i.e. three dimensional distributions of matter. Even in the case of lensing by galaxy clusters, the physical size of the lens is generally much smaller than the distances between observer, lens and source. The deflection therefore arises along a very short section of the light path. This justifies the usage of the *thin screen approximation*: the lens is approximated by a planar distribution of matter, the lens plane.

Within this approximation, the lensing matter distribution is fully described by its surface density,

$$\Sigma(\vec{\xi}) = \int \rho(\vec{\xi}, z) dz, \quad (1.47)$$

where  $\vec{\xi}$  is a two-dimensional vector on the lens plane and  $\rho$  is the three-dimensional density.

As long as the thin screen approximation holds, the total deflection angle is obtained by summing the contribution of all the mass elements  $\Sigma(\vec{\xi})d^2\xi$ :

$$\hat{\alpha}(\vec{\xi}) = \frac{4G}{c^2} \int \frac{(\vec{\xi} - \vec{\xi}')\Sigma(\vec{\xi}')}{|\vec{\xi} - \vec{\xi}'|^2} d^2\xi'. \quad (1.48)$$

This equation shows that the calculation of the deflection angle is formally a convolution of the surface density  $\Sigma(\vec{\xi})$  with the kernel function

$$\vec{K}(\vec{\xi}) \propto \frac{\vec{\xi}}{|\vec{\xi}|^2}. \quad (1.49)$$

This enables the calculation of the deflection angle field in the Fourier space as the product of the Fourier transforms of  $\Sigma$  and  $K$ :

$$\tilde{\alpha}_i(\vec{k}) \propto \tilde{\Sigma}(\vec{k})\tilde{K}_i(\vec{k}), \quad (1.50)$$

where  $\vec{k}$  is the conjugate variable to  $\vec{\xi}$  and the tilde denotes the Fourier Transforms. The subscript  $i \in [1, 2]$  indicates the two components along the two axes on the lens plane (remember that  $\hat{\alpha}$  is a vector!). This calculation can be implemented efficiently using the *Fast-Fourier-Transform (FFT)* algorithm (Cooley and Tukey, 1965). Note that this assumes that the integration extends to an infinite domain, while gravitational lenses have finite mass distributions. FFT algorithms implement this feature assuming periodic conditions on the boundaries of the integration domain.

## 1.5 Python applications

### 1.5.1 Deflection by a black-hole

In our first python application, we write a script to produce Fig. 1.2.2. A brief python tutorial can be found in Appendix A.

We want to implement the formula in Eq. 1.42. We also need to remind that

$$u^2 = \frac{C(R_m)}{A(R_m)}$$

We will compare the resulting deflection angle to

$$\hat{\alpha} = \frac{4GM}{c^2 u} \quad (1.51)$$

which is the result we obtained in the weak-field limit.

We start by importing some useful packages:

```
from scipy import special as sy # need special functions for incomplete \\ 
# elliptic integrals of the first kind
import numpy as np # efficient vector and matrix operations
import matplotlib.pyplot as plt # a MATLAB-like plotting framework
%matplotlib inline # only needed in jupyter notebooks
```

Note that we import the module `special` from `scipy` in order to compute the elliptic integral of the first kind appearing in Eq. 1.42. See <https://docs.scipy.org/doc/scipy/reference/special.html>.

Our goal is to produce a graph. Let's setup the fonts and the character size

```

font = {'family' : 'normal',
        'weight' : 'normal',
        'size'   : 20}

import matplotlib
matplotlib.rcParams['font', **font]

```

The task can be completed in several ways. Here we chose to build a class for point black-holes:

```

class point_bh:

    def __init__(self,M):
        self.M=M

        # functions which define the metric.
    def A(self,r):
        return(1.0-2.0*self.M/r)

    def B(self,r):
        return (self.A(r)**(-1))

    def C(self,r):
        return(r**2)

        # compute u from rm
    def u(self,r):
        u=np.sqrt(self.C(r)/self.A(r))
        return(u)

        # functions concurring to the deflection angle calculation
    def ss(self,r):
        return(np.sqrt((r-2.0*self.M)*(r+6.0*self.M)))

    def mm(self,r,s):
        return((s-r+6.0*self.M)/2/s)

    def phif(self,r,s):
        return(np.arcsin(np.sqrt(2.0*s/(3.0*r-6.0*self.M+s)))))

        # the deflection angle
    def defAngle(self,r):
        s=self.ss(r)
        m=self.mm(r,s)
        phi=self.phif(r,s)
        F=sy.ellipkinc(phi, m) # using the ellipkinc function
                               # from scipy.special
        return(-np.pi+4.0*np.sqrt(r/s)*F)

```

The class contains several methods which will be used to compute the deflection angle. For example, we implement the functions  $A(R)$ ,  $B(R)$ , and  $C(R)$ . These will be used to convert the minimal distance  $R_m$  to  $u$ . We also implement the functions  $s, m, \varphi$ , which depend on the mass of the black-hole and on the minimal distance  $R_m$ . Finally, we implement the function `defAngle`, which

enables to compute the deflection angle using Eq. 1.42. This function uses the method `elipkinc` from `scipy.special` to compute the incomplete elliptic integral of the first kind,  $F(\varphi, m)$ . Note that  $\varphi$  and  $m$  can be passed as numpy arrays, i.e. `elipkinc` can return values for a number of couples  $(\varphi, m)$ .

Following the same approach, we build another class which deals with point lenses in the weak field limit, i.e. it implements Eq. 1.51:

```
class point_mass:

    def __init__(self,M):
        self.M=M

        # the classical formula
    def defAngle(self,u):
        return(4.0*self.M/u)
```

We can now use the two classes above to build two objects, namely a black-hole lens (employing the exact solution for the deflection angle) and a point mass lens, for which we will adopt the weak-field limit. In both cases, the mass of the lens is fixed to  $3M_\odot$ . For a mass of this size, the Schwarzschild radius is  $R_s \sim 9\text{km}$ :

```
bh=point_bh(3.0)
pm=point_mass(3.0)
```

We now use the `linspace` method from `numpy` to initialize a vector of minimal distances  $R_m$ , which we will use to compute  $\hat{\alpha}$ . We use the method `u(r)` of `point_bh` to convert  $R_m$  into an array of impact parameters  $u$ :

```
r=np.linspace(3.0/2.0,10,1000)*2.0*bh.M
u=bh.u(r)/2.0/bh.M
```

The deflection angle as a function of  $u$  or  $R_m$  can be computed in the cases of the exact solution and in the weak field limit using the method `defAngle` applied to `bh` and `pm`:

```
a=bh.defAngle(r)
b=pm.defAngle(u*2.0*bh.M)
```

Note that  $u$  is in units of the Schwarzschild radius and that we have set  $G/c^2 = 1$ .

Finally, we can produce a nice figure displaying the results of the calculation. We use `matplotlib.pyplot` to do this:

```
# initialize figure and axes
# (single plot, 15" by 8" in size)
fig,ax=plt.subplots(1,1,figsize=(15,8))
# plot the exact solution in ax
ax.plot(u,a,'-',label='exact solution')
# plot the solution in the weak field limit
ax.plot(u,b,'--',label='weak field limit',color='red')
# set the labels for the x and the y axes
ax.set_xlabel(r'$u$ $[2GM/c^2]$')
ax.set_ylabel(r'$\hat{\alpha}(u)$ [radians]')
# add the legend
ax.legend()
```

We also want to show the vertical asymptote at  $u_{lim} = 3\sqrt{3}/2$ :

```
# plot a vertical dotted line at u=3\sqrt(3)/2
x=[np.min(u),np.min(u)]
y=[0,10]
ax.plot(x,y,':')
```

To conclude, we save the figure in a .png file:

```
# save figure in png format
fig.savefig('bhalpha.png')
```

### 1.5.2 Deflection by an extended mass distribution

In this application, we implement the calculation of the deflection angle field by an extended lens. A two-dimensional map of the lens surface-density is provided by the fits file `kappa_g1.fits` (see the data folder in the github repository). The map was obtained by projecting the mass distribution of a dark matter halo obtained from N-body simulations on a lens plane. To be precise, this is the surface density divided by a constant which depends on the lens and source redshifts (we will talk about this constant in the next lectures). Let's denote this quantity as  $\kappa$ . Accounting for this normalization, the calculation we want to implement is

$$\vec{\alpha}(\vec{x}) = \frac{1}{\pi} \int \kappa(\vec{x}') \frac{\vec{x} - \vec{x}'}{|\vec{x} - \vec{x}'|^2} d^2x'.$$

This is a convolution, which can be written in the Fourier Space as

$$\vec{\alpha}(\vec{k}) = 2\pi \tilde{\kappa}(\vec{k}) \vec{K}(\vec{k})$$

where  $\vec{K}(\vec{k})$  is the Fourier Transform of

$$\vec{K}(\vec{x}) = \frac{1}{\pi} \frac{\vec{x}}{|\vec{x}|^2}$$

We use the `numpy.fft` module:

```
import numpy as np
import numpy.fft as fftengine
```

We define a class called `deflector`, where the `deflector` object is initialized by reading the fits file containing the surface density map of the lens. To deal with the fits files, we need to use the `astropy.io.fits` module.

The class contains some methods to

- build the kernel  $K(\vec{x})$ ;
- compute the deflection angle map by convolving the convergence with the kernel;
- perform the so-called "zero-padding";
- crop the zero-padded maps.

```

import astropy.io.fits as pyfits

class deflector(object):

    # initialize the deflector using a surface density (convergence) map
    # the boolean variable pad indicates whether zero-padding is used
    # or not
    def __init__(self,filekappa,pad=False):
        kappa,header=pyfits.getdata(filekappa,header=True)
        self.kappa=kappa
        self.nx=kappa.shape[0]
        self.ny=kappa.shape[1]
        self.pad=pad
        if (pad):
            self.kpad()
        self.kx,self.ky=self.kernel()

    # implement the kernel function K
    def kernel(self):
        x=np.linspace(-0.5,0.5,self.kappa.shape[0])
        y=np.linspace(-0.5,0.5,self.kappa.shape[1])
        kx,ky=np.meshgrid(x,y)
        norm=(kx**2+ky**2+1e-12)
        kx=kx/norm/np.pi
        ky=ky/norm/np.pi
        return(kx,ky)

    # compute the deflection angle maps by convolving
    # the surface density with the kernel function
    def angles(self):
        # FFT of the surface density and of the two components of the kernel
        density_ft = fftengine.fftn(self.kappa,axes=(0,1))
        kernelx_ft = fftengine.fftn(self.kx,axes=(0,1),
                                    s=self.kappa.shape)
        kernely_ft = fftengine.fftn(self.ky,axes=(0,1),
                                    s=self.kappa.shape)
        # perform the convolution in Fourier space and transform the result
        # back in real space. Note that a shift needs to be applied using
        # fftshift
        alphax = 2.0/(self.kappa.shape[0])/(np.pi)**2*\n            fftengine.fftshift(fftengine.ifftn(2.0*\n                np.pi*density_ft*kernelx_ft))
        alphay = 2.0/(self.kappa.shape[0])/(np.pi)**2*\n            fftengine.fftshift(fftengine.ifftn(2.0*\n                np.pi*density_ft*kernely_ft))
        return(alphax.real,alphay.real)

    # returns the surface-density (convergence) of the deflector
    def kmap(self):
        return(self.kappa)

```

```

# performs zero-padding
def kpad(self):
    # add zeros around the original array
    def padwithzeros(vector, pad_width, iaxis, kwargs):
        vector[:pad_width[0]] = 0
        vector[-pad_width[1]:] = 0
        return vector
    # use the pad method from numpy.lib to add zeros (padwithzeros)
    # in a frame with thickness self.kappa.shape[0]
    self.kappa=np.lib.pad(self.kappa, self.kappa.shape[0],
                          padwithzeros)

    # crop the maps to remove zero-padded areas and get back to the
    # original region.
def mapCrop(self,mappa):
    xmin=0.5*(self.kappa.shape[0]-self.nx)
    ymin=0.5*(self.kappa.shape[1]-self.ny)
    xmax=xmin+self.nx
    ymax=ymin+self.ny
    mappa=mappa[xmin:xmax,ymin:ymax]
    return(mappa)

```

We can now build a deflector and use it to compute the deflection angles employing the method `angles`:

```

df=deflector('data/kappa_gl.fits')
angx_nopad,angy_nopad=df.angles()
kappa=df.kmap()

import matplotlib.pyplot as plt
from matplotlib.colors import LogNorm, PowerNorm, SymLogNorm
%matplotlib inline

fig,ax = plt.subplots(1,3,figsize=(16,8))
ax[0].imshow(kappa,origin="lower")
ax[0].set_title('convergence')
ax[1].imshow(angx_nopad,origin="lower")
ax[1].set_title('angle 1')
ax[2].imshow(angy_nopad,origin="lower")
ax[2].set_title('angle 2')

```

Note that at this point we have not yet used the zero-padding trick. FFT assumes periodic boundary conditions, meaning that the lens mass distribution is replicated outside the boundaries. Given that the region around the lens considered in this example is relatively small, we expect that the deflection angles will be biased near the borders. The three panels in Fig. 1.5.1 show the maps of the convergence and of the two components of the deflection angles obtained with this setting.

Zero-padding consists of placing zeros all around the convergence map. By doing so, we double the size of the original map, but we expect to increase the accuracy of the calculations near the borders, because the periodic conditions are better reproduced in this setting. We activate zero-padding by just setting the variable `pad=True` when initializing the deflector. Fig. 1.5.2 shows the zero-padded convergence map and the two new maps of the deflection angle components.

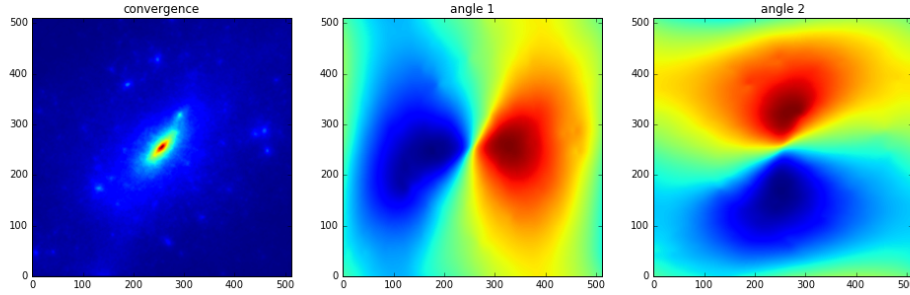


**Figure 1.5.1:** Left panel: the surface density (convergence) map of the lens. Middle and right panels: maps of the two components of the deflection angles.

```
df=deflector('data/kappa_gl.fits',True)
angx,angy=df.angles()
kappa=df.kmap()

fig,ax = plt.subplots(1,3,figsize=(16,8))
angx,angy=df.angles()
ax[0].imshow(kappa,origin="lower")
ax[0].set_title('convergence')
ax[1].imshow(angx,origin="lower")
ax[1].set_title('angle 1')
ax[2].imshow(angy,origin="lower")
ax[2].set_title('angle 2')
```

We are not interested in this large area, thus we can get rid of the values outside the lens convergence map by cropping the deflection angle maps. The results are shown in Fig. 1.5.3 and compared to the previous ones. In fact, significant differences are visible along the borders.

```
angx=df.mapCrop(angx)
angy=df.mapCrop(angy)

fig,ax = plt.subplots(2,2,figsize=(16,16))
ax[0,0].imshow(angx,origin="lower")
ax[0,0].set_title('angle 1')
ax[0,1].imshow(angy,origin="lower")
ax[0,1].set_title('angle 2')
ax[1,0].imshow(angx_nopad,origin="lower")
ax[1,0].set_title('angle 1 - no zero pad')
ax[1,1].imshow(angy_nopad,origin="lower")
ax[1,1].set_title('angle 2 - no zero pad')
```

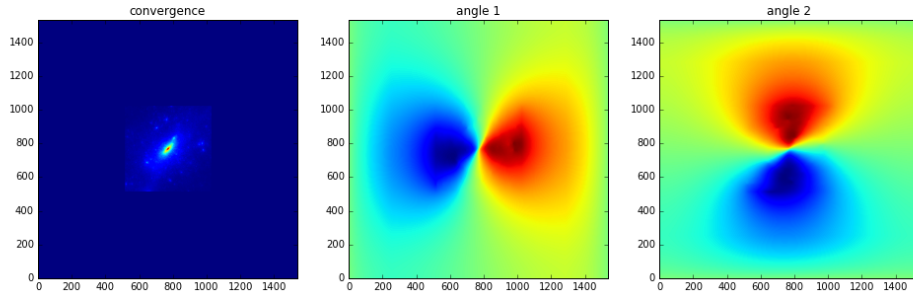


**Figure 1.5.2:** The figure shows the same maps as in Fig. 1.5.1, but with zero-padding. Indeed, as shown in the left panel, the lens is surrounded by a frame of zeros, and the deflection angle maps are computed on an area which has double the size of the maps in Fig. 1.5.1.

## 1.6 Problems

**Problem 1.1** — Write a python script to produce a figure displaying  $\hat{\alpha}(R_m)$  with  $R_m$  in the range 9-1000 km for two lenses with mass  $M = 3M_\odot$  and  $M = 10M_\odot$ .

**Problem 1.2** — Define a class for an ensemble of point masses. The class should be initialized with two numpy arrays containing the masses and the positions of the lenses. Use the thin screen approximation and write the method to compute the deflection angle at a certain location on the lens plane..

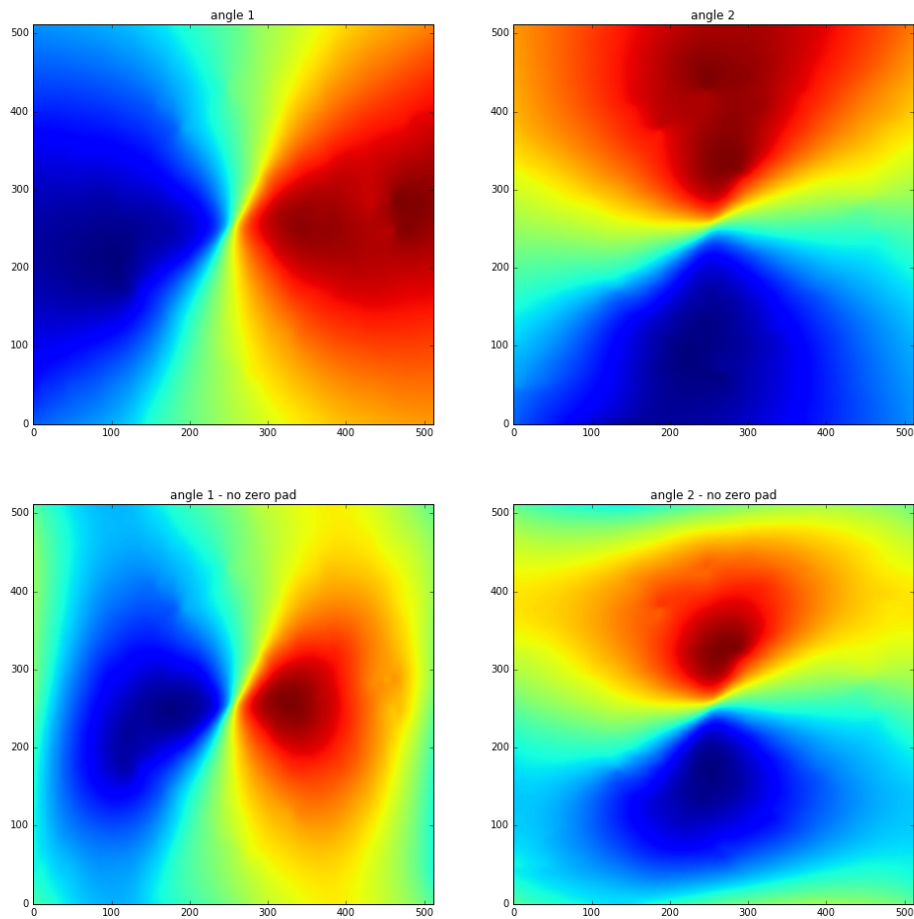


**Figure 1.5.3:** The upper panels show the same two maps displayed in the middle and right panels of Fig. 1.5.2, which have been cropped to match the original size of the input convergence map. The bottom panels show the maps obtained without padding, for comparison.





## 2. The general lens

### 2.1 Lens equation

Gravitational lensing is sensitive to the geometry of the universe. In particular, as in refractive phenomena, the amplitude of the lensing effects is heavily dependent on the distances between the observer, the lenses, and the sources. These are in turn related to the curvature and expansion rate of the universe, which suggests that gravitational lensing is indeed a powerful tool for cosmology.

#### Intrinsic and apparent source position

In this section, we seek a relationship between observed and intrinsic positions of a source in a gravitational lensing event. In absence of the lens, the light emitted by a distant source reaches an observer, who sees the source at a certain position on the sky,  $\vec{\beta}$  (in angular units). This is the *intrinsic* position of the source. Instead, when photons are deflected by the gravitational lens, the observer collects them from a different direction,  $\vec{\theta}$ , which corresponds to the *apparent* (or *observed*) position of the source. We refer to the apparent position of the source as to the *image* position.

In Fig. (2.1.1), we sketch a typical gravitational lens system. A mass is placed at redshift  $z_L$ , corresponding to an angular diameter distance  $D_L$ . This lens deflects the light rays coming from a source at redshift  $z_S$  (or angular distance  $D_S$ ). At the bottom of the diagram, an observer collects the photons from the distant source. The angular diameter distance between the lens and the source is  $D_{LS}$ .

**R** The angular diameter distance  $D_A$  is defined as the ratio of an object's physical transverse size to its angular size (in radians). Therefore, it is used to convert angular separations in the sky to physical separations on the plane of the sources.

This distance does not increase indefinitely with redshift, but it peaks at  $z \sim 1$  and then it turns over. Due to the expansion of the universe the angular diameter distance between  $z_1$  and  $z_2$  (with  $z_2 > z_1$ ) is not found by subtracting the two individual angular diameter distances:

$$D_A(z_1, z_2) \neq D_A(z_2) - D_A(z_1) \quad (2.1)$$

except for those situations where the expansion of the universe can be neglected (i.e. for lenses and sources in our own galaxy). Hogg (1999) presents a concise summary of cosmological

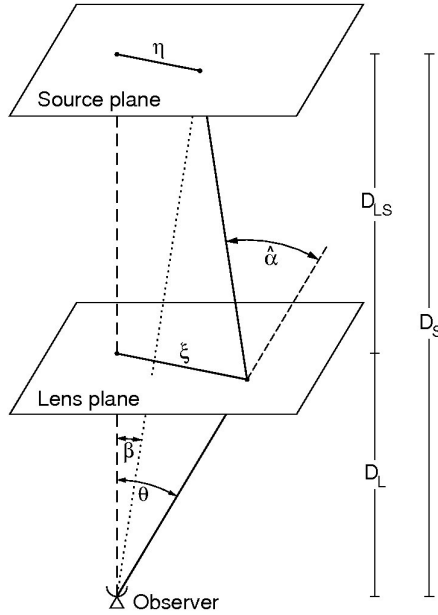


**Figure 2.1.1:** Sketch of a typical gravitational lensing system. Figure from Bartelmann and Schneider (2001).

distances. More in-depth discussions can be found in several cosmology books (see e.g. Weinberg, 1972).

### Thin screen approximation

If the physical size of the lens is small compared to the distances  $D_L$ ,  $D_{LS}$ , and  $D_S$ , the extension of the lens along the line-of-sight can be neglected in the calculation of the light deflection. We can assume that this occurs on a plane, called the *lens plane*.

**R** Given that the apparent position of the source, or image position, originates on this plane, the lens plane is often referred as the *image plane*.

Similarly, we can assume that all photons emitted by the source originate from the same distance  $D_S$ , meaning that the source lies on a *source plane*. The approximation of the lens and of the source to planar distributions of mass and light, is called *thin screen approximation*.

### Relating the intrinsic and apparent positions of the source

We first define an optical axis, indicated in Fig. (2.1.1) by the dashed line, perpendicular to the lens and source planes and passing through the observer. Then we measure the angular positions on the lens and on the source planes with respect to this reference direction.

Consider a source at the intrinsic angular position  $\vec{\beta}$ , which lies on the source plane at a distance  $\vec{\eta} = \vec{\beta}D_S$  from the optical axis. The source emits photons (we may now use the term “light rays”) that impact the lens plane at  $\vec{\xi} = \vec{\theta}D_L$ , are deflected by the angle  $\hat{\alpha}$ , and finally reach the observer. The amplitude of the deflection is given by Eq. (1.32).

Due to the deflection, the observer receives the light coming from the source as if it was emitted at the apparent angular position  $\vec{\theta}$ . Note that we have used vectors to identify the source and image positions on the corresponding planes, either in the case of angular and physical positions.

If  $\vec{\theta}$ ,  $\vec{\beta}$ , and  $\hat{\alpha}$  are small, the true position of the source and its observed position on the sky are related by a very simple relation, which can be readily obtained from the diagram in Fig. 2.1.1.

This relation is called the *lens equation* and is written as

$$\vec{\theta} D_S = \vec{\beta} D_S + \hat{\alpha} D_{LS}, \quad (2.2)$$

where  $D_{LS}$  is the angular diameter distance between lens and source.

Defining the reduced deflection angle

$$\vec{\alpha}(\vec{\theta}) \equiv \frac{D_{LS}}{D_S} \hat{\alpha}(\vec{\theta}), \quad (2.3)$$

from Eq. (2.2), we obtain

$$\vec{\beta} = \vec{\theta} - \vec{\alpha}(\vec{\theta}). \quad (2.4)$$

This equation, called *lens equation*, is apparently very simple. However,  $\vec{\alpha}(\vec{\theta})$  can be a complicated function of  $\vec{\theta}$ , which implies that the equation can only be solved numerically in many cases.

It is very common and useful to write Eq. (2.2) in dimensionless form. This can be done by defining a length scale  $\xi_0$  on the lens plane and a corresponding length scale  $\eta_0 = \xi_0 D_S / D_L$  on the source plane. Then, we define the dimensionless vectors

$$\vec{x} \equiv \frac{\vec{\xi}}{\xi_0} \quad ; \quad \vec{y} \equiv \frac{\vec{\eta}}{\eta_0}, \quad (2.5)$$

as well as the scaled deflection angle

$$\vec{\alpha}(\vec{x}) = \frac{D_L D_{LS}}{\xi_0 D_S} \hat{\alpha}(\xi_0 \vec{x}). \quad (2.6)$$

Carrying out some substitutions, Eq. (2.2) can finally be written as

$$\vec{y} = \vec{x} - \vec{\alpha}(\vec{x}). \quad (2.7)$$

### Solving the lens equation

From Eqs. 2.4 and 2.7, it is obvious that knowing the intrinsic position of the source and the deflection angle field  $\vec{\alpha}(\vec{\theta})$  of the lens, the positions of the image(s) can be found by solving the lens equation for  $\vec{\theta}$ . As it will be discussed later on, this can be achieved analytically only for very simple lens mass distributions. Indeed, the equation is typically highly non-linear. When multiple solutions exist, the source is lensed into *multiple images*.

When observing a lens system, the intrinsic position of the source is unknown, while the position of its images can be measured. Then the source intrinsic position can be recovered by assuming a model for the mass distribution of the lens, i.e. by solving the lens equation for  $\vec{\beta}$ . This is a much easier task, because the lens equation is linear in  $\vec{\beta}$ : for each image there is a unique solution. Thus, if multiple images of the same source are identified, and the lens mass model is correct, the same solution of the lens equation should be found for all images.

## 2.2 Lensing potential

An extended distribution of matter is characterized by its *effective lensing potential*, obtained by projecting the three-dimensional Newtonian potential on the lens plane and by properly rescaling it:

$$\hat{\Psi}(\vec{\theta}) = \frac{D_{LS}}{D_L D_S} \frac{2}{c^2} \int \Phi(D_L \vec{\theta}, z) dz. \quad (2.8)$$

The lensing potential satisfies two important properties:

**1. the gradient of  $\hat{\Psi}$  is the reduced deflection angle:**

$$\vec{\nabla}_\theta \hat{\Psi}(\vec{\theta}) = \vec{\alpha}(\vec{\theta}) . \quad (2.9)$$

Indeed, by taking the gradient of the lensing potential we obtain:

$$\begin{aligned} \vec{\nabla}_\theta \hat{\Psi}(\vec{\theta}) &= D_L \vec{\nabla}_\perp \hat{\Psi} = \vec{\nabla}_\perp \left( \frac{D_{LS}}{D_S} \frac{2}{c^2} \int \hat{\Phi}(\vec{\theta}, z) dz \right) \\ &= \frac{D_{LS}}{D_S} \frac{2}{c^2} \int \vec{\nabla}_\perp \Phi(\vec{\theta}, z) dz \\ &= \vec{\alpha}(\vec{\theta}) \end{aligned} \quad (2.10)$$

Note that, using the dimensionless notation,

$$\vec{\nabla}_x = \frac{\xi_0}{D_L} \vec{\nabla}_\theta . \quad (2.11)$$

We can see that

$$\vec{\nabla}_x \hat{\Psi}(\vec{\theta}) = \frac{\xi_0}{D_L} \vec{\nabla}_\theta \hat{\Psi}(\vec{\theta}) = \frac{\xi_0}{D_L} \vec{\alpha}(\vec{\theta}) . \quad (2.12)$$

By multiplying both sides of this equation by  $D_L^2/\xi_0^2$ , we obtain

$$\frac{D_L^2}{\xi_0^2} \vec{\nabla}_x \hat{\Psi} = \frac{D_L}{\xi_0} \vec{\alpha} . \quad (2.13)$$

This allows us to introduce the dimensionless counterpart of  $\hat{\Psi}$ :

$$\Psi = \frac{D_L^2}{\xi_0^2} \hat{\Psi} . \quad (2.14)$$

Substituting Eq. 2.14 into Eq 2.13, we see that

$$\vec{\nabla}_x \Psi(\vec{x}) = \vec{\alpha}(\vec{x}) . \quad (2.15)$$

**2. the Laplacian of  $\hat{\Psi}$  is twice the *convergence*  $\kappa$ :**

$$\Delta_\theta \Psi(\vec{\theta}) = 2\kappa(\vec{\theta}) . \quad (2.16)$$

The *convergence* is defined as a dimensionless surface density

$$\kappa(\vec{\theta}) \equiv \frac{\Sigma(\vec{\theta})}{\Sigma_{cr}} \quad \text{with} \quad \Sigma_{cr} = \frac{c^2}{4\pi G} \frac{D_S}{D_L D_{LS}} , \quad (2.17)$$

where  $\Sigma_{cr}$  is called the *critical surface density*, a quantity which characterizes the lens system and which is a function of the angular diameter distances of lens and source.

Eq. 2.16 is derived from the Poisson equation,

$$\Delta \Phi = 4\pi G \rho . \quad (2.18)$$

The surface mass density is

$$\Sigma(\vec{\theta}) = \frac{1}{4\pi G} \int_{-\infty}^{+\infty} \Delta \Phi dz \quad (2.19)$$

and

$$\kappa(\vec{\theta}) = \frac{1}{c^2} \frac{D_L D_{LS}}{D_S} \int_{-\infty}^{+\infty} \Delta \Phi dz . \quad (2.20)$$

Let us now introduce a two-dimensional Laplacian

$$\triangle_\theta = \frac{\partial^2}{\partial \theta_1^2} + \frac{\partial^2}{\partial \theta_2^2} = D_L^2 \left( \frac{\partial^2}{\partial \xi_1^2} + \frac{\partial^2}{\partial \xi_2^2} \right) = D_L^2 \left( \Delta - \frac{\partial^2}{\partial z^2} \right), \quad (2.21)$$

which gives

$$\Delta \Phi = \frac{1}{D_L^2} \triangle_\theta \Phi + \frac{\partial^2 \Phi}{\partial z^2}. \quad (2.22)$$

Inserting Eq. 2.22 into Eq. 2.20, we obtain

$$\kappa(\vec{\theta}) = \frac{1}{c^2} \frac{D_{LS}}{D_S D_L} \left[ \triangle_\theta \int_{-\infty}^{+\infty} \Phi dz + D_L^2 \int_{-\infty}^{+\infty} \frac{\partial^2 \Phi}{\partial z^2} dz \right]. \quad (2.23)$$

If the lens is gravitationally bound,  $\partial \Phi / \partial z = 0$  at its boundaries and the second term on the right hand side vanishes. From Eqs. 2.8 and 2.14, we find

$$\kappa(\theta) = \frac{1}{2} \triangle_\theta \hat{\Psi} = \frac{1}{2} \frac{\xi_0^2}{D_L^2} \triangle_\theta \Psi. \quad (2.24)$$

Since

$$\triangle_\theta = D_L^2 \triangle_\xi = \frac{D_L^2}{\xi_0^2} \triangle_x, \quad (2.25)$$

using dimensionless quantities, Eq. 2.24 reads

$$\kappa(\vec{x}) = \frac{1}{2} \triangle_x \Psi(\vec{x}) \quad (2.26)$$

Integrating Eq. (2.16), the effective lensing potential can be written in terms of the convergence as

$$\Psi(\vec{x}) = \frac{1}{\pi} \int_{\mathbf{R}^2} \kappa(\vec{x}') \ln |\vec{x} - \vec{x}'| d^2 x', \quad (2.27)$$

from which we obtain that the scaled deflection angle is

$$\vec{\alpha}(\vec{x}) = \frac{1}{\pi} \int_{\mathbf{R}^2} d^2 x' \kappa(\vec{x}') \frac{\vec{x} - \vec{x}'}{|\vec{x} - \vec{x}'|}. \quad (2.28)$$

### 2.3 First order lens mapping

One of the main consequences of gravitational lensing is image distortion. This is particularly evident when the source has an extended size. For example, background galaxies can appear as very long arcs when lensed by galaxy clusters or other galaxies.

The distortion arises because light bundles are deflected differentially. Ideally, the shape of the images can be determined by solving the lens equation for all the points within the extended source. In particular, if the source is much smaller than the angular scale on which the lens deflection angle field changes, the relation between source and image positions can locally be linearized.

This situation is sketched in Fig. 2.3.1. Let us consider a point on the lens (or image) plane at position  $\vec{\theta}$ , where the deflection angle is  $\vec{\alpha}$ . If the deflection angle satisfies the above conditions, at the nearby location  $\vec{\theta}' = \vec{\theta} + d\vec{\theta}$ , the deflection will be

$$\vec{\alpha}' \simeq \vec{\alpha} + \frac{d\vec{\alpha}}{d\vec{\theta}} d\vec{\theta}. \quad (2.29)$$

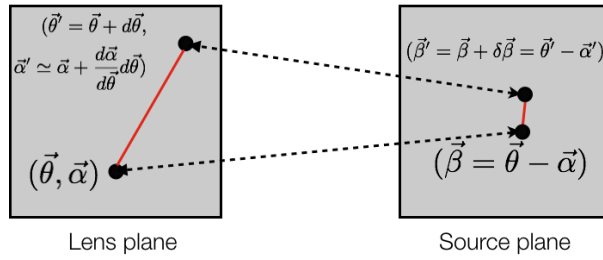


**Figure 2.3.1:** Linear mapping between the lens and the source plane, assuming a slowly varying deflection angle.

Using the lens equation, the points  $\vec{\theta}$  and  $\vec{\theta}'$  can be mapped on the points  $\vec{\beta}$  and  $\vec{\beta}' = \vec{\beta} + d\vec{\beta}$  onto the source plane. Through this mapping, the vector  $(\vec{\beta}' - \vec{\beta})$  is given by

$$(\vec{\beta}' - \vec{\beta}) = \left( I - \frac{d\vec{\alpha}}{d\vec{\theta}} \right) (\vec{\theta}' - \vec{\theta}). \quad (2.30)$$

In other words, the distortion of images can be described by the Jacobian matrix

$$A \equiv \frac{\partial \vec{\beta}}{\partial \vec{\theta}} = \left( \delta_{ij} - \frac{\partial \alpha_i(\vec{\theta})}{\partial \theta_j} \right) = \left( \delta_{ij} - \frac{\partial^2 \hat{\Psi}(\vec{\theta})}{\partial \theta_i \partial \theta_j} \right), \quad (2.31)$$

where  $\theta_i$  indicates the  $i$ -component of  $\vec{\theta}$  on the lens plane.

Eq. (2.31) shows that the elements of the Jacobian matrix can be written as combinations of the second derivatives of the lensing potential. For brevity, we will use the shorthand notation

$$\frac{\partial^2 \hat{\Psi}(\vec{\theta})}{\partial \theta_i \partial \theta_j} \equiv \hat{\Psi}_{ij}. \quad (2.32)$$

We can now split off the isotropic part from the Jacobian, to obtain its traceless part:

$$\left( A - \frac{1}{2} \text{tr} A \cdot I \right)_{ij} = \delta_{ij} - \hat{\Psi}_{ij} - \frac{1}{2}(1 - \hat{\Psi}_{11} + 1 - \hat{\Psi}_{22})\delta_{ij} \quad (2.33)$$

$$= -\hat{\Psi}_{ij} + \frac{1}{2}(\hat{\Psi}_{11} + \hat{\Psi}_{22})\delta_{ij} \quad (2.34)$$

$$= \begin{pmatrix} -\frac{1}{2}(\hat{\Psi}_{11} - \hat{\Psi}_{22}) & -\hat{\Psi}_{12} \\ -\hat{\Psi}_{12} & \frac{1}{2}(\hat{\Psi}_{11} - \hat{\Psi}_{22}) \end{pmatrix}. \quad (2.35)$$

This allows us to define the *shear* tensor

$$\Gamma = \begin{pmatrix} \gamma_1 & \gamma_2 \\ \gamma_2 & -\gamma_1 \end{pmatrix}, \quad (2.36)$$

often written in the form of a pseudo-vector  $\vec{\gamma} = (\gamma_1, \gamma_2)$ , whose components are

$$\gamma_1 = \frac{1}{2}(\hat{\Psi}_{11} - \hat{\Psi}_{22}) \quad (2.37)$$

$$\gamma_2 = \hat{\Psi}_{12} = \hat{\Psi}_{21}. \quad (2.38)$$

The shear is manifestly an symmetric, traceless tensor. It quantifies the projection of the gravitational tidal field (the gradient of the gravitational force), which describes distortions of background sources.

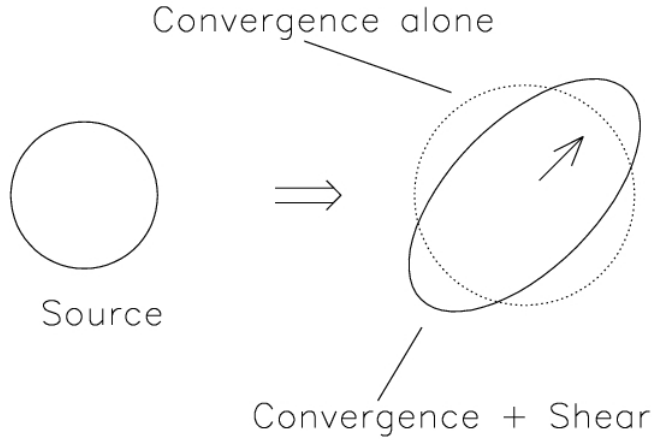


**Figure 2.3.2:** Distortion effects due to convergence and shear on a circular source (Figure from Narayan & Bartelmann, 1995).

The eigenvalues of the shear tensor are

$$\pm \sqrt{\gamma_1^2 + \gamma_2^2} = \pm \gamma. \quad (2.39)$$

Thus, there exist a rotation  $R(\phi)$  such that the Jacobian can be written in a diagonal form. Generally, the Jacobian transforms as

$$A \rightarrow A' = R(\phi)^T A R(\phi) \quad (2.40)$$

where  $T$  indicates the transposed matrix. This shows that the shear components transform under rotations as

$$\begin{aligned} \gamma_1 &\rightarrow \gamma'_1 = \gamma_1 \cos(2\phi) + \gamma_2 \sin(2\phi) \\ \gamma_2 &\rightarrow \gamma'_2 = -\gamma_1 \sin(2\phi) + \gamma_2 \cos(2\phi), \end{aligned} \quad (2.41)$$

unlike a vector. Since the shear components are invariant under rotations of  $\phi = \pi$  rather than  $\phi = 2\pi$ , they form a spin-2 tensor.

We can write the shear tensor as

$$\begin{pmatrix} \gamma_1 & \gamma_2 \\ \gamma_2 & -\gamma_1 \end{pmatrix} = \gamma \begin{pmatrix} \cos 2\phi & \sin 2\phi \\ \sin 2\phi & -\cos 2\phi \end{pmatrix}, \quad (2.42)$$

where we have introduced the angle  $\phi$ , which identifies the direction of the eigenvector of the shear tensor corresponding to the eigenvalue  $+\gamma$ .



Note the factor 2 on the angle  $\phi$ , which reminds that the shear component are elements of a  $2 \times 2$  tensor and not a vector.

The remainder of the Jacobian is

$$\frac{1}{2} \text{tr}A \cdot I = \left[ 1 - \frac{1}{2}(\hat{\Psi}_{11} + \hat{\Psi}_{22}) \right] \delta_{ij} \quad (2.43)$$

$$= \left( 1 - \frac{1}{2} \Delta \hat{\Psi} \right) \delta_{ij} = (1 - \kappa) \delta_{ij}. \quad (2.44)$$

Thus, the Jacobian matrix becomes

$$\begin{aligned} A &= \begin{pmatrix} 1 - \kappa - \gamma_1 & -\gamma_2 \\ -\gamma_2 & 1 - \kappa + \gamma_1 \end{pmatrix} \\ &= (1 - \kappa) \begin{pmatrix} 1 & 0 \\ 0 & 1 \end{pmatrix} - \gamma \begin{pmatrix} \cos 2\phi & \sin 2\phi \\ \sin 2\phi & -\cos 2\phi \end{pmatrix}. \end{aligned} \quad (2.45)$$

The last equation explains the meaning of both convergence and shear. The convergence determines an isotropic transformation, i.e. the images are only rescaled by a constant factor in all directions. On the other hand, the shear stretches the intrinsic shape of the source along privileged directions.

The eigenvalues of the Jacobian matrix are

$$\lambda_t = 1 - \kappa - \gamma \quad (2.46)$$

$$\lambda_r = 1 - \kappa + \gamma. \quad (2.47)$$

Let consider the reference frame where the Jacobian is diagonal. Then,

$$A = \begin{pmatrix} 1 - \kappa - \gamma & 0 \\ 0 & 1 - \kappa + \gamma \end{pmatrix}. \quad (2.48)$$

Consider a circular source, whose isophotes have equation  $\beta_1^2 + \beta_2^2 = r^2$ . The lens equation implies that the points on the source plane satisfying this equation are mapped onto the points  $(\theta_1, \theta_2)$ , such that

$$\begin{pmatrix} \beta_1 \\ \beta_2 \end{pmatrix} = \begin{pmatrix} 1 - \kappa - \gamma & 0 \\ 0 & 1 - \kappa + \gamma \end{pmatrix} \begin{pmatrix} \theta_1 \\ \theta_2 \end{pmatrix}. \quad (2.49)$$

Thus

$$\beta_1 = (1 - \kappa - \gamma)\theta_1 \quad (2.50)$$

$$\beta_2 = (1 - \kappa + \gamma)\theta_2. \quad (2.51)$$

Summing in quadrature, we obtain

$$r^2 = \beta_1^2 + \beta_2^2 = (1 - \kappa - \gamma)^2 \theta_1^2 + (1 - \kappa + \gamma)^2 \theta_2^2, \quad (2.52)$$

which is the equation of an ellipse on the lens plane. Thus, a circular source, which is small enough compared to the typical length-scale over which the lens deflection field varies, like is mapped onto an ellipse when  $\kappa$  and  $\gamma$  are both non-zero, as shown in Fig. (2.3.2).

The semi-major and -minor axes of the ellipse are

$$a = \frac{r}{1 - \kappa - \gamma}, \quad b = \frac{r}{1 - \kappa + \gamma}. \quad (2.53)$$

Obviously, the ellipse reduces to a circle if  $\gamma = 0$ .

## 2.4 Magnification

An important consequence of the lensing distortion is the magnification. Through the lens equation, the solid angle element  $\delta\beta^2$  (or equivalently the surface element  $\delta\eta^2$  or  $\delta y^2$ ) is mapped onto the solid angle  $\delta\theta^2$  (or on the surface element  $\delta\xi^2$  or  $\delta x^2$ ). Because of the Liouville theorem, in absence of emission and absorbtion of photons, the source surface brightness is conserved despite light deflection. Thus, the change of the solid angle under which the source is observed implies that the flux received is magnified (or demagnified).

Given Eq. (2.31), the *magnification* is given by the inverse of the determinant of the Jacobian matrix. For this reason, the matrix  $M = A^{-1}$  is called the *magnification tensor*. We therefore define

$$\mu \equiv \det M = \frac{1}{\det A} = \frac{1}{(1 - \kappa)^2 - \gamma^2}. \quad (2.54)$$

The eigenvalues of the magnification tensor (or the inverse of the eigenvalues of the Jacobian matrix) measure the amplification in the direction of the eigenvectors of the shear tensor. For an axially symmetric lens, these are tangentially and radially oriented with respect to the lens iso-surface density contours. Thus, the quantities

$$\mu_t = \frac{1}{\lambda_t} = \frac{1}{1 - \kappa - \gamma} \quad (2.55)$$

$$\mu_r = \frac{1}{\lambda_r} = \frac{1}{1 - \kappa + \gamma} \quad (2.56)$$

are often called the *tangential* and *radial* magnification factors.

The magnification is ideally infinite where  $\lambda_t = 0$  and where  $\lambda_r = 0$ . These two conditions define two curves in the lens plane, called the *tangential* and the *radial critical lines*. An image forming near the tangential critical line is strongly distorted *tangentially* to the lens mass distribution. On the other hand, an image forming close to the radial critical line is stretched towards the lens center.

## 2.5 Lensing to the second order

We extend now the lens equation including the second order terms in the expansion of the deflection angle. The lens equation then becomes

$$\beta_i \simeq \frac{\partial \beta_i}{\partial \theta_j} \theta_j + \frac{1}{2} \frac{\partial^2 \beta_i}{\partial \theta_j \partial \theta_k} \theta_j \theta_k. \quad (2.57)$$

We introduce the tensor

$$D_{ijk} = \frac{\partial^2 \beta_i}{\partial \theta_j \partial \theta_k} = \frac{\partial A_{ij}}{\partial \theta_k}. \quad (2.58)$$

Then, Eq. 2.57 reads

$$\beta_i \simeq A_{ij} \theta_j + \frac{1}{2} D_{ijk} \theta_j \theta_k \quad (2.59)$$

By simple algebra, it can be shown that

$$D_{ij1} = \begin{pmatrix} -2\gamma_{1,1} - \gamma_{2,2} & -\gamma_{2,1} \\ -\gamma_{2,1} & -\gamma_{2,2} \end{pmatrix}, \quad (2.60)$$

and

$$D_{ij2} = \begin{pmatrix} -\gamma_{2,1} & -\gamma_{2,2} \\ -\gamma_{2,2} & 2\gamma_{1,2} - \gamma_{2,1} \end{pmatrix}. \quad (2.61)$$

Thus, the second order lensing effect can be expressed in terms of the derivatives of the shear (or in terms of the third derivatives of the potential).

### 2.5.1 Complex notation

It is quite useful to use complex notation to map vectors or pseudo-vectors on the complex plane. Indeed, in this case we can also use complex differential operators to write down some relations between the lensing quantities in a very concise way.

In complex notation, any vector or pseudo-vector  $v = (v_1, v_2)$  is written as

$$v = v_1 + i v_2 . \quad (2.62)$$

Similarly we can define the complex deflection angle  $\alpha = \alpha_1 + i \alpha_2$  and the complex shear  $\gamma = \gamma_1 + i \gamma_2$ .

It is also possible to define some complex differential operators, namely

$$\partial = \partial_1 + i \partial_2 \quad (2.63)$$

and

$$\partial^\dagger = \partial_1 - i \partial_2 . \quad (2.64)$$

Using this formalism, we can easily see that

$$\partial \hat{\Psi} = \partial_1 \hat{\Psi} + i \partial_2 \hat{\Psi} = \alpha_1 + i \alpha_2 = \alpha . \quad (2.65)$$

Moreover

$$\partial^\dagger \partial = \partial_1^2 + \partial_2^2 = \Delta . \quad (2.66)$$

Thus,

$$\partial^\dagger \partial \hat{\Psi} = \Delta \hat{\Psi} = 2\kappa . \quad (2.67)$$

Note that while  $\hat{\Psi}$  is a spin-0 scalar field, the application of the  $\partial$  operator gives the deflection angle, i.e. a spin-1 vector field. On the contrary, the  $\partial^\dagger$  operator applied to the deflection field gives another spin-0 scalar field (the convergence). Therefore, the  $\partial$  and  $\partial^\dagger$  operators can be considered as spin raising and lowering operators.

By applying twice the raising operator, we obtain

$$\frac{1}{2} \partial \partial \hat{\Psi} = \frac{1}{2} \partial \alpha = \gamma : \quad (2.68)$$

the shear field is indeed a spin-2 tensor field, which is invariant for rotations by multiples of  $\pi$ .

Note also that

$$\partial^{-1} \partial^\dagger \gamma = \frac{1}{2} \partial^{-1} \partial^\dagger \partial \partial \hat{\Psi} = \partial^\dagger \partial \hat{\Psi} = \kappa \quad (2.69)$$

We can use the raising and lowering operators to define

$$F = \frac{1}{2} \partial \partial^\dagger \partial \hat{\Psi} = \partial \kappa \quad (2.70)$$

$$G = \frac{1}{2} \partial \partial \partial \hat{\Psi} = \partial \gamma \quad (2.71)$$

After some math, it can be shown that

$$F = F_1 + i F_2 = (\gamma_{1,1} + \gamma_{2,2}) + i(\gamma_{2,1} - \gamma_{1,2}) \quad (2.72)$$

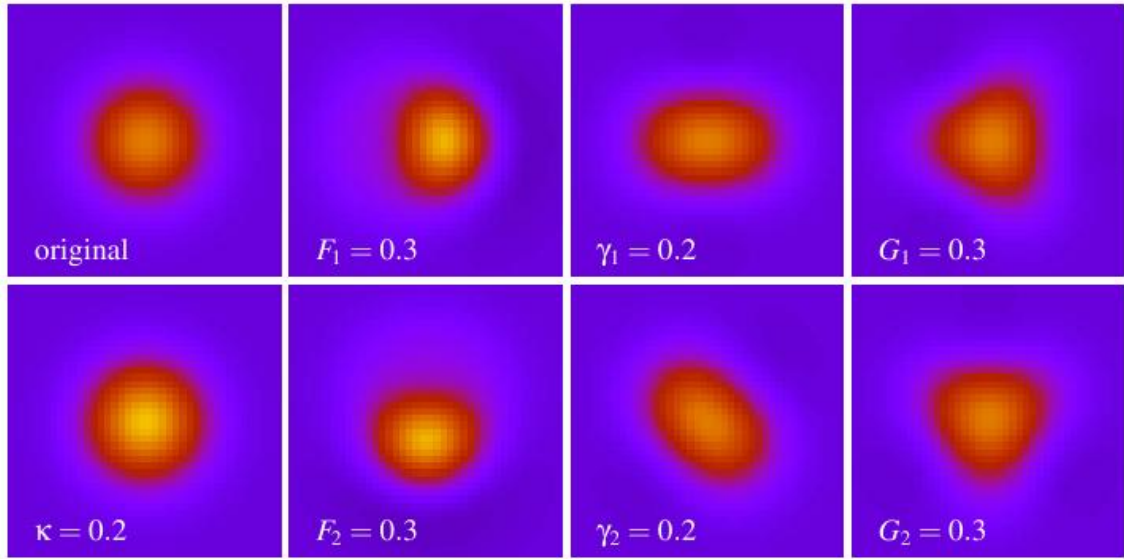


**Figure 2.5.1:** First and second order distortions on the image of a circular source. The unlensed source is shown in the top left panel. The convergence simply changes the size (bottom left panel). While the shear deforms the image such that it becomes elliptical (third column of panels from the left), the first and the second flexion introduce curvature and other distortions (second and fourth columns). Courtesy of Peter Melchior.

and

$$G = G_1 + iG_2 = (\gamma_{1,1} - \gamma_{2,2}) + i(\gamma_{2,1} + \gamma_{1,2}). \quad (2.73)$$

The quantities  $F$  and  $G$  are called *first and second flexion*, respectively. It is easy to show that  $D_{ijk}$  can be written in terms of  $F$  and  $G$ . Thus, they describe second order distortions of the images of lensed sources. Note that  $F$  is a spin-1 vector field. Indeed, it is

$$\vec{F} = \vec{\nabla} \kappa. \quad (2.74)$$

Thus, it describes transformations that are invariant under rotations by  $2\pi$ . For this reason,  $F$  stretches the images along one particular direction, introducing asymmetries in their shape. On the contrary,  $G$  is a spin-3 tensor field. The transformations described by  $G$  are invariant under rotations by  $2\pi/3$ . This is manifested in the "triangular" pattern in the image shapes, as shown in Fig. 2.5.1.

## 2.6 Occurrence of images

The deflection of light rays causes a delay in the travel-time of light between the source and the observer. This time delay has two components:

$$t = t_{\text{grav}} + t_{\text{geom}} \quad (2.75)$$

The first one is the *gravitational time delay*, also known as the Shapiro delay. It can be derived by comparing the time required for light to travel through a space-time with an effective refractive index and through empty space, by assuming *same trajectories*.

Let  $n = 1 - 2\Phi/c^2$  be the effective refractive index. We have that

$$t_{\text{grav}} = \int \frac{dz}{c'} - \int \frac{dz}{c} = \frac{1}{c} \int (n-1) dz = -\frac{2}{c^3} \int \Phi dz \quad (2.76)$$

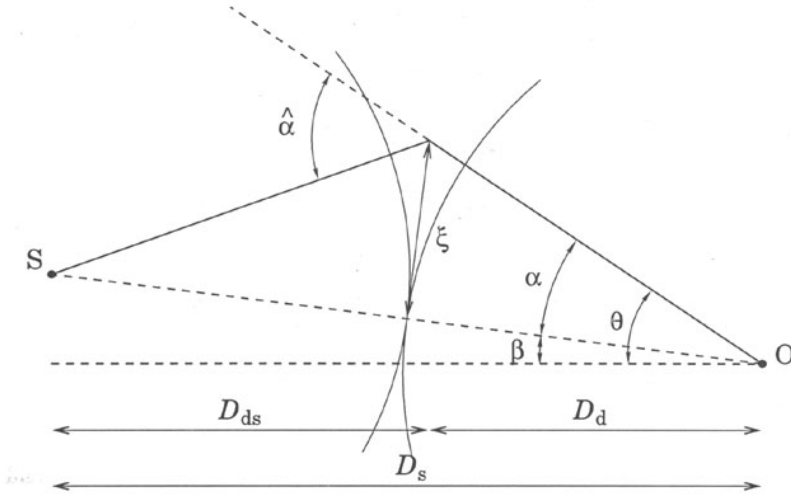


**Figure 2.6.1:** Illustration of the geometrical time delay.

Using the definition of the lensing potential, this can be written as

$$t_{\text{grav}} = -\frac{D_L D_S}{D_{LS}} \frac{1}{c} \hat{\Psi}. \quad (2.77)$$

The second term in the time delay is called *geometrical* and is due to the different path length of the deflected light rays compared to the unperturbed ones. This time delay is proportional to the squared angular separation between the intrinsic position of the source and the location of its image. This result can be derived from the metric, but it can be estimated also through a simple geometrical construction, shown in Fig. 2.6.1. The extra-path of the light in presence of the lens can be written as

$$\Delta l = \xi \frac{\hat{\alpha}}{2} = (\vec{\theta} - \vec{\beta}) \frac{D_L D_S}{D_{LS}} \frac{\vec{\alpha}}{2} = \frac{1}{2} (\vec{\theta} - \vec{\beta})^2 \frac{D_L D_S}{D_{LS}}, \quad (2.78)$$

and the corresponding time-delay is

$$t_{\text{geom}} = \frac{\Delta l}{c} \quad (2.79)$$

Both the time delays occur at the lens position, thus they need to be multiplied by a factor  $(1 + z_L)$  for accounting for the expansion of the universe. Then, the total time delay introduced by gravitational lensing at the position  $\vec{\theta}$  on the lens plane is<sup>1</sup>

$$\begin{aligned} t(\vec{\theta}) &= \frac{(1 + z_L)}{c} \frac{D_L D_S}{D_{LS}} \left[ \frac{1}{2} (\vec{\theta} - \vec{\beta})^2 - \hat{\Psi}(\vec{\theta}) \right] \\ &= \frac{D_{\Delta t}}{c} \tau(\vec{\theta}). \end{aligned} \quad (2.80)$$

The quantities

$$D_{\Delta t} = (1 + z_L) \frac{D_S D_L}{D_{LS}} \quad (2.81)$$

<sup>1</sup>The dimensionless form of the time delay can be obtained by multiplying and dividing by the factor  $(\xi_0/D_L)^2$ .

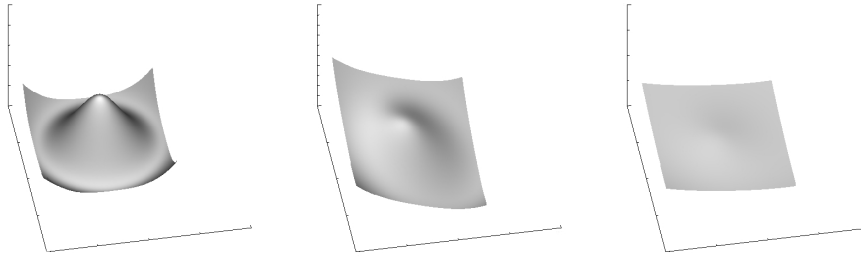


**Figure 2.6.2:** Time delay surfaces of an axially symmetric lens for three different source positions. Right panel: source and lens are perfectly aligned along the optical axis; middle panel: the source is no more aligned with the lens. Its projected position on the lens plane is moved along the line  $x_1 = x_2$ ; right panel: the source is moved to an even larger angular distance from the optical axis.

and

$$\tau(\vec{\theta}) = \frac{1}{2}(\vec{\theta} - \vec{\beta})^2 - \hat{\Psi}(\vec{\theta}), \quad (2.82)$$

are often called *time delay distance* and *Fermat potential*, respectively.

Through the effective lensing potential, the lens equation can be written as

$$(\vec{\theta} - \vec{\beta}) - \nabla \hat{\Psi}(\vec{\theta}) = \nabla \left[ \frac{1}{2}(\vec{\theta} - \vec{\beta})^2 - \hat{\Psi}(\vec{\theta}) \right] = 0. \quad (2.83)$$

Eqs. (2.80) and (2.83) imply that images satisfy the Fermat Principle,  $\nabla t(\vec{\theta}) = 0$ . Images therefore are located at the stationary points of the time delay surface given by Eq. (2.80). The Hessian matrix of this surface is

$$T = \frac{\partial^2 t(\vec{\theta})}{\partial \theta_i \partial \theta_j} \propto (\delta_{ij} - \Psi_{ij}) = A \quad (2.84)$$

We can distinguish between three types of image:

1. type I images arise at the minima of the time delay surface, where the eigenvalues of the Hessian matrix are both positive, hence  $\det A > 0$  and  $\text{tr} A > 0$ . Therefore, they have positive magnification;
2. type II images arise at the saddle points of the time delay surface, where eigenvalues have opposite signs. Since  $\det A < 0$ , they have negative magnification. The interpretation of a negative  $\mu$  is that the parity of the image is flipped compared to the source;
3. finally, type III images arise at the maxima of the time delay surface. Here, the eigenvalues are both negative, hence  $\det A > 0$  and  $\text{tr} A < 0$ . These images therefore have positive magnification.

Since the Hessian matrix describes the local curvature of the time delay surface, the smaller is the curvature along one direction at the position where the image forms, the larger is its magnification along the same direction. We display in Fig. (2.6.2) some examples of the time delay surface for a general axially symmetric lens with core. The density profile of this lens scales with radius as  $r^{-2}$  outside the core. The surfaces are plotted for three different source position  $\vec{\beta}$ : in the left panel the source and the lens are perfectly aligned along the optical axis passing through the lens center ( $\vec{y} = 0$  and  $\vec{\theta} = 0$ ); in the middle and right panel, the source is moved far away, increasing its angular distance from the optical axis. In order to better see where the minima and the maxima

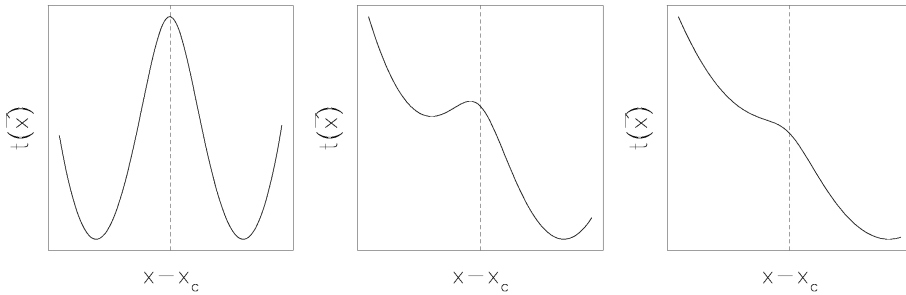


**Figure 2.6.3:** Profiles of the time delay surfaces displayed in Fig. (2.6.2) along the line  $x_1 = x_2$ .

arise, we show in Fig. (2.6.3) the profile along the line  $x_1 = x_2$  of the same surfaces. When the source and the lens are perfectly aligned, the minima of the time delay surface are located on a ring and the maximum is at the lens center. The source therefore is mapped to a ring image of type I (the so called *Einstein Ring*) and to a central type III image. This last one is generally demagnified, since the curvature of the time delay surface here is large for density profiles peaked at the lens center.

As the source is moved far away from the optical axis, the time delay surface deforms. In particular, the ring breaks, leading to the formation of a minimum and of a saddle point. Three images therefore arise. In the case displayed in the middle panel of Fig. (2.6.2), the type I image at the minimum and the type II image at the saddle point are stretched in the tangential direction, since the local curvature of the time delay surface is small in that direction. This explains the formation of tangential arcs in galaxy clusters. However, as the source is moved to even larger angular distances from the optical axis, the saddle point and the maximum move much closer to each other, while the minimum follows the source. The local curvature of the time delay surface in the radial direction becomes smaller between the saddle point and the maximum as they get closer. The images arising at these two points therefore are stretched towards each other. Then a radial image forms. When the saddle point and the maximum point touch, two images disappear and only the image arising at the minimum of the time delay surface remains (see right panels of Fig. (2.6.2) and Fig. (2.6.3)).

Here follows a number of other important properties of the time-delay surface:

- the height difference at different images of the surface  $t(\vec{\theta})$  gives the difference in arrival time between these images. This time delay can be measured if the source is variable, and provides one way of potentially measuring the Hubble constant;
- in absence of the lens, the time-delay surface is a parabola which has a single extremum (a minimum); additional extrema have to come in pairs, thus the total number of images must be odd (as we showed earlier by continuously deforming the time-delay surface);
- when two additional images are formed, they must be a maximum and a saddle point; in between them, the curvature changes from negative to positive, thus it is zero between them; remember that  $\det A = 0$  is the condition for having a critical point, where the magnification is (formally) infinite. The critical lines thus separate multiple-image pairs; these pairs merge and disappear (as discussed above) at the critical lines. In other words, the critical lines separate regions of different image multiplicities.

## 2.7 Python applications

### 2.7.1 Implementing a ray-tracing algorithm

In this exercise, we will implement a simple ray-tracing algorithm. In ray-tracing, we make use of the lens equation to propagate a bundle of light-rays from the observer position, through a regular

grid covering the lens plane, to the source plane. For each ray passing through the position  $\vec{x}^{ij}$ , we will evaluate the deflection angle  $\vec{\alpha}(\vec{x}^{ij})$  and compute the arrival position on the source plane as

$$\vec{y}^{ij} = \vec{x}^{ij} - \vec{\alpha}(\vec{x}^{ij}).$$

In the formula above,  $(i, j)$  identify the ray passing through the grid point with indexes  $i$  and  $j$  along the  $x_1$  and  $x_2$  axes, respectively.

The deflector used in this example is the same of the previous exercise. In particular, we will use the deflection angle maps shown in the upper panels of the figure above to propagate the light rays towards the sources.

We start by creating a mesh, where each grid-point has two coordinates. Suppose coordinates along the  $x_1$  and  $x_2$  axes are represented by the  $n_{pix}$ -dimensional vectors  $|x_1^i|$  and  $|x_2^j|$ , with  $i, j \in [1, n_{pix}]$  (so that  $n_{pix}$  is the number of grid points along one axis on the mesh). The mesh can be created using the `numpy.meshgrid` method, as e.g.

```
npix=angx.shape[0]
x1=np.linspace(0.0,1.0,npix)*(npix-1) # define x1 coordinates
x2=np.linspace(0.0,1.0,npix)*(npix-1) # define x2 coordinates
x1_,x2_=np.meshgrid(x1,x2) # lens plane mesh
```

will generate two numpy arrays, `x1_` and `x2_`, with size  $n_{pix} \times n_{pix}$ . In the first, the values on the  $i$ -th column will be equal to  $x_1^i$ ; in the second, the values on the  $j$ -th row will be equal to  $x_2^j$ .

We may now implement the lens equation for the two components along  $x_1$  and  $x_2$ :

```
y1=x1_-angx
y2=x2_-angy
```

In fact, we could arrive to the same result by using a feature in numpy called \*broadcasting\*. The term broadcasting describes how numpy treats arrays with different shapes during arithmetic operations. Subject to certain constraints, the smaller array is “broadcast” across the larger array so that they have compatible shapes.

Using this feature, we can write the first component of the lens equation as

$$\begin{bmatrix} y_1^{1,1} & \cdots & y_1^{1,n_{pix}} \\ \vdots & \ddots & \vdots \\ y_1^{n_{pix},1} & \cdots & y_1^{n_{pix},n_{pix}} \end{bmatrix} = B(n_{pix}, n_{pix}) \begin{bmatrix} x_1^1 \\ \vdots \\ x_1^{n_{pix}} \end{bmatrix} - \begin{bmatrix} \alpha_1^{1,1} & \cdots & \alpha_1^{1,n_{pix}} \\ \vdots & \ddots & \vdots \\ \alpha_1^{n_{pix},1} & \cdots & \alpha_1^{n_{pix},n_{pix}} \end{bmatrix}$$

The vector `x_1` is then broadcast to match the size of `alpha_1` (the broadcasting function is here indicated as  $B(n_{pix}, n_{pix})$ ). The result will be to add  $|x_1^i|$  to each column of the matrix  $-|\alpha_1^{ij}|$ .

Computing the coordinates  $|y_2^{ij}|$  involves few more steps. Again, using the lens equation, we obtain:

$$\begin{bmatrix} y_1^{1,1} & \cdots & y_1^{n_{pix},1} \\ \vdots & \ddots & \vdots \\ y_1^{1,n_{pix}} & \cdots & y_1^{n_{pix},n_{pix}} \end{bmatrix} = B(n_{pix}, n_{pix}) \begin{bmatrix} x_2^1 \\ \vdots \\ x_2^{n_{pix}} \end{bmatrix} - \begin{bmatrix} \alpha_1^{1,1} & \cdots & \alpha_1^{1,n_{pix},1} \\ \vdots & \ddots & \vdots \\ \alpha_1^{1,n_{pix}} & \cdots & \alpha_1^{n_{pix},n_{pix}} \end{bmatrix}$$

This equation implements the column-wise addition of  $|x_2^i|$  to  $-|\alpha_2^{ji}| = |\alpha_2^{ij}|^T$ , where  $T$  indicates the transposed matrix. The result is  $|y_2^{ij}| = |y_2^{ij}|^T$ .

The python implementation is quite easy:

```
y1=(x1-angx) # y1 coordinates on the source plane
y2=np.transpose(x2-np.transpose(angy)) # y2 coordinates
```

is not much difference between this approach and the previous one in terms of execution time and memory usage.

This example builds on the deflection angles derived in Sect. 1.5.2, for a numerically simulated dark matter halo. In this case the lens is at redshift  $z_L = 0.3$  and the source plane is at  $z_S = 2$ . The deflection angles are stored in the arrays `angx` and `angy` and the maps contain  $512 \times 512$  pixels. In

order to improve the visualization of the results, we downsample the maps by tracing a lower number of rays through the lens plane. We reduce the number of points on the lens plane mesh by a factor

```

ndown=16
x1=np.linspace(0.0,1.0,npix/ndown)*(npix-1) # downsampled x
x2=np.linspace(0.0,1.0,npix/ndown)*(npix-1) #
x1_,x2_=np.meshgrid(x1,x2) # downsampled grid
# now we need to interpolate the defl. angle maps at (x1_,
# we can use the method map_coordinates from scipy.ndimage
from scipy.ndimage import map_coordinates
# first, we need to reshape x1_ and y1_:
x=np.reshape(x1_,x1_.size)
y=np.reshape(x2_,x2_.size)
# then we interpolate:
angx_=map_coordinates(angx,[[y],[x]],order=1)
angy_=map_coordinates(angy,[[y],[x]],order=1)
# now we reshape the angles back to a mesh
angx_=angx_.reshape((npix/ndown,npix/ndown))
angy_=angy_.reshape((npix/ndown,npix/ndown))
y1=x1_-angx_
y2=x2_-angy_
# or
#y1=(x1-angx_)
#y2=np.transpose(x2-np.transpose(angy_))

```

result of this calculation is shown in Fig. 2.7.1. In the left panel, we show the regular grid on the lens plane, through which light-rays are traced starting from the observer position. In the right panel, we show the arrival positions of the light-rays on the source plane. We can see that 1) the grid on the source plane is no longer regular, as the consequence of the variations of the deflection angles across the field of view; 2) the source plane is crunched, specially near the center of the lens, where many points are brought very close to each other. This is a manifestation of the lensing magnification: a small area on the source plane is mapped onto a larger area on the lens plane.

## 2.7.2 Derivation of the lensing potential

Deriving the lensing potential from the lens convergence map requires to solve the Poisson equation in two dimensions (Eqs. 2.26 and 2.27). This can be done numerically by means of Fast-Fourier-Transform.

The Fourier transform of the Laplace operator is

$$\tilde{\Delta}(\vec{k}) = -4\pi^2 k^2$$

where  $k^2 = k_1^2 + k_2^2$ . Therefore, in Fourier space, the Poisson equation reads

$$-4\pi^2 k^2 \tilde{\Psi}(\vec{k}) = 2\tilde{\kappa}(\vec{k}).$$

The Fourier transform of the lensing potential is then

$$\tilde{\Psi}(\vec{k}) = -\frac{\tilde{\kappa}(\vec{k})}{2\pi^2 k^2}.$$

As shown in Sect. 1.5.2, the numerical calculation of the Fourier transforms can be implemented using e.g. the `numpy.fft` module. The following function could be added to the class `deflector` in

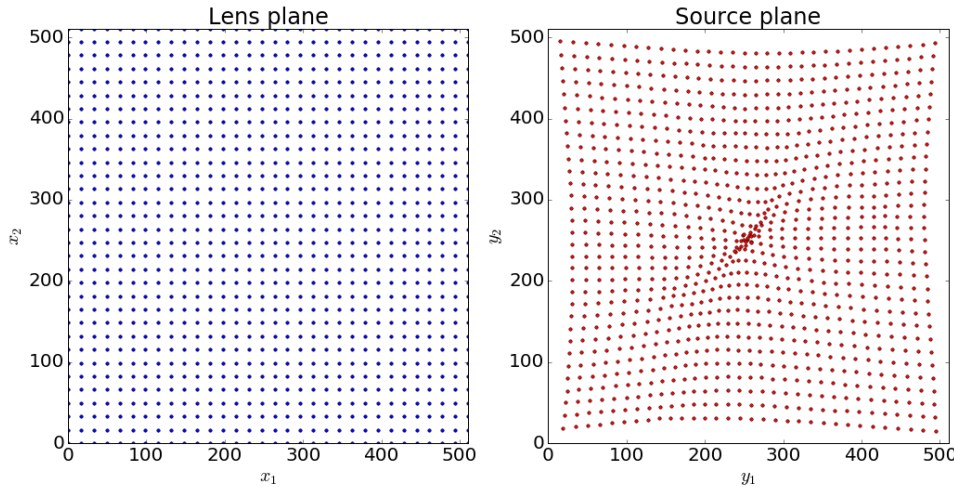


**Figure 2.7.1:** Ray-tracing through a regular grid on the lens plane (left panel). The arrival positions of the light-rays on the source plane are shown in the right panel. The lens is the same used in Sect. 1.5.2.

Sect. 1.5.2:

```
def potential(self):
    # define an array of wavenumbers (two components k1,k2)
    k = np.array(np.meshgrid(fftengine.fftfreq(self.kappa.shape[0])\
                           ,fftengine.fftfreq(self.kappa.shape[1])))
    pix=1 # pixel scale (now using pixel units)
    #Compute Laplace operator in Fourier space = -4*pi*l*l
    kk = k[0]**2 + k[1]**2
    kk[0,0] = 1.0
    #FFT of the convergence
    kappa_ft = fftengine.fftn(kappa)
    #compute the FT of the potential
    kappa_ft *= - pix**2 / (kk * (2.0*np.pi**2))
    kappa_ft[0,0] = 0.0
    potential=fftengine.ifftn(kappa_ft) #units should be rad**2
    return potential.real
```

We

```
pot=df.potential() # compute the
kappa=df.mapCrop(kappa) # remove
# converg
pot=df.mapCrop(pot)
```

can compute the lensing potential and display the resulting map as follows:

```
# display the results
fig,ax = plt.subplots(1,2,figsize=
ax[0].imshow(kappa,origin="lower")
ax[0].set_title('convergence')
ax[1].imshow(pot,origin="lower")
ax[1].set_title('potential')
```

The maps of the convergence and of the lensing potential for the lens considered are shown in Fig. 2.7.2. Clearly, the potential is much smoother than the convergence. This reflects the fact that the convergence is obtained by means of second derivatives of the potential.

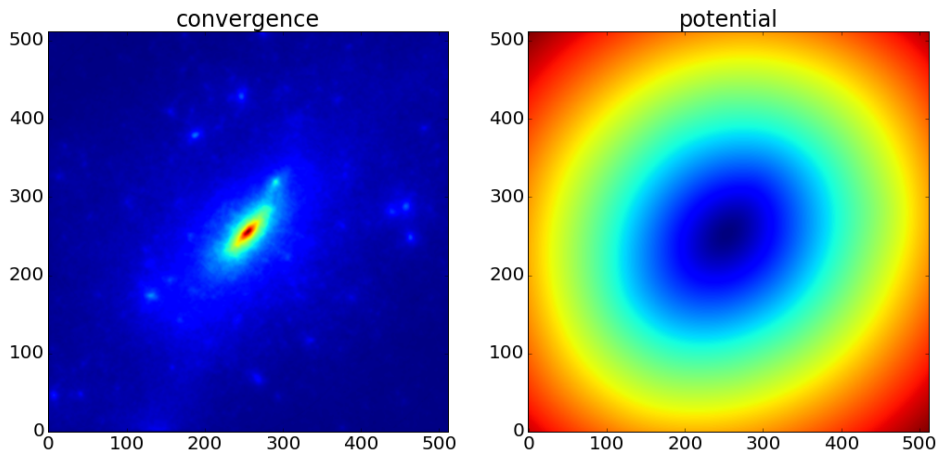


**Figure 2.7.2:** Maps of the convergence and of the lensing potential maps for the same lens used in Sect. 1.5.2

## 2.8 To be done

- use the relation between the potential and the convergence to derive the potential from the mass distribution
- use the potential to derive, via differentiation, the properties of the lens: convergence, shear, deflection angles, magnification
- apply lensing distortions to first and second order to a circular source.

# Part Two: Applications

<b>3</b>	<b>Microlensing</b>	<b>49</b>
3.1	The point mass lens	
3.2	Microlensing light-curve	
3.3	Photometric microlensing: optical depth and event rates	
3.4	Astrometric microlensing	
3.5	Multiple point masses	
3.6	Planetary microlensing	
3.7	Python applications	
3.8	Planetary microlensing	
<b>4</b>	<b>Extended lenses</b>	<b>85</b>
4.1	Axially symmetric lenses	
4.2	Power-law lens	
4.3	Softened (Isothermal) Lenses	
4.4	Time delays	
4.5	Other profiles	
4.6	Elliptical lenses	
4.7	Environment	
4.8	Substructures	
4.9	Mass-sheet degeneracy	
4.10	Python applications	
	<b>Bibliography</b>	<b>113</b>
	<b>Index</b>	<b>115</b>
<b>A</b>	<b>Python tutorial</b>	<b>115</b>
A.1	Installation	
A.2	Documentation	
A.3	Running python	
A.4	Your first python code	
A.5	Variables	
A.6	Strings	
A.7	Lists	
A.8	Tuples	
A.9	Dictionaries	
A.10	Blocks and Indentation	
A.11	IF / ELIF / ELSE	
A.12	While loops	
A.13	For loops	
A.14	Functions	
A.15	Classes	
A.16	Modules	
A.17	Importing packages	



### 3. Microlensing

This chapter is dedicated to microlensing, i.e. the lensing effects caused by lenses of very small size in the universe. In fact, a broad range of masses enter this class of lenses: from planets to stars. Given the small size of the lenses, microlenses are (to first order) assimilated to point masses or ensembles of point masses. Microlensing effects are mostly detectable and searched within our own galaxy, in particular by monitoring huge amounts of stars in the bulge of the Milky Way or towards the Magellanic clouds. Nevertheless, microlensing effects are relevant also in extragalactic gravitational lensing. Indeed, small mass lenses contained in galaxies other than ours produce small scale perturbations to the lensing signal of their hosts, which can be revealed in some situations.

#### 3.1 The point mass lens

##### Deflection angle and lensing potential

In Example 1.2, we derived the deflection angle of a point mass. By choosing the lens position as the center of the reference frame (i.e. by counting the angles  $\beta$  and  $\theta$  starting from the lens position), the deflection angle turns out to be

$$\hat{\vec{\alpha}} = \frac{4GM}{c^2} \frac{\vec{\xi}}{|\vec{\xi}|^2} = \frac{4GM}{c^2 D_L} \frac{\vec{\theta}}{|\vec{\theta}|^2}, \quad (3.1)$$

where, as usual, we have used the relation between the physical length  $\xi$  and the angle  $\theta$  given by the angular diameter distance  $D_L$ ,  $\xi = D_L \theta$ . Given that

$$\vec{\alpha} = \frac{D_{LS}}{D_S} \hat{\vec{\alpha}} = \vec{\nabla} \Psi \quad (3.2)$$

and that

$$\nabla \ln |\vec{x}| = \frac{\vec{x}}{|\vec{x}|^2}, \quad (3.3)$$

we can see that the lensing potential of the point mass lens is given by

$$\hat{\Psi}(\vec{\theta}) = \frac{4GM}{c^2} \frac{D_{LS}}{D_L D_S} \ln |\vec{\theta}|, \quad (3.4)$$

as we anticipated in Sect. ??.

### Lens equation

To derive the above equations, we chose the origin of the reference frame on the lens plane to be coincident with the position of the lens. The vector  $\hat{\alpha}$  points away from the lens. In fact, given the symmetry of the point mass, we may omit the vector sign in many of following equations. Then

$$\hat{\alpha} = \frac{4GM}{c^2\xi} = \frac{4GM}{c^2D_L\theta}. \quad (3.5)$$

The lens equation reads

$$\beta = \theta - \frac{4GM}{c^2D_L\theta} \frac{D_{LS}}{D_S}. \quad (3.6)$$

This is a quadratic equation in  $\theta$ , i.e. for a given position of the source  $\beta$  there always exist two images, whose positions can be determined by solving the lens equation.

### Multiple images

Eq. 3.6 can be written in a more concise way by introducing the *Einstein radius*,

$$\theta_E \equiv \sqrt{\frac{4GM}{c^2} \frac{D_{LS}}{D_L D_S}}. \quad (3.7)$$

The importance of this quantity will be clear shortly.

By inserting Eq. 3.7 into Eq. 3.6, we obtain

$$\beta = \theta - \frac{\theta_E^2}{\theta}. \quad (3.8)$$

Dividing by  $\theta_E$  and setting  $y = \beta/\theta_E$  and  $x = \theta/\theta_E$ , i.e. by expressing all angles in units of the Einstein radius, we obtain the adimensional the lens equation

$$y = x - \frac{1}{x}. \quad (3.9)$$

Multiplication with  $x$  leads to

$$x^2 - xy - 1 = 0, \quad (3.10)$$

which has two solutions:

$$x_{\pm} = \frac{1}{2} \left[ y \pm \sqrt{y^2 + 4} \right]. \quad (3.11)$$

The right panel of Fig. 3.1.1 shows a sequence of sources at different angular distances from the lens (indicated by a red star). Each source is shown using a different color, so that its images can be easily recognized in the left panel. For convenience the sources have been placed on the axis  $y_2 = 0$ .

Each source have two images, both on the axis  $x_2 = 0$ , but one with  $x_+ > 0$  and one with  $-1 < x_- < 0$ . Thus, they are on opposite sides with respect to the lens, and the image at  $x_-$  is always within a circle of radius  $x = 1$ . Such circle coincides with the image of the source at  $y = 0$ ,  $x_{\pm} = \pm 1$ ; that is, a source exactly behind the point lens has a ring-shaped image with radius  $\theta_E$ , also called *Einstein ring*. The size of the Einstein radius is

$$\begin{aligned} \theta_E &\approx (10^{-3})'' \left( \frac{M}{M_{\odot}} \right)^{1/2} \left( \frac{D}{10 \text{kpc}} \right)^{-1/2}, \\ &\approx 1'' \left( \frac{M}{10^{12} M_{\odot}} \right)^{1/2} \left( \frac{D}{\text{Gpc}} \right)^{-1/2}, \end{aligned} \quad (3.12)$$

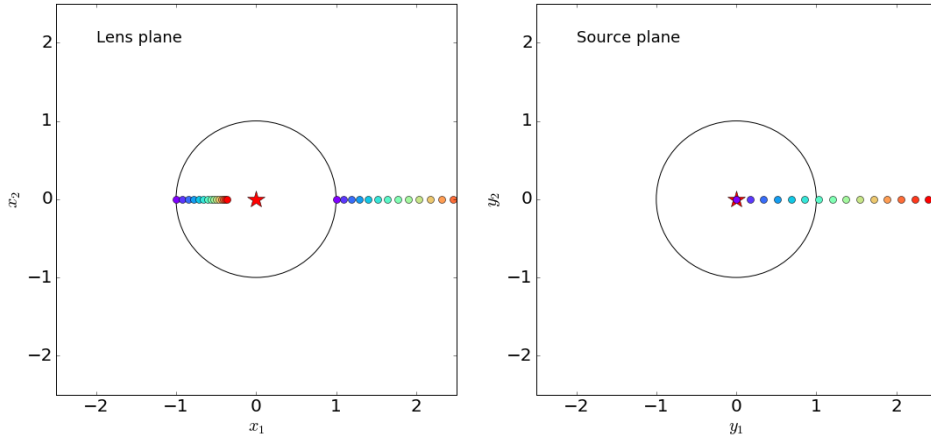


**Figure 3.1.1:** Solutions of the lens equation for a point mass lens. In both panels, the lens is given by the star at the center of the figure. The Einstein ring is shown in black. In the right panel, the positions of several source are indicated by colored circles. The corresponding images, as obtained by Eq. 3.11, are shown in the left panel.

where

$$D \equiv \frac{D_L D_S}{D_{LS}} \quad (3.13)$$

is the *effective lensing distance*.

As  $\beta \rightarrow \infty$ , we see that  $\theta_- = x_- \theta_E \rightarrow 0$ , while obviously  $\theta_+ = x_+ \theta_E \rightarrow \beta$ : when the angular separation between the lens and the source becomes large, the source is unlensed. Formally, there is still an image at  $\theta_- = 0$ , but as we have seen when discussing the properties of the time-delay surface, this central image are zero magnification.

### Critical lines, caustics, and magnification

Given that the lens is axially-symmetric, the Jacobian determinant is:

$$\det A(x) = -\frac{y \, dy}{x \, dx}. \quad (3.14)$$

From Eq. 3.14 and from Eq. 3.6, that the eigenvalues of the Jacobian matrix are

$$\begin{aligned} \lambda_t(x) &= \frac{y}{x} = \left(1 - \frac{1}{x^2}\right) \\ \lambda_r(x) &= \frac{dy}{dx} = \left(1 + \frac{1}{x^2}\right). \end{aligned} \quad (3.15)$$

Obviously, the second eigenvalue is never zero. Therefore, the point mass lens only have one critical line, namely a circle with equation  $x^2 = 1$ . This is the equation of the Einstein ring, which thus coincides with the tangential critical line.

Using the lens equation, as seen above, this line is mapped onto the tangential caustic, which is a point at  $\beta = 0$  ( $y = 0$ ).

The magnification is the inverse of the Jacobian determinant, thus

$$\mu(x) = 1 - \frac{1}{x^4}. \quad (3.16)$$

### Source magnification

From Eq. 3.11, we can see that, at the image positions,

$$\begin{aligned}\frac{x}{y} &= \frac{1}{2} \left( 1 \pm \frac{\sqrt{y^2+4}}{y} \right) \\ \frac{dx}{dy} &= \frac{1}{2} \left( 1 \pm \frac{y}{\sqrt{y^2+4}} \right).\end{aligned}\quad (3.17)$$

Thus, the image magnification can be written as a function of the source position as

$$\begin{aligned}\mu_{\pm}(y) &= \frac{1}{4} \left( 1 \pm \frac{\sqrt{y^2+4}}{y} \right) \left( 1 \pm \frac{y}{\sqrt{y^2+4}} \right) \\ &= \frac{1}{4} \left( 1 \pm \frac{\sqrt{y^2+4}}{y} \pm \frac{y}{\sqrt{y^2+4}} + 1 \right) \\ &= \frac{1}{4} \left( 2 \pm \frac{2y^2+4}{y\sqrt{y^2+4}} \right) = \frac{1}{2} \left( 1 \pm \frac{y^2+2}{y\sqrt{y^2+4}} \right) \\ &= \pm \frac{(y^2+2 \pm y\sqrt{y^2+4})}{2y\sqrt{y^2+4}} \\ &= \pm \frac{(2y^2+4 \pm 2y\sqrt{y^2+4})}{4y\sqrt{y^2+4}} \\ &= \pm \frac{(y \pm \sqrt{y^2+4})^2}{4y\sqrt{y^2+4}}.\end{aligned}\quad (3.18)$$

Thus, for  $y > 0$ ,  $\mu_-(y) < 0$  and  $\mu_+(y) > 0$ , showing that the parity of the two images is different.

The total source magnification is

$$\mu(y) = |\mu_+(y)| + |\mu_-(y)| = \frac{y^2+2}{y\sqrt{y^2+4}}, \quad (3.19)$$

while the sum of the *signed* magnifications is  $\mu = 1$ . By means of a power series expansion of the function above, we see that  $\mu \propto 1 + 2/y^4$  for  $y \rightarrow \infty$ , i.e. the magnification drops quickly as the source moves away from the lens.

The magnification ratio of the two images is

$$\begin{aligned}\left| \frac{\mu_+}{\mu_-} \right| &= \left( \frac{y+\sqrt{y^2+4}}{y-\sqrt{y^2+4}} \right)^2 \\ &= \left( \frac{x_+}{x_-} \right)^2.\end{aligned}\quad (3.20)$$

We can see that  $\lim_{y \rightarrow \infty} \mu_- = 0$  and that  $\lim_{y \rightarrow \infty} \mu_+ = 1$ . Moreover, a power series expansion shows that for large  $y$ ,

$$\left| \frac{\mu_+}{\mu_-} \right| \propto y^4, \quad (3.21)$$

i.e. the image at  $x_+$  dominates the magnification budget pretty quickly as the source is moved away from the lens.

### Microlensing cross section

A source at  $y = 1$  has two images at

$$x_{\pm} = \frac{1 \pm \sqrt{5}}{2}, \quad (3.22)$$

and their magnifications are

$$\mu_{\pm} = \left[ 1 - \left( \frac{2}{1 \pm \sqrt{5}} \right)^4 \right]^{-1}. \quad (3.23)$$

Thus, the total source magnification is  $\mu = |\mu_+| + |\mu_-| = 1.17 + 0.17 = 1.34$ . In terms of magnitudes, this correspond to  $\Delta m = -2.5 \log \mu \sim 0.3$  only. The image at  $x_+$  contributes for  $\sim 87\%$  of the total magnification. As seen above, for  $y > 1$  the magnification drops quickly meaning that the only chance to detect microlensing events via magnification effects is by finding sources well aligned with the lenses, i.e. within their Einstein rings. For this reason, the area of the Einstein ring is generally assumed to be the cross-section for microlensing,

$$\sigma_{\text{micro}} = \pi \theta_E^2. \quad (3.24)$$

This is the solid angle within which a source has to be placed in order to produce a detectable microlensing signal.

## 3.2 Microlensing light-curve

The order-of-magnitude of the image separation in microlensing events is given by the Einstein radius of the typical lens. As seen above, for a one solar-mass star within our galaxy, this is of the order of  $\sim 10^{-3}$  arcseconds, thus undetectable with the current instrumentation.

Microlenses in the Milky Way or its surrounding can however be detected by exploiting the relative motion of the lenses and of the sources, due to the (differential) rotation of our own galaxy. If the source and the lens are in relative motion, i.e. if the relative distance between the lens and the source,  $y$ , is a function of time, then Eq. 3.19 shows that the magnification is a function of time as well,  $\mu \equiv \mu(t)$ . Therefore, a source with intrinsic flux  $f_s$  will appear to have a flux  $f(t) = \mu(t)f_s$ , while being lensed. The curve describing the variation of the source flux as a function of time during the microlensing event is called the *microlensing light-curve*.

We assume that the relative path of the source with respect to the lens can be approximated by a straight line, as shown by the blue-dashed line in the diagram in Fig. 3.2.1. The source (indicated by the blue dot) reaches the minimum dimensionless distance  $y_0$  from the lens at time  $t_0$ .  $y_0$  is the dimensionless *impact parameter* of the source. Assuming that the source moves with transverse velocity  $v$  relative to the lens, we can write the dimensionless distance of the source from the point of minimum distance from the lens as

$$y_1(t) = \frac{v(t - t_0)}{D_L \theta_E}, \quad (3.25)$$

where  $D_L$  indicates, as usual, the angular diameter distance between the observer and the lens.

If the source moves at velocity  $v$ , it will take a time

$$t_E = \frac{D_L \theta_E}{v} = \frac{\theta_E}{\mu_{\text{rel}}} \quad (3.26)$$

to cross the Einstein radius of the lens. In the equation above, we have introduced the relative proper motion of the source with respect to the lens,  $\mu_{\text{rel}} = v/D_L$ . Since, as we discussed in the

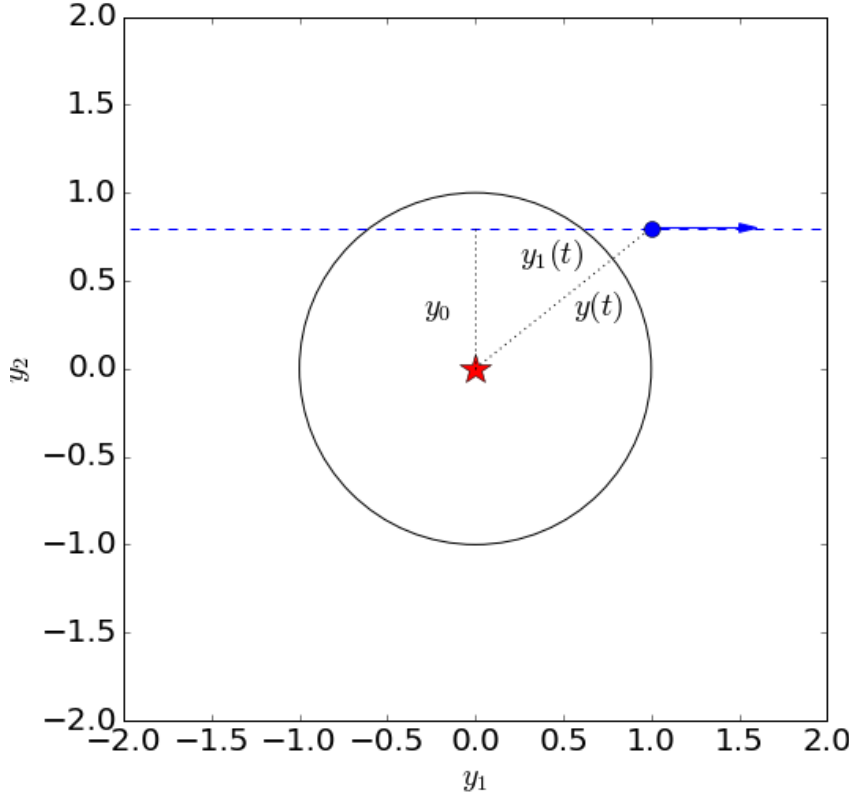


**Figure 3.2.1:** Illustration for the lens position and source trajectory. The dimensionless impact parameter is  $y_0$ .  $y_1(t)$  is the dimensionless distance of the source from the point of minimum distance from the lens. Finally,  $y(t)$  is the dimensionless distance of the source from the lens.

previous section, the magnification significantly deviates from unity only for sources with  $|y| \lesssim 1$ , we can assume that the *Einstein radius crossing time*,  $t_E$ , is the timescale of the microlensing event. If we use the definition of Einstein radius given in Eq. 3.7, we see that

$$t_E \approx 19 \text{ days} \sqrt{4 \frac{D_L}{D_S} \left(1 - \frac{D_L}{D_S}\right)} \left(\frac{D_S}{8 \text{kpc}}\right)^{1/2} \left(\frac{M}{0.3 M_\odot}\right)^{1/2} \left(\frac{v}{200 \text{km/s}}\right)^{-1} \quad (3.27)$$

To write this equation, we have used the approximation  $D_{LS} = D_S - D_L$ , which is valid only for non-cosmological distances, and thus applies in our galaxy.

Inserting Eq. 3.26 into Eq. 3.25, we obtain:

$$y_1(t) = \frac{(t - t_0)}{t_E}. \quad (3.28)$$

Thus,

$$y(t) = \sqrt{y_0^2 + y_1^2(t)} = \sqrt{y_0^2 + \frac{(t - t_0)^2}{t_E^2}}. \quad (3.29)$$

Combining Eqs. 3.29 and 3.19, we obtain the microlensing light-curve. Some examples of light-curves corresponding to different values of the impact parameter  $y_0$  are shown in Fig. 3.2.2.

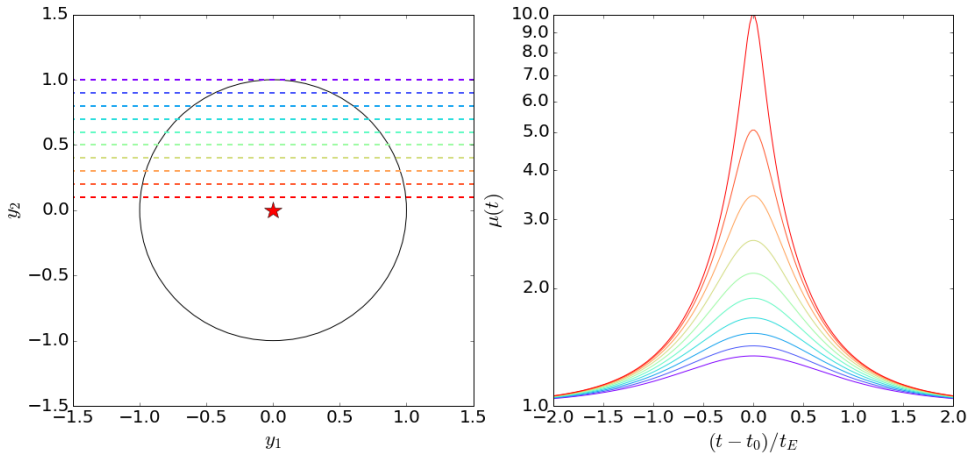


**Figure 3.2.2:** Left panel: source trajectories corresponding to different values of the impact parameter  $y_0$ , varying from 0.1 (red) to 1 (purple). Right panel: color-coded light-curves corresponding to the source trajectories displayed in the left panel.

### 3.2.1 Light-curve fitting

The shape of the *standard* microlensing light-curve is characterized by a peak which occurs at  $t_0$ . The peak height is determined by the value of  $y_0$ : the closer the source trajectory passes to the lens, the higher is the peak. The peak width is instead determined by  $t_E$ , which in turn depends on the lens mass, the relative transverse velocity, the lens and the source distances. Therefore from an observed light curve well fitted by the standard model, one cannot infer the distances, the velocity, and the lens mass uniquely. This is the so-called *microlensing degeneracy*. However, given a lens mass function and some kinematic model of the Milky Way, we can infer the lens masses statistically.

In addition, to fit an observed light-curve we need the baseline flux  $f$ . Generally, a *blending parameter*,  $b_s$ , which describes the fraction of light contributed by the lensed source is also included. In presence of crowded fields, the measured flux is indeed the sum of the flux from the source, from the lens, and from other unrelated stars within the seeing disk. Since these may be wavelength dependent, the blending parameter is generally different in different filters. Note that blending biases the magnification estimate low.

While the standard light-curve model works well in about 90% of the cases, there are situations where one or more of the assumptions at the basis of the standard model break down. In these *exotic* cases, it may be possible to derive extra constraints which help to partially lift the microlensing degeneracy. Non-standard light-curves occur, for example, when the source or the lens are not point-like (finite source size and finite lens size effects) or when the motion of the source relative to the lens is not linear. This is the case when the lens and/or the source are in binary systems, for example.

If the lens has finite size, one can always find a time interval when the lens obscures the inner (and the outer, depending on the lens size) lensed image in the early rising stage and in the final declining stage of the light curve. This is shown in Fig. 3.2.3, taken from (Lee et al., 2009). Thus, the impact of these effects is to dim the wings of the light curve.

The finite source size effect occurs when the size of the source is not negligible and it is particularly important in the high-magnification limits (Gould, 1994; Lee et al., 2009; Witt and Mao, 1994). In this case, the light-curve is broadened near the peak, as the result of the fact that different parts of the source experience different magnifications. Assuming that the surface

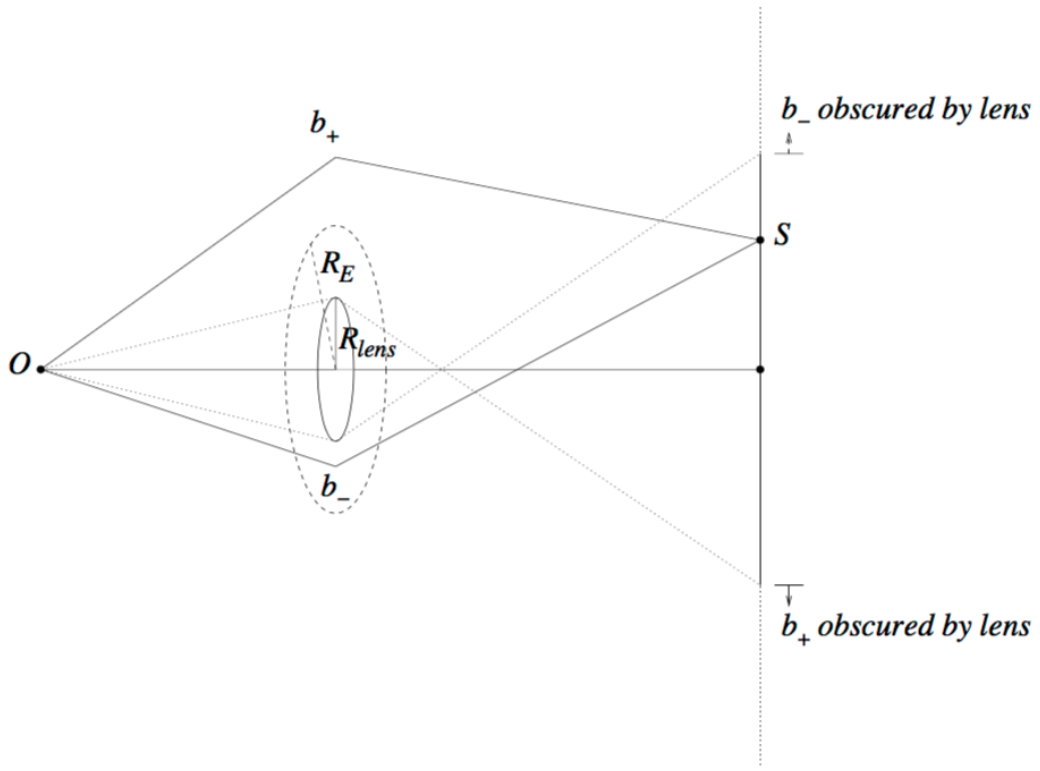


**Figure 3.2.3:** Illustration of the finite lens size effect. Depending on the distance of the source from the center of the finite lens, the images in  $x_+$  or in  $x_-$  (here indicated with  $b_{\pm}$ ) are obscured. Figure from (Lee et al., 2009).

brightness of the source is uniform, the magnification near the peak of the light curve can be approximated by the following formula (Gould, 1994):

$$\mu'(y) \simeq \mu(y) \frac{4y}{\pi\rho} E(\vartheta_{max}, y/\rho), \quad (3.30)$$

where  $E(\vartheta, \varphi)$  is the Elliptical integral of the second kind and  $\vartheta$  is defined as

$$\vartheta_{max} = \begin{cases} \frac{\pi}{2} & y \leq \rho \\ \arcsin(\rho/y) & y > \rho \end{cases}. \quad (3.31)$$

An example of light-curve being fitted including both finite source and lens size effects is shown in Fig. 3.2.4.

### 3.3 Photometric microlensing: optical depth and event rates

After deriving the shape of the light-curve, we estimate now the frequency of photometric microlensing events.

#### 3.3.1 Optical depth

The optical depth to some distance  $D_S$  is the probability that a source at that distance gives rise to a detectable microlensing event. As discussed earlier, we can assume that the lens cross section (in steradians) coincides with the solid angle enclosed by the Einstein ring,  $\pi\theta_E^2$ . Therefore, the optical depth can be computed as the sum of the cross sections of all lenses up to distance  $D_S$ , divided by

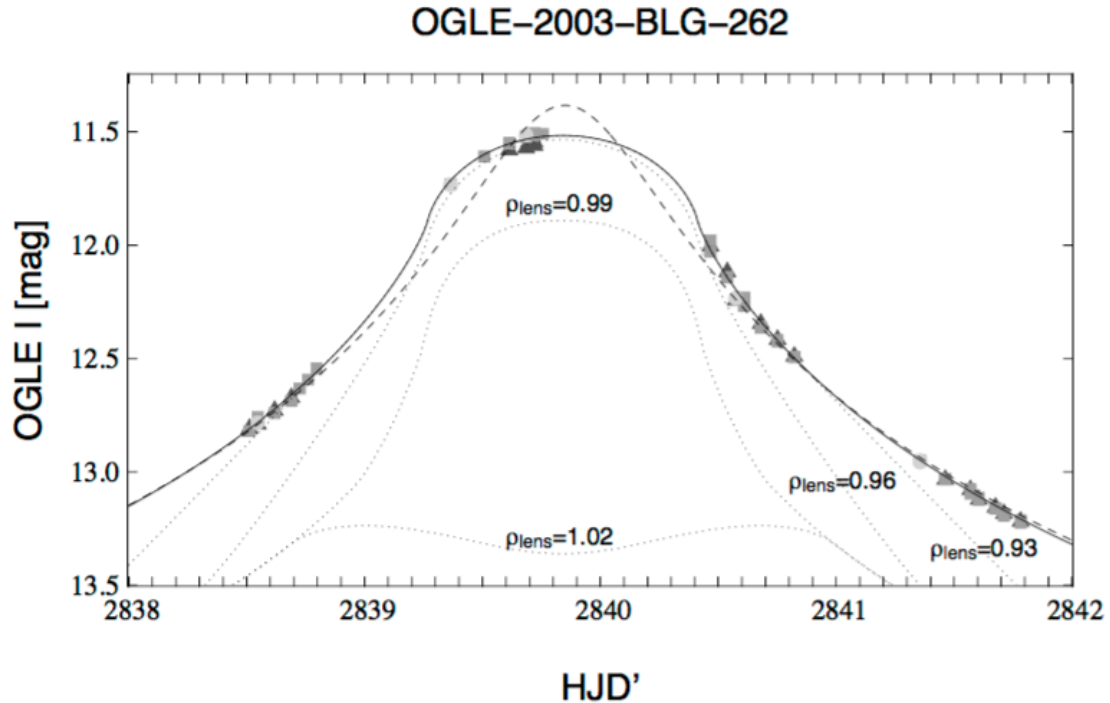


**Figure 3.2.4:** Light curve of the microlensing event OGLE-2003-BLG-262. The shape of the light curve is fitted with a model which accounts for finite source size effects (solid line). The dotted lines illustrate the effects of finite lens sizes on top of finite-source size for lens sizes of  $\rho_{\text{lens}} = 0.93, 0.96, 0.99$ , and  $1.02$ . Figure from (Lee et al., 2009).

the area of the sky. Let assume that the number density of lenses varies as a function of the lens distance as  $n(D_L)$ . Then, the number of lenses in the spherical shell centered on the observer and with radius  $D_L$  to  $D_L + dD_L$  is

$$dN_L = 4\pi D_L^2 n(D_L) dD_L. \quad (3.32)$$

Thus, the optical depth is

$$\tau(D_S) = \frac{1}{4\pi} \int_0^{D_S} [4\pi D_L^2 n(D_L)] (\pi \theta_E^2) dD_L. \quad (3.33)$$

If all lenses have the same mass  $M$ , then  $n(D_L) = \rho(D_L)/M$ , where  $\rho(D_L)$  is the mass density. Note that, since  $\theta_E \propto M^{1/2}$ , the optical depth depends on the total mass density but not on the lens mass. This result can be generalized also to the case where the lens have a mass distribution (a.k.a. the *lens mass function*), if the spatial distribution of the lenses is independent on the mass. Indeed, we can write

$$n(D_L) = \int n(D_L, M) dM = \int \rho_M(D_L) M^{-1} dM. \quad (3.34)$$

Under this assumption, and using Eq. 3.7, we obtain

$$\begin{aligned} \tau(D_S) &= \frac{4\pi G}{c^2} \int_0^{D_S} \rho(D_L) D_L^2 \frac{D_{LS}}{D_L D_S} dD_L \\ &= \frac{4\pi G}{c^2} \int_0^{D_S} \rho(D_L) D_L \frac{D_S - D_L}{D_S} dD_L \\ &= \frac{4\pi G}{c^2} \int_0^{D_S} \rho(D_L) \frac{D_L}{D_S} \left(1 - \frac{D_L}{D_S}\right) D_S dD_L. \end{aligned} \quad (3.35)$$

Setting  $x = D_L/D_S$ ,  $dx = dD_L/D_S$ , the optical depth is thus

$$\tau(D_S) = \frac{4\pi G}{c^2} D_S^2 \int_0^1 \rho(x)x(1-x)dx . \quad (3.36)$$

By taking the derivative with respect to  $x$ , we see that

$$\frac{d\tau}{dx} \propto \rho(x)x(1-x) . \quad (3.37)$$

The function  $f(x) = x(1-x)$ , which weights the contribution of lenses to the optical depth, has a maximum at  $x = 0.5$ , i.e. the lenses which are located about half way between the observer and the sources contribute the most to the optical depth. However, one has to consider  $\rho(x)$  to establish where most of the microlensing signal comes from.

If we assume, for simplicity,  $\rho(x) = \rho_0 = \text{const.}$ , then we obtain

$$\tau(D_S) = \frac{4\pi G}{c^2} \rho_0 D_S^2 \int_0^1 x(1-x)dx = \frac{2}{3} \frac{\pi G}{c^2} D_S^2 \rho_0 . \quad (3.38)$$

Let's consider the case of microlensing in the Milky Way. The sphere centered on the center of the galaxy and with radius  $D_S$  contains a mass  $M_{gal} = \frac{4}{3}\pi D_S^3 \rho_0$ , thus

$$\tau(D_S) = \frac{GM_{gal}}{2c^2 D_S} = \frac{V_{circ}^2}{2c^2} . \quad (3.39)$$

where  $V_{circ} \approx 220$  km/s is the circular velocity. Assuming that the sources are all at galactocentric distance, the optical depth for microlensing is

$$\tau \approx 2.6 \times 10^{-7} . \quad (3.40)$$

Thus we need to monitor many millions of stars in order to have a realistic yield of microlenses, meaning that observational campaigns have to target regions where the numerical density of stars is very high. In fact, several microlensing experiments have been carried out since the 90's, which have targeted the galactic bulge and the Magellanic Clouds.



The calculations reported above assume that the mass density of lenses is constant. However, this is an over-simplification: in the case of microlensing towards the galactic bulge, we should account for the far more complex structure of our galaxy, which includes several components (bulge, bar, disk, halo), each of which have its own mass density.

**Exercise 3.1 — Optical depth of an exponential disk.** We report here the calculations for computing the optical depth to the galactic center for a distribution of lenses resembling the galactic disk (i.e. having an exponential density profile). This exercise was proposed in the nice review paper by [2008arXiv0811.0441M](#)

The mass density in the exponential disk is described, with respect to an observer near the sun, by the function

$$\rho(R) = \rho_0 \exp(-(R - R_0)/R_D) , \quad (3.41)$$

where  $\rho_0$  is the mass density in the solar neighborhood,  $R$  is the distance of the lens from the galactic center,  $R_0$  is the distance of the sun from the galactic center and  $R_D$  is the disk scale (i.e. a parameter which defines how quickly the density falls as a function of radius). Using the standard notation, we have that  $R = D_{LS}$  and  $R_0 = D_S$ , thus

$$\rho(D_L) = \rho_0 \exp(D_L/R_D) . \quad (3.42)$$

Scaling the distances by  $D_S$ , the density can be written as

$$\rho(x) = \rho_0 \exp x/x' , \quad (3.43)$$

where  $x' = R_D/D_S$ . This can be inserted into Eq. 3.36 to obtain

$$\tau(D_S) = \frac{4\pi G}{c^2} \rho_0 D_S^2 \int_0^1 \exp(x/x') x(1-x) dx . \quad (3.44)$$

Solving the last integral, we find that

$$\tau(D_S) = \frac{4\pi G}{c^2} \rho_0 D_S^2 x'^2 [2x' - 1 + \exp(1/x')(2x' - 1)] ; . \quad (3.45)$$

Assuming  $D_S = 8$  kpc,  $R_D = 3$  kpc,  $\rho_0 = 0.1 M_\odot \text{pc}^{-3}$ , we obtain

$$\tau \approx 2.9 \times 10^{-6} . \quad (3.46)$$

■

### 3.3.2 Event rate

While the optical depth gives the probability that a source is undergoing a microlensing event at any given instant, we are interested in knowing what is the rate of microlensing events we may see while monitoring a certain number of sources for a certain time.

To calculate the event rate it is more natural to imagine that sources form a static background in front of which lenses move at some transverse velocity  $v$ . For simplicity, we can assume that this velocity is the same for all the lenses (although, in a realistic case, both the lenses and the sources have some velocity distributions). The lens cross section has diameter  $2r_E$ , where  $r_E$  is the physical size of the Einstein radius on the lens plane,  $r_E = D_L \theta_E$ . In order to compute the probability to observe a microlensing event in a given time  $dt$ , we have to consider that the lens, while moving in front of the sources at velocity  $v$ , swipes a certain area. The area swept in the time  $dt$  is

$$dA = 2r_E v dt = 2r_E^2 \frac{dt}{t_E} . \quad (3.47)$$

Multiplying by the number density of lenses between  $D_L$  and  $D_L + dD_L$ , we obtain the probability that a source undergoes a new microlensing event in the time  $dt$

$$d\tau = \int_0^{D_S} n(D_L) dA dD_L = 2 \int_0^{D_S} n(D_L) r_E^2 \frac{dt}{t_E} dD_L . \quad (3.48)$$

If we monitor  $N_\star$  sources during the time  $dt$ , we obtain the expected number of microlensing events observed by multiplying the probability that one source undergoes a microlensing event by the number of stars monitored. Finally, by dividing by the time  $dt$ , we obtain the *event rate*:

$$\Gamma = \frac{d(N_\star \tau)}{dt} = \frac{2N_\star}{\pi} \int_0^{D_S} n(D_L) \frac{\pi r_E^2}{t_E} dD_L . \quad (3.49)$$

Assuming that all the Einstein crossing times are identical, we obtain

$$\Gamma = \frac{2N_\star}{\pi t_E} \tau . \quad (3.50)$$

Therefore, if  $t_E \approx 19$  days,

$$\Gamma \approx 1200 \text{yr}^{-1} \frac{N_\star}{10^8} \frac{\tau}{10^{-6}} \left( \frac{t_E}{19 \text{days}} \right)^{-1} , \quad (3.51)$$

meaning that by monitoring  $\sim 10^8$  stars, we would expect to observe  $\sim 1200$  microlensing events per years. For comparison, the OGLE-III collaboration, by monitoring  $2 \times 10^8$  stars in the galactic bulge, detected  $\sim 600$  events. This may indicate that the detection efficiency is of the order of  $25 - 30\%$ .

Note that while the optical depth does not depend on the mass, the event rate is mass-dependent, because  $\Gamma \propto t_E^{-1} \propto M^{-1/2}$ . This is very important, because it means that we can use the distribution of event timescales to probe the kinematics of the Milky Way and the stellar population in the galaxy.

### 3.4 Astrometric microlensing

While the totality of microlensing events (to my knowledge) has been observed so far only photometrically, there is another potential way to detect microlensing which is becoming possible thanks to the dramatic improvements in the precision of astrometric measurements. The GAIA satellite, for example, is performing micro-arcsecond ( $\mu\text{as}$ ) global astrometry for nearly  $10^9$  stars down to magnitude  $G 20$ .

The idea behind the so-called *astrometric microlensing* is the following (1995A&A...294..287H; 1995AJ....110.1427M; 1995AJ....110.1427M; 1998astro.ph..5360D; 2011A&A...536A..50P). During the microlensing event, the positions as well as the relative magnifications of the images vary as a function of time. Consequently, the light-centroid of the images will reflect this time variation and will move along a trajectory which can be calculated easily.

First of all, we consider the motion of the images forming outside and inside the Einstein ring in response to the motion of the source. The vector indicating the source position as a function of time,  $\vec{y}(t)$ , has two components, namely  $y_{\parallel} = (t - t_0)/t_E$  and  $y_{\perp} = y_0$ , along and perpendicular to the direction of motion of the source, respectively. The two images always lay on the line passing through the lens and the source. Their distances from the lens in units of the Einstein radius are given in Eq. 3.11. For the images external and internal to the Einstein ring, we have that

$$\begin{aligned} x_{\pm,\parallel} &= \frac{1}{2}(1 \pm Q)y_{\parallel} \\ x_{\pm,\perp} &= \frac{1}{2}(1 \pm Q)y_{\perp}, \end{aligned} \quad (3.52)$$

where

$$Q = \frac{\sqrt{y^2 + 4}}{y}. \quad (3.53)$$

The path of the two images is shown for a source moving on a trajectory with  $y_0 = 0.2$  in Fig. 3.4.1.

The corresponding magnifications are given in Eq. 3.18. The light centroid of the images can be computed as

$$\vec{x}_c = \frac{\vec{x}_+ |\mu_+| + \vec{x}_- |\mu_-|}{|\mu_+| + |\mu_-|}. \quad (3.54)$$

As discussed in Sect. 3.1, the magnified flux received from the two images is strongly unbalanced in favor of the image external to the Einstein radius for most of the time. Therefore, the light centroid will be generally pulled towards the external image.

In practice, when monitoring a source, one will detect a shift compared to the unlensed position. This shift is given by

$$\delta \vec{x}_c = \vec{x}_c - \vec{y}. \quad (3.55)$$

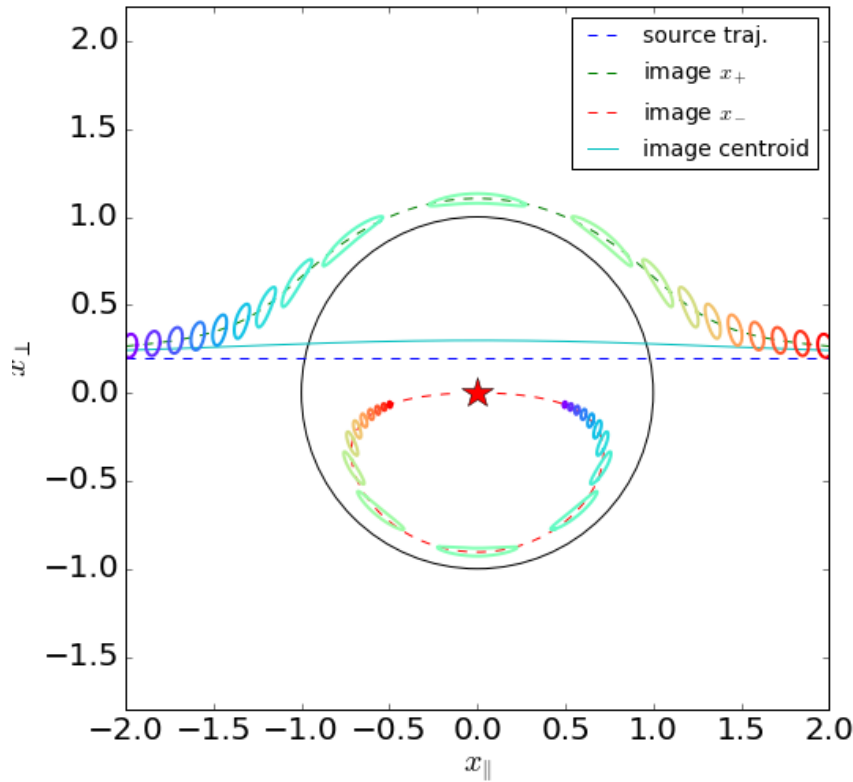


**Figure 3.4.1:** Illustration of a microlensing event. The source trajectory (corresponding to an impact parameter  $y_0 = 0.2$ ) is given by the dashed line. The red star indicates the lens position in  $(0,0)$ . The green and the red dashed lines show the trajectories of the images external and internal to the Einstein ring (black circle), respectively. For better visualizing the magnification of the images, we assign to the source a circular shape. As the source moves from left to right, the color of the two images changes from blue to red. Obviously, the size of the external image is always bigger than the size of the internal image, showing that the former will generally provide a larger fraction of the flux. As a consequence, the light centroid will follow a path (cyan solid line) which will differ from the path of the source, being pulled towards the external image.

As shown in Fig. 3.4.2, this has the characteristic shape of an ellipse. The axis ratio of the ellipse and its extension depend on the impact parameter of the source,  $y_0$ , as it will be discussed below.

Since the lens, the source and the images must be aligned on the plane of the sky,  $\vec{x}_c$  and  $y$  in Eq. 3.55 are aligned too. Thus, using Eqs. 3.11 and 3.18, we can compute the amplitude of the shift

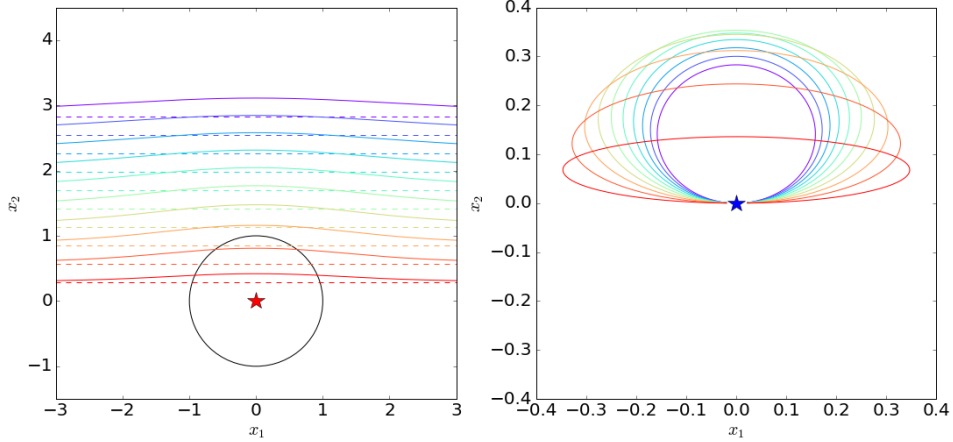


**Figure 3.4.2:** Left panel: Light centroid trajectories (solid lines) for sources with decreasing impact parameter (from blue to red). The unlensed source trajectories are given by the dashed lines. Right panel: the corresponding centroid shifts from the unlensed source paths.

as

$$\begin{aligned}
 \delta x_c &= \frac{\frac{1}{4} \left[ (y + \sqrt{y^2 + 4}) \left( 1 + \frac{y^2 + 2}{y\sqrt{y^2 + 4}} \right) - (y - \sqrt{y^2 + 4}) \left( 1 - \frac{y^2 + 2}{y\sqrt{y^2 + 4}} \right) \right]}{\frac{y^2 + 2}{y\sqrt{y^2 + 4}}} - y \\
 &= \frac{\frac{1}{4} \left( y + \sqrt{y^2 + 4} + \frac{y^2 + 2}{\sqrt{y^2 + 4}} + \frac{y^2 + 2}{y} - y + \sqrt{y^2 + 4} + \frac{y^2 + 2}{\sqrt{y^2 + 4}} - \frac{y^2 + 2}{y} \right)}{\frac{y^2 + 2}{y\sqrt{y^2 + 4}}} - y \\
 &= \frac{y}{y^2 + 2}.
 \end{aligned} \tag{3.56}$$

Given the sign,  $\delta \vec{x}_c$  points in the same direction of  $\vec{y}$ . An interesting property is that, for  $y \gg \sqrt{2}$ ,

$$\delta x_c \approx \frac{1}{y}, \tag{3.57}$$

meaning that the amplitude of the astrometric microlensing effect decreases with the distance of the source from the lens much slower than the photometric microlensing effect. In addition,

$$\frac{d(\delta x_c)}{dy} = \frac{2 - y^2}{(y^2 + 2)^2}, \tag{3.58}$$

which shows that the shift has a maximum amplitude for  $y = \sqrt{2}$ , where  $\delta x_c = \delta x_{c,max} = (2\sqrt{2})^{-1} \approx 0.354$ . Assuming  $\theta_E \approx 1$  mas, then  $\delta \theta_c = \delta x_c \theta_E \approx 1/3$  mas, which is well above the accuracy of GAIA.

We can now decompose the shift into the components parallel and perpendicular to the source trajectory:

$$\delta x_{c,\parallel} = \frac{y_{\parallel}}{y^2 + 2} = \frac{(t - t_0)/t_E}{[(t - t_0)/t_E]^2 + y_0^2 + 2} \tag{3.59}$$

$$\delta x_{c,\perp} = \frac{y_{\perp}}{y^2 + 2} = \frac{y_0}{[(t - t_0)/t_E]^2 + y_0^2 + 2}. \tag{3.60}$$

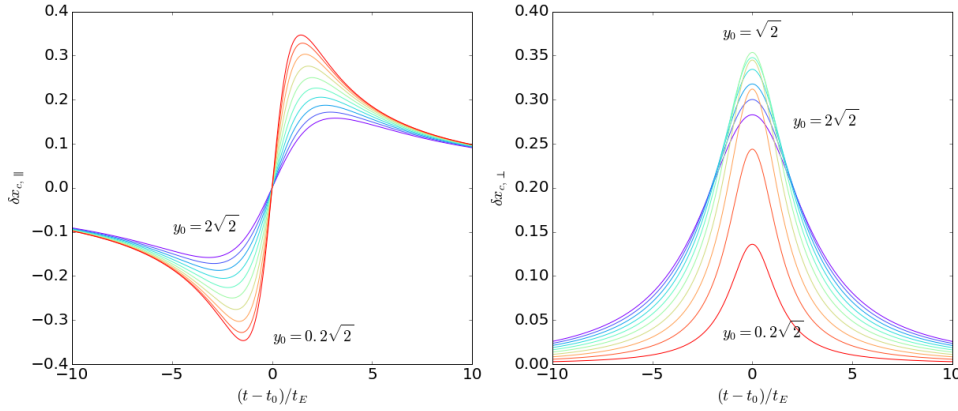


**Figure 3.4.3:** Components of the light centroid shift as a function of time. The left and the right panels show the shift components parallel and perpendicular to the trajectory of the source, respectively. Different colors are used to illustrate the results for different impact parameters  $y_0$ .

These two functions of time are shown in Fig. 3.4.3

We can see that  $\delta x_{c,||}$  is anti-symmetric around  $t_0$ , i.e. it is negative for  $t < t_0$  and positive otherwise. By taking the time derivative, we see that

$$\frac{d(\delta x_{c,||})}{dt} = \frac{y_0^2 + 2 - [(t - t_0)/t_E]^2}{\{[(t - t_0)/t_E]^2 + y_0^2 + 2\}^2}. \quad (3.61)$$

Thus, the function has a maximum and a minimum at  $(t_m - t_0)/t_E = \pm\sqrt{y_0^2 + 2}$ , where

$$\delta x_{c,||,min}, \delta x_{c,||,max} = \pm \frac{1}{2\sqrt{y_0^2 + 2}}. \quad (3.62)$$

For  $y_0 \ll 1$ , the minimum and the maximum occur at  $(t_m - t_0)/t_E \approx \pm\sqrt{2}$  and  $\delta x_{c,||,min/max} \approx \pm\delta x_{c,max}$ .

On the other hand,  $\delta x_{c,\perp}$  has a maximum at  $(t - t_0)/t_E = 0$ , i.e. at  $t = t_0$ , where it reaches the value

$$\delta x_{c,\perp,max} = \frac{y_0}{y_0^2 + 2}. \quad (3.63)$$

Since  $\delta x_{c,||}(t = t_0) = 0$ , the shift is only perpendicular to the motion of the source at this time. For  $y_0 = \sqrt{2}$ ,  $\delta x_{c,\perp,max}$  reaches its maximum amplitude  $\delta x_{c,max}$ .

If Fig. 3.4.4, we show how the total amplitude light centroid shift varies as a function of time for a variety of values of  $y_0$ . We can see that

$$\frac{d(\delta x_c)}{dp} = 2p \frac{2 - y_0^2 - p^2}{2\sqrt{y_0^2 + p^2(y_0^2 + p^2 + 2)^2}}, \quad (3.64)$$

where we have introduced  $p = (t - t_0)/t_E$ . For  $y_0 < \sqrt{2}$ ,  $\delta x_c(t)$  has two maxima at  $p_{max} = (t_{max} - t_0)/t_E = \pm\sqrt{2 - y_0^2}$  and one minimum at  $p_{min} = 0$ , i.e. at  $t = t_0$ . On the contrary, for  $y_0 > \sqrt{2}$ , only one maximum exist at  $t = t_0$ . These results can interpreted as follows. For sources with small impact parameter, the centroid shift is mainly parallel to the motion of the source, thus

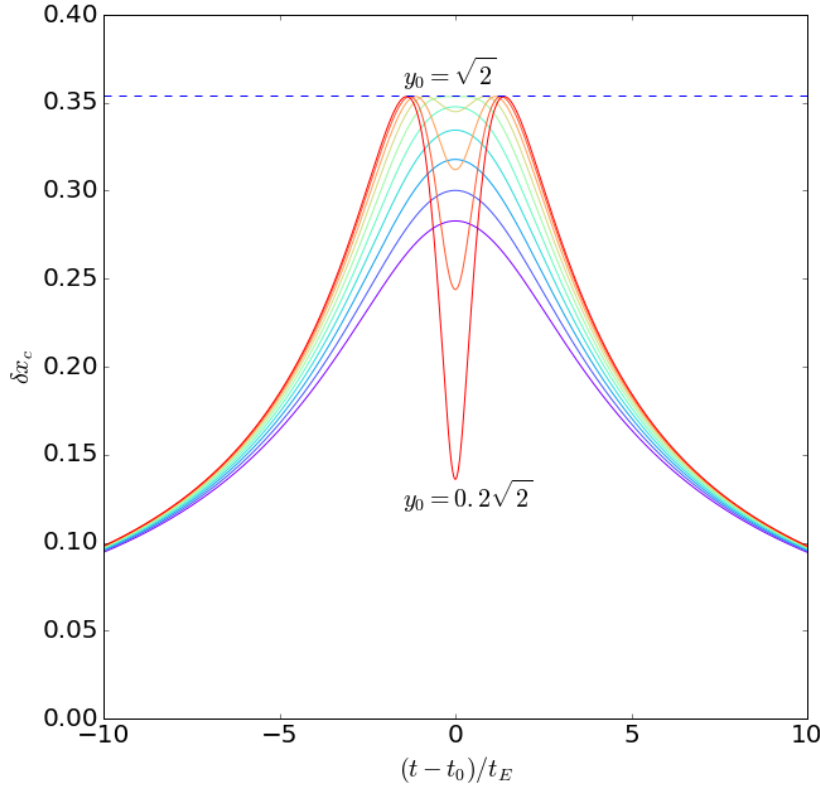


**Figure 3.4.4:** Total amplitude of the light centroid shift as a function of time. Different colors are used to illustrate the results for different impact parameters  $y_0$ .

two maxima exist, which correspond to the minimum and to maximum of  $\delta x_{c,\parallel}$  shown in Fig. 3.4.3. On the contrary, for sources with large impact parameter, the dominant component of the shift is the one perpendicular to the direction of motion of the source, which has a single peak at  $t = t_0$ .

When combined, these motions along the  $\delta_{\parallel}$  and  $\delta_{\perp}$  directions generate the elliptical paths shown in the right panel of Fig. 3.4.2. The ellipses are centered in  $(0, y_0)$ . Their major-axes and the semi-minor axes are oriented along the  $\delta_{\parallel}$  and  $\delta_{\perp}$  directions, respectively. As it results from Eqs. 3.62 and 3.63, their sizes are

$$a = \frac{1}{2} \frac{1}{\sqrt{y_0^2 + 2}} \quad (3.65)$$

$$b = \frac{1}{2} \frac{y_0}{y_0^2 + 2}. \quad (3.66)$$

For  $y_0 \rightarrow \infty$ , the ellipse degenerates to a circle with radius  $r \approx 1/2y_0$  (thus, with size tending to zero). For  $y_0 \rightarrow 0$ , the ellipse degenerates to straight line, as  $b \rightarrow 0$  and  $a \rightarrow 1/2$ .

### 3.5 Multiple point masses

#### 3.5.1 Generalities

##### Deflection angle

The deflection angle of an ensemble of  $N$  point masses was given in Eq. 1.46. Even for such lens, the proper choice of an angular scale allows to write the deflection angle in a convenient form. Generalizing the case of a single point mass, we can define an equivalent Einstein radius for a mass equal to the sum of the point masses,  $M_{tot} = \sum_{i=1}^N M_i$ . The reduced deflection angle can be written as

$$\vec{\alpha}(\vec{\theta}) = \sum_{i=1}^N \frac{D_{LS}}{D_L D_S} \frac{4GM_i}{c^2} \frac{(\vec{\theta} - \vec{\theta}_i)}{|\vec{\theta} - \vec{\theta}_i|^2} \frac{M_{tot}}{M_{tot}} = \sum_{i=1}^N m_i \frac{\theta_E^2}{|\vec{\theta} - \vec{\theta}_i|^2} (\vec{\theta} - \vec{\theta}_i), \quad (3.67)$$

where we have set  $m_i = M_i/M_{tot}$ . By further dividing by  $\theta_E$ , we obtain:

$$\vec{\alpha}(\vec{x}) = \sum_{i=1}^N \frac{m_i}{|\vec{x} - \vec{x}_i|^2} (\vec{x} - \vec{x}_i), \quad (3.68)$$

where  $x = \theta/\theta_E$ .

##### Lens equation

The lens equation in the adimensional form then reads

$$\vec{y} = \vec{x} - \sum_{i=1}^N \frac{m_i}{|\vec{x} - \vec{x}_i|^2} (\vec{x} - \vec{x}_i). \quad (3.69)$$

**1990A&A...236..311W** showed that it is convenient to use the complex notation instead of the vectorial form to write this lens equation. Using this notation,  $z = x_1 + ix_2$  and  $z_s = y_1 + iy_2$  are the positions on the lens and on the source planes. The complex deflection angle is  $\alpha(z) = \alpha_1(z) + i\alpha_2(z)$  which can then be written as

$$\alpha(z) = \sum_{i=1}^N m_i \frac{(z - z_i)}{(z - z_i)(z^* - z_i^*)} = \sum_{i=1}^N \frac{m_i}{z^* - z_i^*}, \quad (3.70)$$

where the  $*$  symbol denotes the complex conjugate. The lens equation is

$$z_s = z - \sum_{i=1}^N \frac{m_i}{z^* - z_i^*}. \quad (3.71)$$

By taking the complex conjugate of both sides, we can then solve for  $z^*$ :

$$z^* = z_s^* + \sum_{i=1}^N \frac{m_i}{z - z_i}. \quad (3.72)$$

This can be inserted into Eq. 3.71 to obtain a complex polynomial equation of degree  $N^2 + 1$ . Thus, the lens equation formally have up to  $N^2 + 1$  solutions, some of which may, however, be spurious. **2001astro.ph..3463R; 2003astro.ph..5166R** probed that, in fact, a lens composed of  $N > 3$  point masses produces a maximum of  $5(N - 1)$  images.

### Critical lines

To find the critical lines, we first need to compute the determinant of the lensing Jacobian. In Sect. 2.3, this was found to be

$$\det A = \frac{\partial y_1}{\partial x_1} \frac{\partial y_2}{\partial x_2} - \left( \frac{\partial y_1}{\partial x_2} \right)^2. \quad (3.73)$$

Using the complex differential operators, we see that

$$\frac{\partial z_s}{\partial z} = \frac{1}{2} \left( \frac{\partial}{\partial x_1} - i \frac{\partial}{\partial x_2} \right) (y_1 + iy_2) = \frac{1}{2} \left( \frac{\partial y_1}{\partial x_1} + \frac{\partial y_2}{\partial x_2} \right) + \frac{i}{2} \left( \frac{\partial y_2}{\partial x_1} - \frac{\partial y_1}{\partial x_2} \right) \quad (3.74)$$

$$\frac{\partial z_s}{\partial z^*} = \frac{1}{2} \left( \frac{\partial}{\partial x_1} + i \frac{\partial}{\partial x_2} \right) (y_1 + iy_2) = \frac{1}{2} \left( \frac{\partial y_1}{\partial x_1} - \frac{\partial y_2}{\partial x_2} \right) + \frac{i}{2} \left( \frac{\partial y_2}{\partial x_1} + \frac{\partial y_1}{\partial x_2} \right). \quad (3.75)$$

The imaginary part of Eq. 3.74 is zero, because  $\partial y_1 / \partial x_2 = \partial y_2 / \partial x_1$ . Thus,

$$\left( \frac{\partial z_s}{\partial z} \right)^2 = \frac{1}{4} \left[ \left( \frac{\partial y_1}{\partial x_1} \right)^2 + \left( \frac{\partial y_1}{\partial x_2} \right)^2 + 2 \frac{\partial y_1}{\partial x_1} \frac{\partial y_2}{\partial x_2} \right] \quad (3.76)$$

and

$$\left( \frac{\partial z_s}{\partial z^*} \right) \left( \frac{\partial z_s}{\partial z^*} \right)^* = \frac{1}{4} \left[ \left( \frac{\partial y_1}{\partial x_1} \right)^2 + \left( \frac{\partial y_1}{\partial x_2} \right)^2 - 2 \frac{\partial y_1}{\partial x_1} \frac{\partial y_2}{\partial x_2} \right] + \left( \frac{\partial y_1}{\partial x_2} \right)^2. \quad (3.77)$$

By taking the difference of Eqs. 3.76 and 3.77, we obtain that

$$\left( \frac{\partial z_s}{\partial z} \right)^2 - \left( \frac{\partial z_s}{\partial z^*} \right) \left( \frac{\partial z_s}{\partial z^*} \right)^* = \frac{\partial y_1}{\partial x_1} \frac{\partial y_2}{\partial x_2} - \left( \frac{\partial y_1}{\partial x_2} \right)^2 = \det A \quad (3.78)$$

Using the lens equation in the form given in Eq. 3.71, we finally see that

$$\frac{\partial z_s}{\partial z} = 1 \quad (3.79)$$

and

$$\frac{\partial z_s}{\partial z^*} = \sum_{i=1}^N \frac{m_i}{(z^* - z_i^*)^2}. \quad (3.80)$$

Thus,

$$\det A = 1 - \left| \sum_{i=1}^N \frac{m_i}{(z^* - z_i^*)^2} \right|^2. \quad (3.81)$$

It follows that the critical lines are defined by

$$\left| \sum_{i=1}^N \frac{m_i}{(z^* - z_i^*)^2} \right|^2 = 1. \quad (3.82)$$

The sum in the above equation must be satisfied on the unit circle. The complex solutions of this equation can be found by solving

$$\sum_{i=1}^N \frac{m_i}{(z^* - z_i^*)^2} = e^{i\phi} \quad (3.83)$$

for each  $\phi \in [0, 2\pi)$ . The above equation is a complex polynomial of order  $2N$  with respect to  $z$ . Thus, for each value of  $\phi$ , there are  $2N$  or less critical points. By varying  $\phi$  continuously, the solutions will trace out  $2N$  (or less) critical lines. Critical lines corresponding to different solutions may join smoothly (**1990A&A...236.311W**). Note that for  $N = 1$ ,  $m_1 = 1$  and, by taking  $z_1 = 0$ , we obtain that the critical line is the Einstein ring ( $|z| = 1$ ). In the case of multiple point masses, however, the critical lines are much more complicated, as we will see in the next Section.

As usual the critical lines can be mapped onto the source plane through the lens equation. This will give the caustics.

### 3.5.2 Binary lenses

#### Lens equation

The binary lens is a particular case of multiple point mass lenses, where  $N = 2$ . In this case, the lens equation is

$$z_s = z - \frac{m_1}{z^* - z_1^*} - \frac{m_2}{z^* - z_2^*}. \quad (3.84)$$

Since the choice of the reference frame is arbitrary, we may opt for selecting the real axis to pass through the two lenses. We may further set  $z_2 = -z_1$ .

As discussed in the previous Section, the lens equation for the binary lens can be reduced to a complex polynomial equation of degree 5:

$$c_0 + c_1 z + c_2 z^2 + c_3 z^3 + c_4 z^4 + c_5 z^5 = 0, \quad (3.85)$$

where

$$\begin{aligned} c_0 &= z_1^2 [4(\Delta m)^2 z_s + 4m\Delta m z_1 + 4\Delta m z_s z_s^* z_1 + 2mz_s^* z_1^2 + z_s z_s^{*2} z_1^2 - 2\Delta m z_1^3 - z_s z_1^4] \\ c_1 &= -8m\Delta m z_s z_1 - 4(\Delta m)^2 z_1^2 - 4m^2 z_1^2 - 4mz_s z_s^* z_1^2 - 4\Delta m z_s^* z_1^3 - z_s^{*2} z_1^4 + z_1^6 \\ c_2 &= 4m^2 z_s + 4m\Delta m z_1 - 4\Delta m z_s z_s^* z_1 - 2z_s z_s^{*2} z_1^2 + 4\Delta m z_1^3 + 2z_s z_1^4 \\ c_3 &= 4mz_s z_s^* + 4\Delta m z_s^* z_1 + 2z_s^{*2} z_1^2 - 2z_1^4 \\ c_4 &= -2mz_s^* + z_s z_s^{*2} - 2\Delta m z_1 - z_s z_1^2 \\ c_5 &= z_1^2 - z_s^{*2}. \end{aligned} \quad (3.86)$$

In the above equations we have introduced  $\Delta m = (m_1 - m_2)/2$  and  $m = (m_1 + m_2)/2$  (**1995ApJ...447L.105W**).

#### Critical lines and caustics

It can be shown that Eq. 3.85 has 3 or 5 images depending on the distance between the two point masses and on their mass ratio. This can be better understood by looking at the structure of the critical lines and caustics. The critical lines can be found as explained above by solving the Eq. 3.83. In the case of the binary lens, this assumes the form

$$\frac{m_1}{(z^* - z_1^*)^2} + \frac{m_2}{(z^* - z_2^*)^2} = \frac{m_1}{(z^* - z_1^*)^2} + \frac{m_2}{(z^* + z_1^*)^2} = e^{i\phi} \quad (3.87)$$

for  $\phi \in [0, 2\pi)$ . by getting rid of the fractions, the equation can be turned into

$$z^4 - z^2(2z_1^{*2} + e^{i\phi}) - zz_1^{*2}(m_1 - m_2)e^{i\phi} + z_1^{*2}(z_1^{*2} - e^{i\phi}) = 0. \quad (3.88)$$

The left side is a fourth degree polynomial. Thus, for each  $\phi$  there are up to four solutions of this equation.

In the python application in Sect. 3.7.4 we show how to find the solutions of the above equation and to draw the critical lines of the binary lens. The critical points are mapped onto the caustics via

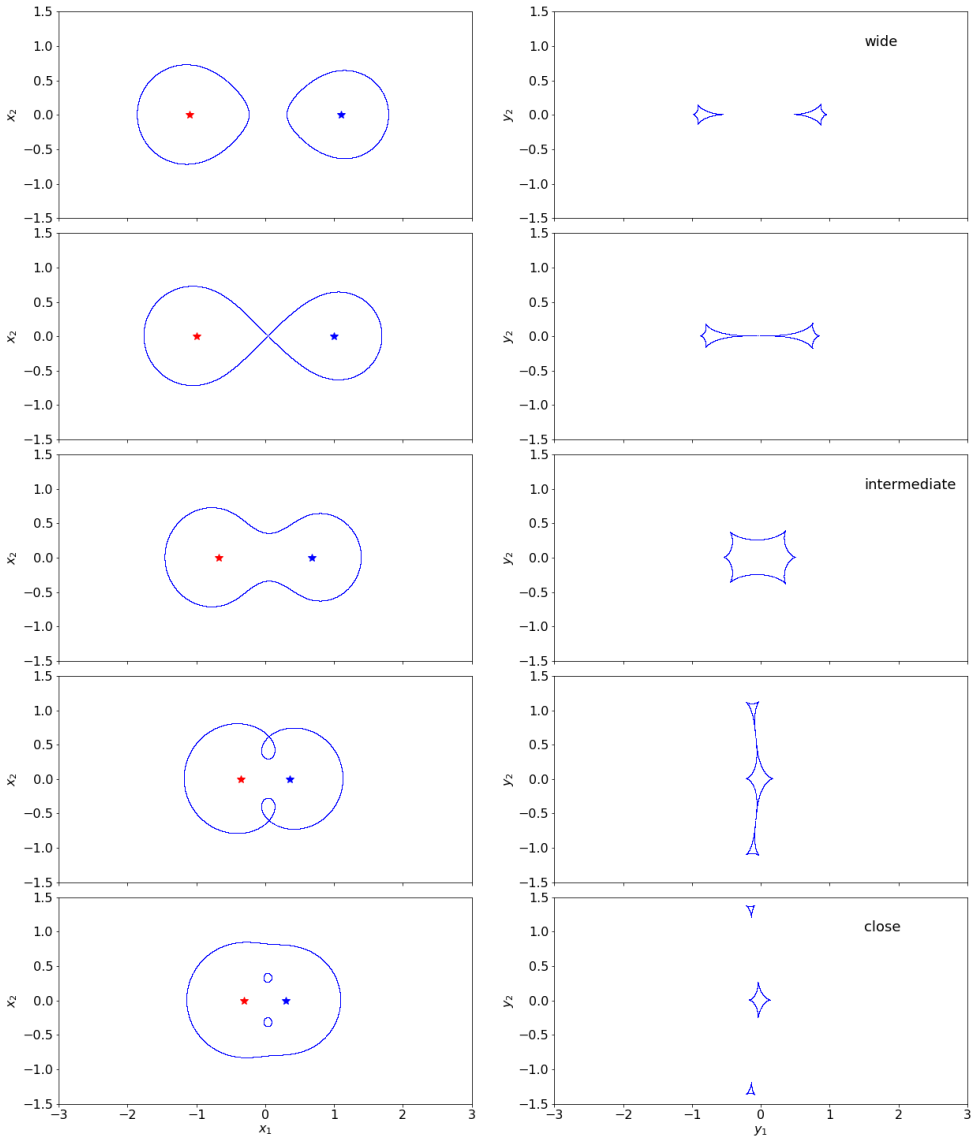


**Figure 3.5.1:** Critical lines (left panels) and caustics (right panels) of a binary lens system for different values of the separation between the point masses,  $d$ . From the top to the bottom, we show examples of wide, intermediate, and close topologies. The results refer to the case of a lens with  $M_1 = 1M_\odot$  and  $q = 0.8$ .

the lens equation. Depending on the ratio of the two masses,  $q = m_1/m_2$ , and on the separation between the two lenses in units of the equivalent Einstein radius,  $d = |z_1 - z_2|$ , the resulting caustics can be one, two, or three.

We distinguish between wide, intermediate, and close systems on the basis of the topology of

the caustics, as shown in Fig. 3.5.1. More precisely:

- in wide systems, there exist two separate extended caustics, which correspond to the point-like caustics associated with the individual lenses. The shape of the caustics resemble that of an astroid with four cusps. This is the result of the reciprocal perturbation of each lens on the other. Indeed, the presence of two masses breaks the symmetry of the point-mass lens. The wide topologies are typical of binary systems with large separations between the two lenses;
- in intermediate systems, there exist a single caustic, characterized by six cusps. This caustic is the result of the merging of the two individual astroid-like caustics in wide systems, which happens when the lenses are brought closer to each other (or when the masses of the individual lenses are increased, thus making the equivalent Einstein radius bigger, and reducing  $d$ );
- finally, in close systems, there are three caustics. Two are triangular-like and one is an astroid-like caustic with four cusps.

The transitions between these topologies occur when two critical lines merge at one point (**2002glml.book.....M**). This happens where, not only  $\det A = 0$ , but also  $\partial \det A / \partial z^* = 0$  (the gradient of the Jacobian determinant is zero). In particular, it can be shown that the transition between wide and intermediate regimes occurs for a separation between the lenses (in units of the equivalent Einstein radius) of

$$d_{WI} = (m_1^{1/3} + m_2^{1/3})^{3/2}. \quad (3.89)$$

On the other hand, the transition between intermediate and close regimes occurs when

$$d_{IC} = (m_1^{1/3} + m_2^{1/3})^{-3/4}. \quad (3.90)$$

### Multiple images

Solving Eq. 3.85 leads to finding the multiple images of a source at  $z_s$ . This must be done numerically, as illustrated in Sect. 3.7.5. Here, we give some brief and qualitative statements about the occurrence of multiple images.

- a source outside the caustics has only three images, meaning that two solution of the lens equation are spurious. Two of these images form inside the critical lines and, for large distances of the source from the binary lens, their positions are very close to the two point masses. This is very similar to the behavior of the image with negative parity in the case of the point-mass lens (see Eq. 3.11). The image outside the critical lines correspond to a local minimum of the time-delay surface, and have positive parity;
- when the source is on the caustic, two additional images appear on the critical line (thus they are formally indistinguishable and have infinite magnification);
- when the source is inside the caustics, five images exist.

 Note that, due to the singularity of lensing potential of the two point-masses, there are always at least three images of a single source.

The above statements can be verified by looking at Fig. 3.5.2. In the left panel, we show the critical lines of a binary lens. The case chosen have  $q = 1$  and  $d = 1$ . The corresponding caustics are shown in the right panel, where we also display the trajectory of a source in relative motion in the background of the binary lens. A color sequence is used to identify the source position as a function of time. The images, which are also color-coded, are shown in the left panel.

The source trajectory crosses the lens caustics at two points. Let us call the corresponding crossing times  $t_1$  (light blue) and  $t_2$  (green). Before  $t_1$  and after  $t_2$ , there are three images of the background source. Between  $t_1$  and  $t_2$ , the images are five. In particular, two images appear at the

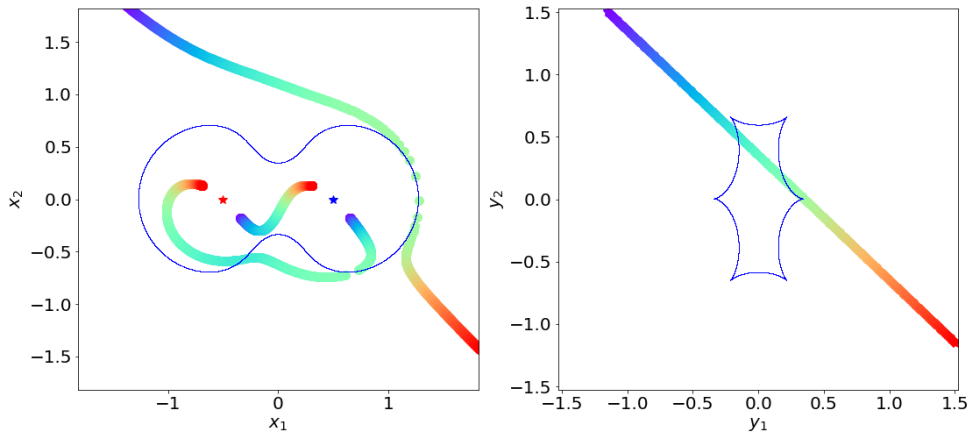


**Figure 3.5.2:** Images of a source in relative motion with respect to a foreground binary lens. In the right panel, the caustics of the lens and the trajectory of the source are shown. We color-code the source position as a function of time. The corresponding images are shown in the left panel, together with the lens critical line. The binary lens is made of two stars of equal mass at a distance  $d = 1$ , thus the caustic is resonant.

time  $t_1$  on the lens critical line. While the source moves across the caustic, one of the images moves outside the critical line, while the other follows a trajectory which brings it near the star of mass  $m_1$ . The outer image approaches the critical line again at  $t_2$ , when it merges with one of the inner images. The two images disappear once the source has crossed the caustic again.

### Image magnifications and light-curves

As in the case of microlensing by single lenses, the multiple images are not spatially resolved. Thus, the microlensing events involving binary lenses are also revealed through variations of the source luminosity. The shape of the source light curves, however, have much more complex shapes compared to the case of the single point-mass lens<sup>1</sup>.

The shape of the light curve reflects how the sum of the magnifications of the images changes as a function of time:

$$\mu(t) = \sum_{j=1}^{N_{ima}} |\mu_j(t)| . \quad (3.91)$$

The magnification of image  $j$  is obtained by inserting the image position  $z_j(t)$  in Eq. 3.81:

$$\mu_j(t) = \left[ 1 - \left| \sum_{i=1}^N \frac{m_i}{z_j^*(t) - z_i^*} \right|^2 \right]^{-1} . \quad (3.92)$$

In Sect. 3.7.6 we discuss how to compute the light-curve of a source in the background of a binary lens. We show in Fig. 3.5.3 the light-curve corresponding to the example in Fig. 3.5.2. The signatures of the passage of a source across the fold of the caustic are very sharp spikes in the light-curve. The shape of the spikes is asymmetric: if the source enters the caustic, there is a sudden rise of the observed flux, followed by a slightly more gentle decline of light curve. **1995ApJ...447L.105W** showed analytically that, while the source is inside the caustic, the total

<sup>1</sup>Even in the case of binary lenses, microlensing events produce astrometric signatures.

magnification cannot be smaller than 3. A similar asymmetry (although reversed) is observed when the source exits the caustic. These events are called *caustic crossing* events.

Finite source-size effects affect the sharpness of these transitions in the light-curves. Indeed, if the size of the source is not negligible the light-curve appears smoothed, while the event lasts longer (as the result of the fact that the source takes more time to cross the fold of the caustic).

The passage of the source near a cusp, which is a locus of very high magnification, produces another steep rise of the light curve. In these *cusp* events, there is a single peak in the light curve, as shown in Fig. 3.5.3.

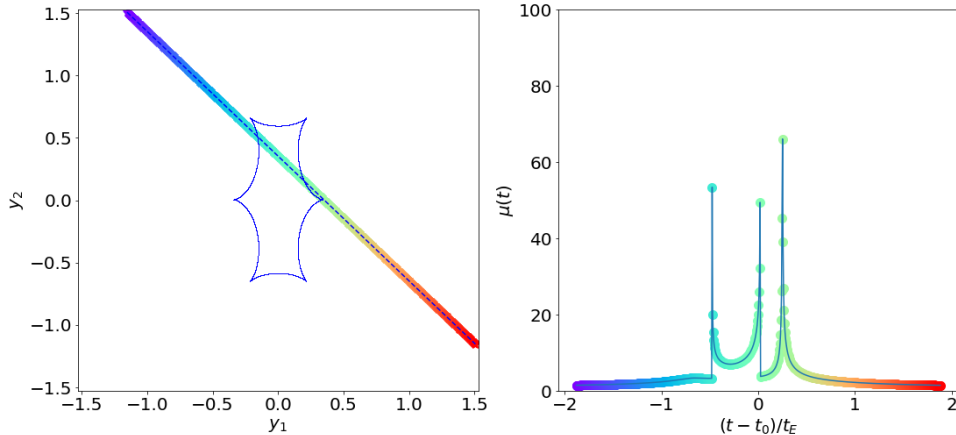


**Figure 3.5.3:** Light-curve of the source whose multiple images are shown in Fig. 3.5.2.

### 3.6 Planetary microlensing

A system made of a planet orbiting a star is a particular kind of binary lens, where the mass budget is dominated by the star. For Jupiter-like planet orbiting a solar mass star  $q \sim 10^{-3}$ . Conversely, for an Earth-like planet  $q \sim 3 \times 10^{-6}$ . Given the small mass ratio, the light-curve is most of the time very similar to the standard microlensing light-curve by a single star. The presence of a secondary lens (the planet) produces localized perturbations to the magnification pattern, which can be revealed through short-time variations of the standard light-curve. The features produced by the planet have shapes which strongly depend on the trajectory of the source with respect to the lens.

#### Perturbations of the central caustic

As discussed earlier, the shape of the caustic matters. Also in the case of planetary microlensing, three types of caustic (and critical line) topologies are possible: wide, intermediate (or resonant), and close. In Fig. 3.6.1 we show how the caustics and an the critical lines of a binary lens change when we keep  $d$  fixed and vary the mass ratio  $q$ . The three examples shown refer to the three topologies. In the case of a wide system (left column), the caustic of the primary (i.e. most massive) component becomes smaller and smaller as  $q$  decreases. In addition, the angular distance between the lens and this caustic becomes smaller. This is not surprising: as long as the two masses are well separated, putting most of the mass into one of the two lenses makes the overall system very similar to a single point-mass lens. Similarly, bringing the star and the planet close to each other, the central caustic shrinks (close topology).

Because of the small value of  $q$ , the central caustics are very elongated in the direction of the planet. Indeed, they are characterized by a pronounced cusp. Three additional cusps are located on the back of the caustic with respect to the planet.

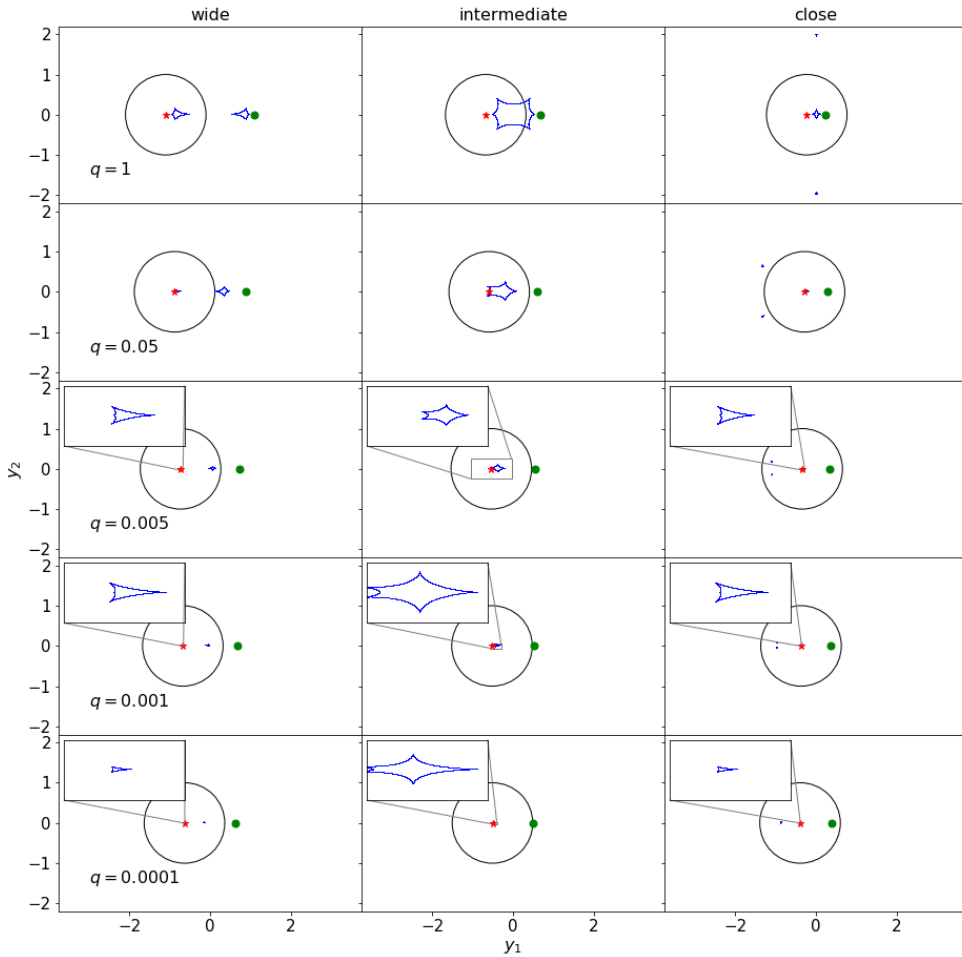


**Figure 3.6.1:** Caustics of a binary lens for different values of the mass ratio  $q$ . The left, central, and right panels refer to wide, intermediate, and close topologies, respectively. In each panel the two mass components are indicated with a red star and with a circle. In the cases with  $q \ll 1$ , the green circle represents a planet-like mass. The equivalent Einstein radius is given by the black circle in each panel. The insets show zooms over the central caustics.

In Fig. 3.6.2, we show some examples of central caustic perturbations in the light-curve of a source. The source trajectory, relative to the lens, is given by the dotted line in each of the left panels. The central panels zoom over the central caustic. The source trajectory is indicated here by a color-sequence, which allows to read-off where the source is located at the time when a perturbation of the light-curve is detected in the right panels. From the upper to the lower panels, the source trajectory is such to pass behind, across, or in front of the central caustic (with the respect to the position of the planet, which is given by the blue dot in the left panels). The standard light curve, i.e. the light curve which could be measured in absence of the planet is given by the dashed black lines in the right panels.

When the source passes behind the central caustic (upper panels), we first see a negative perturbation (with respect to the standard light-curve), followed by positive perturbation of the

light-curve. In the case where the source crosses the caustic (middle panels), we see two peaks in the light curve, which occur at the times when the source enters and exits the central caustic. Finally, in the case when the source passes in front of the pronounced cusp, which is a location where the magnification is particularly strong, we see a single, sharp peak in the light curve (bottom panels).

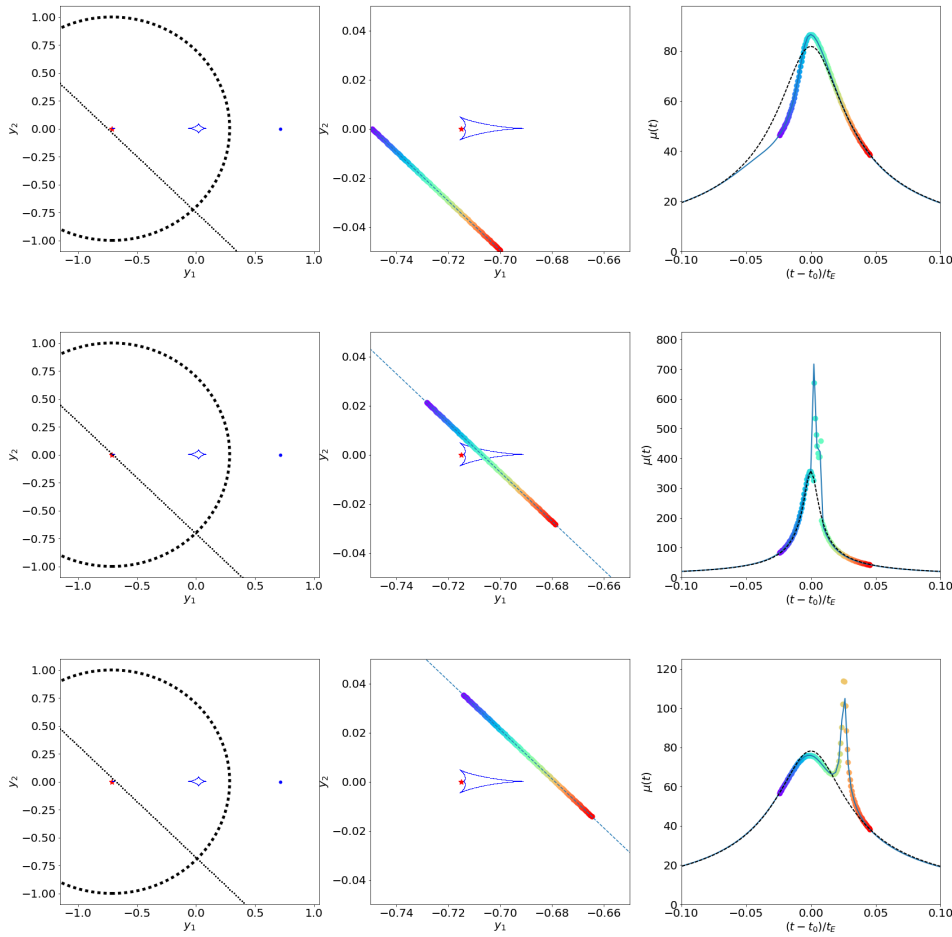


**Figure 3.6.2:** Central caustic perturbations by planets.

It is worth noticing that all these perturbations are near the peak of the light-curve, i.e. they occur in an high-magnification regime. This is particularly relevant in terms of event detectability. In some sense, events like these are predictable, because the primary microlensing event can be revealed earlier than the planet perturbation appears. If the search strategy consists of detecting the primary event and triggering a follow-up (as in the first generation of microlensing surveys), the cadence at which the light-curve is monitored can be adjusted such to make the detection of such planet perturbations possible. In addition, since they occur in high-magnification regimes, photometric measurements in such events tend to be more accurate (**2012ARA&A..50..411G**).

The insets in Fig. 3.6.1 show that, for  $q \ll 1$ , there is a degeneracy between close and wide topologies in terms of the shape of the central caustic. In fact, close and wide systems where  $d_c = d_w^{-1}$  (as in the examples shown in the left and in the right panels) have identical central caustics. Thus, the planet signatures in the light-curve in central caustic events do not allow to distinguish between wide and close topologies (wide-close degeneracy).

### Perturbations of the planetary caustic

Another way to detect the presence of a planet around a star is by means of signatures of the planetary caustic.

In wide topologies, the planetary caustic is an astroid-like caustic with four cusps. **2006ApJ...638.1080H** showed that the size of this caustic scales as  $\sim q^{1/2}d^{-2}$  and that its distance from the star is  $\sim d - d^{-1}$ . Signatures of this caustic in the light-curve are single- or double-peaks occurring when the source passes close a cusp or across the caustic. Some example of these perturbations are shown in the upper panels of Fig. 3.6.3. These events can be detected at lower magnifications compared to central caustic events, because of the distance of the planetary caustic from the star. The perturbation can be detected near the peak of the primary light curve, if the source trajectory is nearly perpendicular to the axis of the binary lens. However the impact parameter  $y_0$  is larger than in the case of central caustic events.

In close topologies, there are two planetary caustics, which are located on the opposite side of the star with respect to the planet (see the bottom panels in Fig. 3.6.3). The positions of the two caustics is symmetric with respect to the axis passing through the star and the planet. **2006ApJ...638.1080H** showed that the size of the triangular caustics scales as  $\sim q^{1/2}d^3$ . The separation between the two caustics is  $\sim 2q^{1/2}(d^{-2} - 1)^{1/2}$ , and their distance from the star is  $\sim d^{-1} - d$ . The signatures of these caustics in the source-light curve can be single or double peaks corresponding to the cases where the source passes near the cusps or crosses the caustic. In addition, the region in between the two triangular caustics is characterized by a relatively low magnification. Thus, a depression in the light-curve, with respect to the primary microlensing event, can be seen if the source trajectory passes near these planetary caustics and crosses the axis of the binary lens.

Planetary caustic events occur in low- to medium-magnification regimes.

### Perturbations of the resonant caustic

For  $q \ll 1$ , intermediate (or resonant) caustics are possible only for a narrow range of separations. This can be shown as follows. Let us consider the transition between wide and intermediate topologies, which occurs for  $d_{WI} = (m_1^{1/3} + m_2^{1/3})^{3/2}$ . Some simple algebra shows that

$$d_{WI} = (1 + q^{1/3})^{3/2} m_1^{1/2}. \quad (3.93)$$

We recall that  $d$  is the angular separation between the two masses in units of the equivalent Einstein radius,  $\theta_E$ , which is in turn related to the Einstein radius of the primary by

$$\theta'_E = m_1^{1/2} \theta_E. \quad (3.94)$$

Thus, the separation between the star and the planet at the transition between wide and intermediate topologies, in units of the Einstein radius of the star, is

$$d'_{WI} = d_{WI}/m_1^{1/2} = (1 + q^{1/3})^{3/2} \sim 1 + 3/2q^{1/3}. \quad (3.95)$$

Similarly, since  $d_{IC} = (m_1^{1/3} + m_2^{1/3})^{-3/4}$ , we obtain that

$$d'_{IC} = d_{IC}/m_1^{-1/4} = (1 + q^{1/3})^{-3/4} \sim 1 - 3/4q^{1/3}. \quad (3.96)$$

Therefore, the range of distances between the star and the planet for which the caustic is resonant is

$$d'_{WI} - d'_{IC} \sim \frac{9}{4}q^{1/3},. \quad (3.97)$$

Obviously, this range is very narrow for small values of  $q$ .

Some examples of light-curve perturbations by a resonant caustic are shown in Fig. ???. The passage of the source in front, across, or behind the caustic correspond to either positive or negative deviations from the standard light curve. These perturbations are located near the peak of the standard light curve, and, because the caustic is close to the star, these events occur in intermediate- to high-magnification regimes.

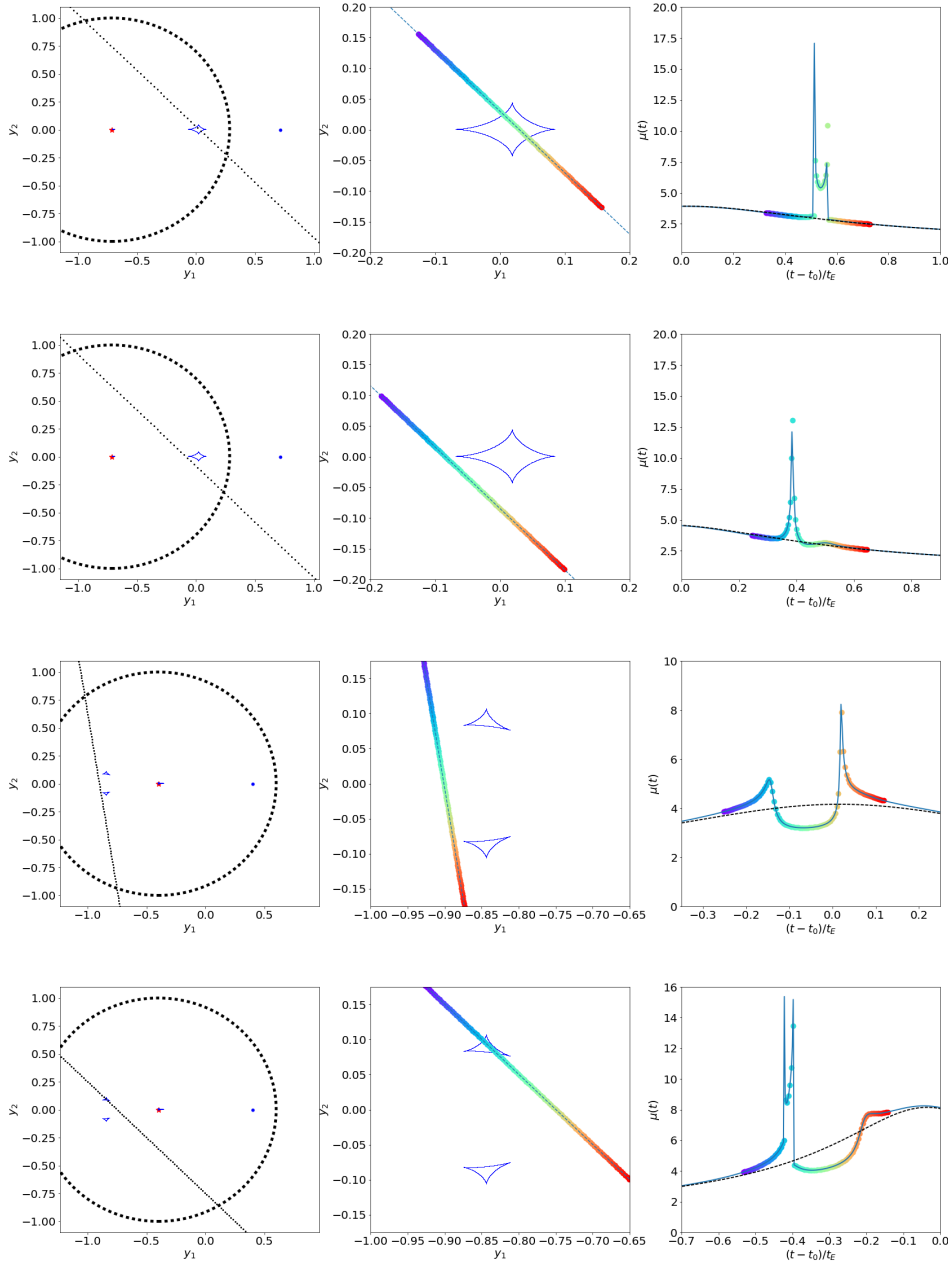


**Figure 3.6.3:** Planetary caustic perturbations of the light-curves.

### Astrometric effects

As discussed above, during a planetary microlensing event, we detect an anomaly in the standard light-curve of the microlensing event by the star. While we have shown that the planet locally perturbs the magnification pattern of the single lens, we can explain the anomalies also in terms of astrometric perturbations. This can be very instructive to fully understand the phenomenon and to realize to which kind of planets microlensing is sensitive.

In the microlensing event by the star, two images form, one inside and one outside the Einstein ring. In the left panels of Fig. ??, we show the positions of the images corresponding to a given source trajectory with respect to the lens.

As seen earlier, in order to detect the planetary perturbation, the source trajectory must pass

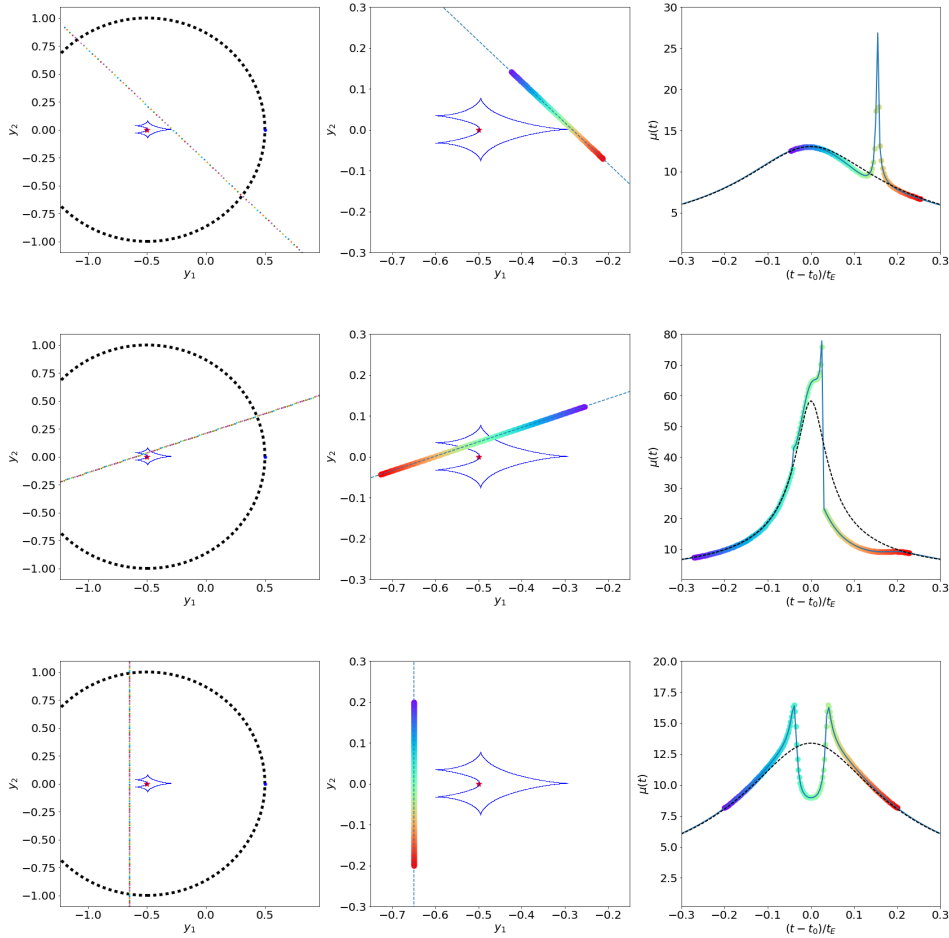


**Figure 3.6.4:** Resonant caustic perturbations of the light-curves.

close to either the central, the planetary, or the resonant caustic. The central and the resonant caustics are located near the star. Consequently, the images of the source must be near the Einstein radius. Thus, in order to perturb the images, the planet must be near the Einstein radius too.

In the case of a planetary caustic

### Planetary microlensing surveys

The search for planets using microlensing is a relatively young field of research. The first detections are dated back...

## 3.7 Python applications

### 3.7.1 Standard microlensing light curve

In the following example, we derive the standard light curve in a microlensing event involving a point lens and a point source. The source moves with a constant transverse velocity  $v$  or relative motion

$$\mu_{rel} = \frac{v}{D_L} .$$

Assuming that the trajectory of the source relative to the lens is linear, during the microlensing event, the magnification of the source changes as

$$\mu(t) = \frac{y^2(t) + 2}{y(t)\sqrt{y^2(t) + 4}}$$

with

$$y(t) = \sqrt{y_0^2 + \left(\frac{t-t_0}{t_E}\right)^2}.$$

For more explanations about these formulas, we refer the reader to Sects. 3.1 and 3.2.

First, we import some useful packages. In particular, we will make use here of some constants defined in the module `constants` of `astropy` and we will need to make proper unit conversions us-

ing the module units of `astropy`.

```
# import useful packages

import numpy as np
import matplotlib.pyplot as plt
from astropy import constants as const
from astropy import units as u
import matplotlib.ticker as ticker
```

We begin implementing the relevant functions, namely:

- the Einstein radius  $\theta_E$ ;
  - the Einstein crossing time  $t_E$ ;
  - the relative distance between the source and the lens as a function of time,  $y(t)$ ;
  - the magnification as a function of time,  $\mu(t)$ .

```

# the Einstein radius
def theta_e_func(M,DL,DS):
    mass=M*const.M_sun#.value
    G=const.G#.value
    c=const.c#.value
    aconv=180.0*3600.0/np.pi*u.arcsecond
    return((np.sqrt(4.0*(G*mass/c*c).to('kpc'))*(DS-DL)/DL/DS/u.kpc))*aconv)

# the Einstein radius crossing time
def EinsteinCrossTime(M,DL,DS,v):
    theta_e=theta_e_func(M,DL,DS)
    return(((theta_e.to('radian').value*DL*u.kpc).to('km')
           /v/u.km*u.s).to('day')).value

# the distance of the source from the lens as a function of time
def yt(tE,y0,t0,t):
    return (np.sqrt(y0**2+((t-t0)/tE)**2))

# the lens magnification as a function of time
def mut_func(tE,y0,t0,t):
    y=yt(tE,y0,t0,t)
    return ((y**2+2)/y/np.sqrt(y**2+4))

```

The lens system consists of a lens with mass  $M = 0.3M_{\odot}$  at  $D_L = 4$  kpc and a source at  $D_S = 8$  kpc. We assume that the relative velocity of the source with respect to the lens is  $v = 200$  km/s. The

following code sets these initial values up:

```
M_lens=0.3 # solar masses
DL=4.0 # kpc
DS=8.0 # kpc
vel=200 # km/s
```

We will display the light curves for a variety of impact parameters  $y_0$ . The choice of the time of the passage of the source at the minimum distance from the lens happens is not important, as we will

display the light-curves as a function of  $(t - t_0)/t_E$ :

```
# initialize the impact parameters
y0=np.linspace(1.0,0.1,10)
# passage at the minimum distance from the lens
t_0=365 # days
# compute the Einstein radius crossing time
t_einst=EinsteinCrossTime(M_lens,DL,DS,vel) # days
t=t_0+np.linspace(-2,2,200)*t_einst
```

Finally, we can create the plot. We will loop on the values of the impact parameters and for each of them we will compute the light-curve  $\mu(t)$ . We will use a sequence of colors from the rainbow

```

xx=[-2,2]

fig,ax=plt.subplots(1,2,figsize=(18,8))
ax[1].set_ylim([1.0,10.0])
ax[1].set_xlim([-2,2])
ax[1].set_yscale('log')
ax[1].set_xlabel(r'$\frac{t-t_0}{t_E}$',fontsize=23)
ax[1].set_ylabel(r'$\mu(t)$',fontsize=23)
ax[1].set_yticks(np.arange(1, 11, 1.0))
ax[1].yaxis.set_major_formatter(ticker.FormatStrFormatter('%.1f'))
ax[1].xaxis.set_tick_params(labelsize=20)
ax[1].yaxis.set_tick_params(labelsize=20)

# create a circle with radius 1 (the Einstein ring)
circle=plt.Circle((0,0),1,color='black',fill=False)
ax[0].set_xlim([-1.5,1.5])
ax[0].set_ylim([-1.5,1.5])
ax[0].add_artist(circle) # display the Einstein ring
ax[0].plot([0.0],[0.0],'*',markersize=20,color='red')
ax[0].xaxis.set_tick_params(labelsize=20)
ax[0].yaxis.set_tick_params(labelsize=20)

from matplotlib.pyplot import cm
# create a color sequence using the rainbow color-map
color=iter(cm.rainbow(np.linspace(0,1,y0.size)))

# loop over the impact parameters and plot the light
for i in range(y0.size):
    c=next(color)
    mut=mut_func(t_einst,y0[i],t0,t)
    ax[1].plot((t-t0)/t_einst,mut,'-',color=c)
    yy=[y0[i],y0[i]]
    ax[0].plot(xx,yy,'--',color=c,lw=2)

ax[0].set_xlabel(r'$y_1$',fontsize=23)
ax[0].set_ylabel(r'$y_2$',fontsize=23)

```

resulting plot is shown in Fig. 3.2.2.

### 3.7.2 Fitting the standard light curve

The microlensing light-curve is a function of  $t_0$ ,  $y_0$ , and  $t_E$ . This last parameter is in turn a function of  $M$ ,  $v$ ,  $D_L$ , and  $D_S$ . The normalization of the light-curve is given by the base-line flux  $f_0$ , which can be regarded as an additional parameter. Once a microlensing event has been detected and the light-curve has been measured, we wonder how well the parameters listed above can be derived.

Here, we set up the following experiment:

- we simulate the observation of a microlensing event and generate synthetic data, including measurement errors;
- we use the package `lmfit` to find the maximum-likelihood model fitting the data;
- we perform a bayesian analysis based on the package `emcee` to estimate the posterior probability distributions of the parameters and estimate the uncertainties.

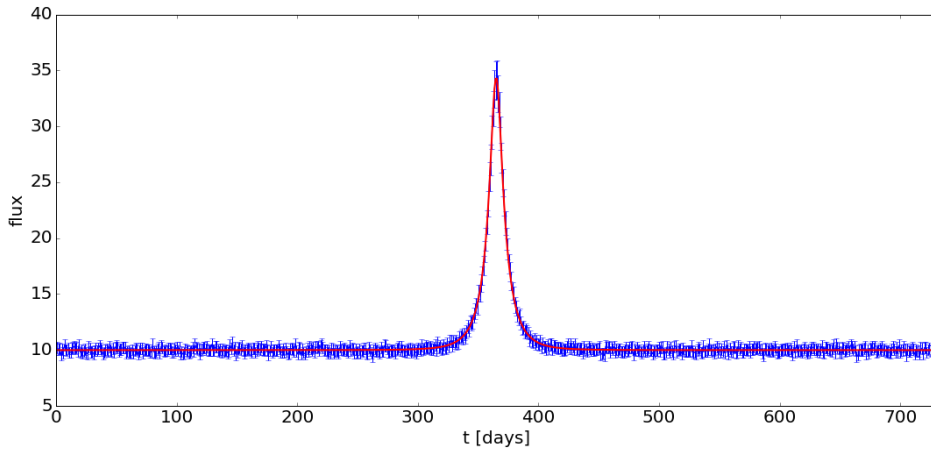


**Figure 3.7.1:** Simulated light curve of a microlensing event (blue points with error bars. The best fit to the data is shown in red.

The lens system is composed by a lens of mass  $M = 0.3M_{\odot}$  at  $D_L = 4$  kpc and by a source at  $D_S = 8$  kpc. The source baseline flux is chosen to be  $f_0 = 10$  (the units are arbitrary). The relative velocity of the source is  $v = 210$  km/s and we assume that impact parameter  $y_0$  is 0.3. We assume to monitor the source star for a long period (2 years) and to collect data continuously. This is clearly unrealistic, but we want to test a very ideal situation. In addition, we assume that the accuracy of the measurement is 5%. The passage of the source at the minimum distance from the lens occurs at  $t_0 = 365$  days after we begin monitoring the source star.

The code used to generate the synthetic data is here below. To compute the light curve, we use

```
# input parameters for the light-curve
t=np.linspace(0,730,730)
M_lens=0.3 # solar masses
DL=4.0 # kpc
DS=8.0 # kpc
vel=210 # km/s
y0=0.3
t0=365.0 # days
flux0=10.0 # some arbitrary flux unit

t_einst=EinsteinCrossTime(M_lens,DL,
# lightcurve plus random noise
mut=flux0*(mut_func(t_einst,y0,t0,t))

# we assign to the data some errors,
# constant fraction of the measurement
emut=mut*0.05
```

the functions defined in the previous example discussed in Sect. 3.7.1.

light-curve is displayed in Fig. 3.7.1 (blue points with error bars).

As said, in order to fit the data, we use the python package `lmfit`. This package allows to build complex fitting models for non-linear least-squares problems. The implementation shown here was obtained by closely following the examples in the package documentation, which can be found at this link: [http://cars9.uchicago.edu/software/python/lmfit\\_MinimizerResult/intro.html](http://cars9.uchicago.edu/software/python/lmfit_MinimizerResult/intro.html)

We begin by setting up some initial guesses for the model parameter, storing them in a `lmfit.Parameter` object, including also some plausible ranges where the parameters are free to

vary. Then, we write the function to be minimized, a.k.a. the *objective* function:

```
import lmfit

# initial guesses
p = lmfit.Parameters()
p.add_many(('t0', 360., True, 0,
            ('DL', 5., True, 0),
            ('vel', 200, True, 10),
            ('flux0', 12, True))

# objective function
def residual(p):

    v = p.valuesdict()
    t_einst=EinsteinCrossTime
    res=(mut_func(t_einst,v[

        return (res)
```

function simply compares the model to the data, returning the residuals, weighted by the measurement errors.

The next step is use a minimizer to minimize the objective function (i.e. the residuals). Several algorithms are available in `lmfit`. Here, we perform the minimization using the Nelder-Mead

```
# minimize the objective function using the Nelder-Mead method
mi = lmfit.minimize(residual, p, method='Nelder')
# print report on the fit
lmfit.printfuncs.report_fit(mi.params, min_correl=0.5)

# plot the maximum likelihood solution on the top of the data
fig,ax=plt.subplots(1,1,figsize=(18,8))
ax.errorbar(t, mut, emut)
method.
ax.set_xlabel('t [days]', fontsize=20)
ax.set_ylabel('flux', fontsize=20)
ax.xaxis.set_tick_params(labelsize=20)
ax.yaxis.set_tick_params(labelsize=20)
ax.set_xlim([0,730])

t_einst=EinsteinCrossTime(mi.params['M_lens'],mi.params['DL'],
                         mi.params['DS'],mi.params['vel'])
ax.plot(t,mi.params['flux0']*mut_func(t_einst,mi.params['y0'],
                                         mi.params['t0'],t),'r',lw=2)
```

figure generated by this piece of code is that shown in Fig. 3.7.1. The report of the maximum likeli-

hood parameters reads:

[[Variables]]	t0: 365.002446 (init= 360) M_lens: 0.22162718 (init= 0.5) DL: 5.17859669 (init= 5) DS: 9.89082660 (init= 10) vel: 200.691012 (init= 200) y0: 0.29997367 (init= 0.2) flux0: 9.98550295 (init= 12)
---------------	--

derive the probability distribution for the parameters, we use a Bayesian approach. More precisely, we perform a Bayesian sampling of the posterior distribution for the parameters using the `emcee`

The

Markov Chain Monte Carlo package. You need to have `emcee` installed to use this method.

The method requires to define a log-likelihood function, which is used to compute the log-posterior probability of the model parameters as

$$\ln P(p|d) \propto \ln P(d|p) + \ln P(p), \quad (3.98)$$

where  $p$  are the parameters and  $d$  are the data. The method (implemented in `lmfit`) assumes that the prior is uniform, i.e.  $\ln P(p) = 0$ .

The log-likelihood function is given by

$$\ln P(d|p) = -\frac{1}{2} \sum_n \left[ \frac{(model_n - data_n)^2}{s_n^2} + \ln 2\pi s_n^2 \right]. \quad (3.99)$$

```
# log-likelihood function
def lnprob(p):
    from numpy import inf
    resid = residual(p)
    s = emut
    resid *= resid
    resid += np.log(2 * np.pi * s**2)
    lnp=-0.5 * np.sum(resid)
    if (np.isnan(lnp)):
        lnp=-1e10

    return lnp
```

can not perform the sampling of the posterior distribution:

```
# build a general minimizer for curve fitting
mini = lmfit.Minimizer(lnprob, mi.params, nan_ok=True)
# sampling of the posterior distribution
res = mini.emcee(burn=300, steps=2000, thin=1)
```

will generate 2000 samples. The posterior distributions for the parameters can be displayed in a corner plot, shown in Fig. 3.7.2. This requires installation of the `corner` package:

```
# show corner plot (confidence
# correlations)
import corner
figure=corner.corner(res.flatchain,
                      truths=li,
                      show_titles=True)
```

The values reported in the `MinimizerResult` are the medians of the probability distributions and a

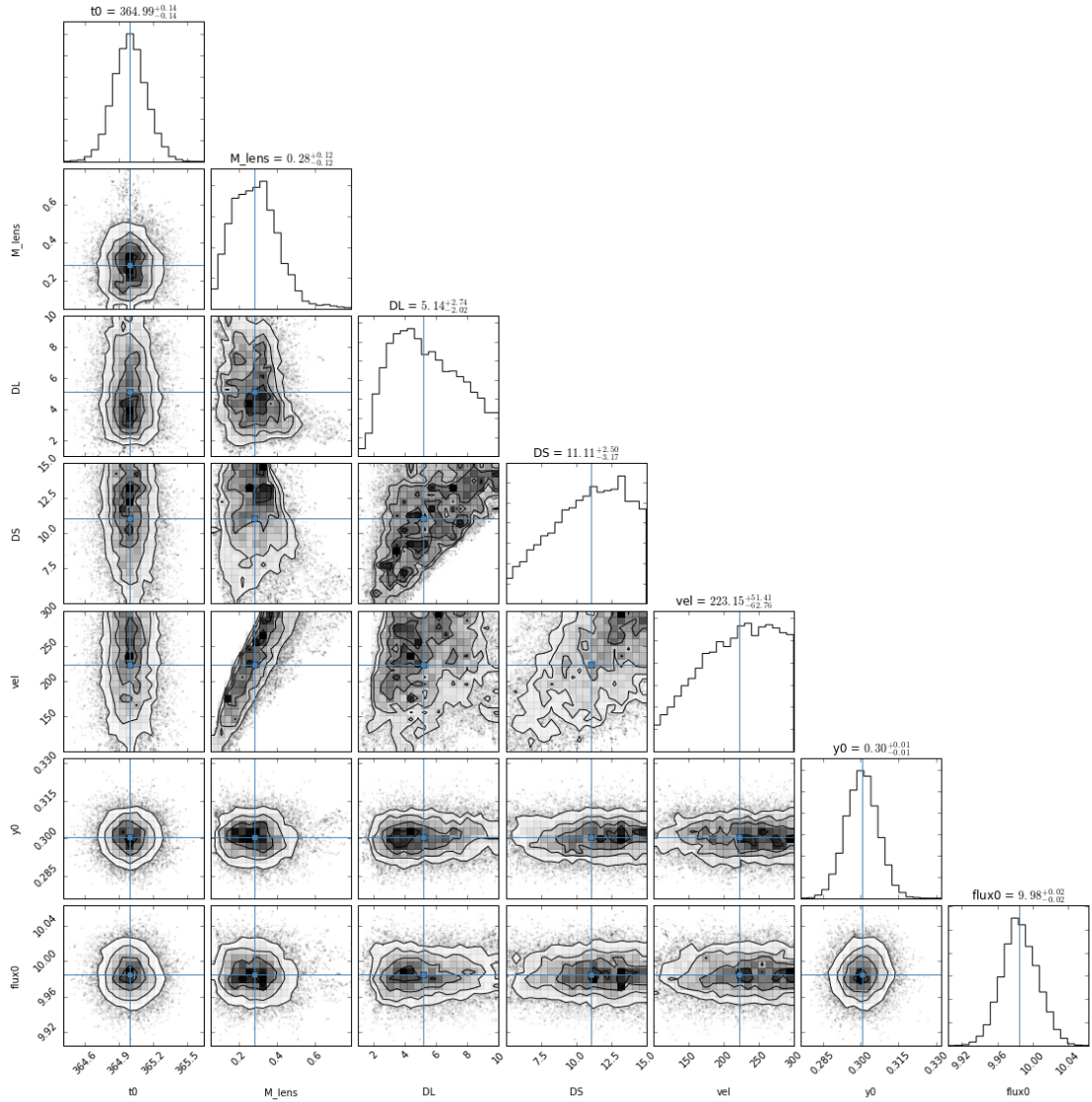


**Figure 3.7.2:** Corner plot showing the posterior distributions for the parameters.

$1\sigma$  quantile, estimated as half the difference between the 15.8 and 84.2 percentiles:

```

median of posterior probability density

[[Variables]]
t0: 365.005389 +/- 0.14
M_lens: 0.29572066 +/- 0.12
DL: 4.77833889 +/- 2.74
DS: 10.8725461 +/- 3.17
vel: 224.631948 +/- 51.41
y0: 0.29996274 +/- 0.01
flux0: 9.98410492 +/- 0.02

[[Correlations]] (unreported correlations)
C(M_lens, vel)
C(DL, DS)
C(DS, vel)
C(DL, vel)
C(M_lens, DS)
C(M_lens, DL)

```

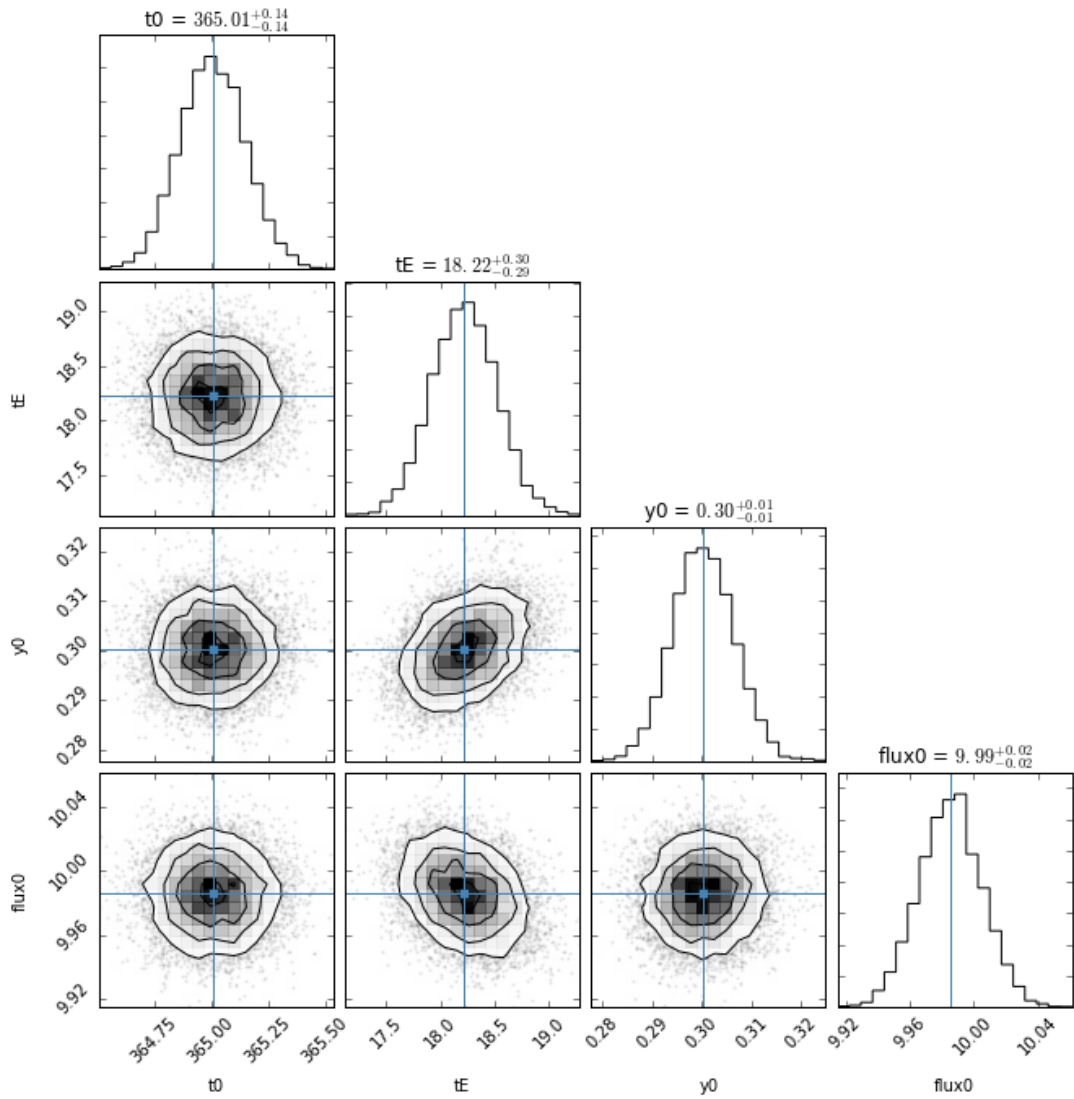


**Figure 3.7.3:** Corner plot showing the posterior distributions for the parameters.

are correlations between the parameters `vel`, `M_lens`, `DL`, and `DS`, which highlight the microlensing degeneracy: with a single microlensing event, it is only possible to constrain the parameter  $t_E$ , which is a combination of all these parameters.

Fig. 3.7.3 shows the results of the fit to the measured light-curve with a model which depends only on  $t_E$ ,  $t_0$ , and  $y_0$ .

### 3.7.3 Astrometric microlensing effect

### 3.7.4 Critical lines and caustics of a binary lens

### 3.7.5 Solving the lens equation of the binary lens

### 3.7.6 Light curve in a binary microlensing event

## 3.8 Planetary microlensing

## 4. Extended lenses

In this chapter, we review some properties of extended lenses, i.e. gravitational lenses which can be described by extended, bound, mass distributions. Cosmic structures like galaxies and galaxy cluster belong to this class of gravitational lenses.

We consider analytical lens models, i.e. models whose lensing properties are (almost) fully expressed by means of analytic formulas. We change a few properties of the lens mass distributions to understand how these impact the ability to produce gravitational lensing effects. In particular, we focus on:

- the density profile;
- the shape;
- the small scale perturbations;
- the effects of the environment.

### 4.1 Axially symmetric lenses

We begin with the simplest description of an extended lens, i.e. an axially symmetric, or circular, lens. The main advantage of using axially symmetric lenses is that their surface density is independent on the position angle with respect to lens center. If we choose the lens center as the origin of the reference frame on the lens plane, then  $\Sigma(\vec{\xi}) = \Sigma(|\vec{\xi}|)$ . Most of the equations therefore reduce to a one-dimensional form.

#### Deflection angle

In general, the deflection angle is a two-dimensional vector. In the case of axially symmetric lenses, however, we can demonstrate that this vector always points away from the lens center.

We begin with Eq. 1.48. A obvious choice for the origin of the reference frame is the center of the lens. We can choose the reference frame such that  $\vec{\xi} = (\xi, 0)$ ,  $\xi \geq 0$ . In polar coordinates,  $\vec{\xi}' = (\xi'_1, \xi'_2) = \xi'(\cos \phi, \sin \phi)$  (see Fig. 4.1.1). Then,

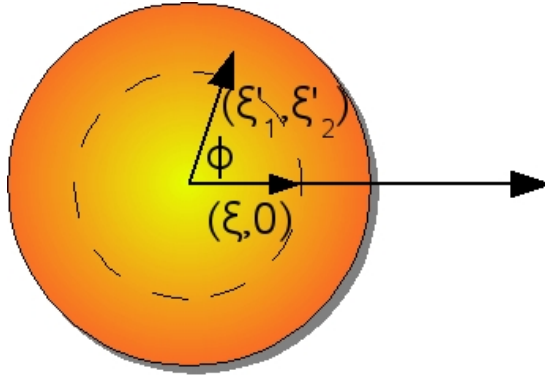


**Figure 4.1.1:** A sketch of an axially symmetric lens.

$$\vec{\xi} - \vec{\xi}' = (\xi - \xi' \cos \phi, -\xi' \sin \phi) \quad (4.1)$$

$$\begin{aligned} |\vec{\xi} - \vec{\xi}'|^2 &= \xi^2 + \xi'^2 \cos^2 \phi - 2\xi \xi' \cos \phi + \xi'^2 \sin^2 \phi \\ &= \xi^2 + \xi'^2 - 2\xi \xi' \cos \phi \end{aligned} \quad (4.2)$$

For a symmetric mass distribution  $\Sigma(\vec{\xi}) = \Sigma(|\vec{\xi}|)$ . The components of the deflection angle are thus

$$\begin{aligned} \hat{\alpha}_1(\vec{\xi}) &= \frac{4G}{c^2} \int_0^\infty d\xi' \xi' \Sigma(\xi') \int_0^{2\pi} d\phi \frac{\xi - \xi' \cos \phi}{\xi^2 + \xi'^2 - 2\xi \xi' \cos \phi} \\ \hat{\alpha}_2(\vec{\xi}) &= \frac{4G}{c^2} \int_0^\infty d\xi' \xi' \Sigma(\xi') \int_0^{2\pi} d\phi \frac{-\xi' \sin \phi}{\xi^2 + \xi'^2 - 2\xi \xi' \cos \phi} \end{aligned} \quad (4.3)$$

By symmetry, the second component of the deflection angle is zero. Thus,  $\hat{\alpha}$  is parallel to  $\vec{\xi}$ .

By considering the first component of the deflection angle in Eq. 4.3, we see that the inner integral vanishes for  $\xi' > \xi$ , while this equals  $2\pi/\xi$  for  $\xi' < \xi$ . Thus, the deflection angle for an axially symmetric lens is

$$\hat{\alpha}(\xi) = \frac{4G}{c^2} \frac{2\pi \int_0^\xi \Sigma(\xi') \xi' d\xi'}{\xi} = \frac{4GM(\xi)}{c^2 \xi} . \quad (4.4)$$

The formula is similar to that derived for a point mass. The deflection is determined by the mass enclosed by the circle of radius  $\xi$ ,  $M(\xi)$ .

As usual, we can use the adimensional notation. This implies the choice of an arbitrary linear scale,  $\xi_0$ , which corresponds to the angular scale  $\theta_0 = \xi_0/D_L$ . From Eqs. 2.6 and 2.17, the reduced deflection angle in the adimensional form is:

$$\begin{aligned} \alpha(x) &= \frac{D_L D_{LS}}{\xi_0 D_S} \hat{\alpha}(\xi_0 x) \\ &= \frac{D_L D_{LS}}{\xi_0 D_S} \frac{4GM(\xi_0 x)}{c^2 \xi} \frac{\pi \xi_0}{\pi \xi_0} \\ &= \frac{M(\xi_0 x)}{\pi \xi_0^2 \Sigma_{cr}} \frac{1}{x} \equiv \frac{m(x)}{x} , \end{aligned} \quad (4.5)$$

where we have introduced the *dimensionless mass*  $m(x)$ . Note that

$$\alpha(x) = \frac{2}{x} \int_0^x x' \kappa(x') dx' \Rightarrow m(x) = 2 \int_0^x x' \kappa(x') dx' . \quad (4.6)$$

### Lens equation

Since  $\vec{\alpha}(\vec{x})$  is parallel to  $\vec{x}$ , the lens equation (2.7) can be written omitting the vector notation. Using the result from the previous section, we obtain

$$y = x - \frac{m(x)}{x} . \quad (4.7)$$

### Convergence and shear

Convergence and shear can be obtained from the partial derivatives of the deflection angle. To compute them, we need to write the deflection angle as a vector:

$$\vec{\alpha}(\vec{x}) = \frac{m(\vec{x})}{x^2} \vec{x} , \quad (4.8)$$

where  $\vec{x} = (x_1, x_2)$ .

By differentiating, we obtain:

$$\frac{\partial \alpha_1}{\partial x_1} = \frac{dm}{dx} \frac{x_1^2}{x^3} + m \frac{x_2^2 - x_1^2}{x^4} , \quad (4.9)$$

$$\frac{\partial \alpha_2}{\partial x_2} = \frac{dm}{dx} \frac{x_2^2}{x^3} + m \frac{x_1^2 - x_2^2}{x^4} , \quad (4.10)$$

$$\frac{\partial \alpha_1}{\partial x_2} = \frac{\partial \alpha_2}{\partial x_1} = \frac{dm}{dx} \frac{x_1 x_2}{x^3} - 2m \frac{x_1 x_2}{x^4} . \quad (4.11)$$

This allows us to obtain the following expressions for the convergence and the shear components:

$$\kappa(x) = \frac{1}{2x} \frac{dm(x)}{dx} , \quad (4.12)$$

$$\gamma_1(x) = \frac{1}{2} (x_2^2 - x_1^2) \left( \frac{2m(x)}{x^4} - \frac{dm(x)}{dx} \frac{1}{x^3} \right) , \quad (4.13)$$

$$\gamma_2(x) = x_1 x_2 \left( \frac{dm(x)}{dx} \frac{1}{x^3} - \frac{2m(x)}{x^4} \right) . \quad (4.14)$$

From these relations,

$$\gamma(x) = \frac{m(x)}{x^2} - \kappa(x) . \quad (4.15)$$

Since  $m(x) = 2 \int_0^x x' \kappa(x') dx'$ , we see that

$$\frac{m(x)}{x^2} = 2\pi \frac{\int_0^x x' \kappa(x') dx'}{\pi x^2} = \bar{\kappa}(x) . \quad (4.16)$$

where  $\bar{\kappa}(x) = m(x)/x^2$  is the *mean surface mass density* within  $x$ . Eq. 4.15 then reduces to

$$\gamma(x) = \bar{\kappa}(x) - \kappa(x) \quad (4.17)$$

### Lensing Jacobian

From Eqs. 4.11, we immediately obtain the Jacobian matrix:

$$\begin{aligned} A &= I - \frac{m(x)}{x^4} \begin{pmatrix} x_2^2 - x_1^2 & -2x_1 x_2 \\ -2x_1 x_2 & x_1^2 - x_2^2 \end{pmatrix} \\ &\quad - \frac{dm(x)}{dx} \frac{1}{x^3} \begin{pmatrix} x_1^2 & x_1 x_2 \\ x_1 x_2 & x_2^2 \end{pmatrix} . \end{aligned} \quad (4.18)$$

The Jacobian determinant of the lens mapping is

$$\begin{aligned}\det A &= \frac{y}{x} \frac{dy}{dx} = \left(1 - \frac{m(x)}{x^2}\right) \left[1 - \frac{d}{dx} \left(\frac{m(x)}{x}\right)\right] \\ &= \left(1 - \frac{m(x)}{x^2}\right) \left(1 + \frac{m(x)}{x^2} - 2\kappa(x)\right) \\ &= \left(1 - \frac{\alpha(x)}{x}\right) \left(1 - \frac{d\alpha(x)}{dx}\right).\end{aligned}\quad (4.19)$$

### Critical lines and caustics:

Since the critical lines arise where  $\det A = 0$ , Eq. (4.19) implies that axially symmetric lenses with monotonically increasing  $m(x)$  have at most two critical lines, where  $m(x)/x^2 = 1$  and  $d(m(x)/x)/dx = dy/dx = 1$ . Both these conditions define circles on the lens plane (see Fig. ??). The critical line along which  $m(x)/x^2 = 1$  is the tangential one: any vector which is tangential to this line is an eigenvector with zero eigenvalue of the Jacobian matrix. On the other hand, given that any vector perpendicular to the critical line where  $d(m(x)/x)/dx = 1$  is also an eigenvector with zero eigenvalue, this line is the radial critical line. This can be seen as follows. Consider a point  $(x, 0)$  on a critical line. Although this point has been chosen to lay on the  $x_1$ -axis, this discussion can be generalized to any other critical point, since the reference frame can be arbitrarily chosen. The Jacobian at  $(x, 0)$  is readily derived from Eq. 4.18:

$$A(x, 0) = I - \frac{m(x)}{x^2} \begin{pmatrix} -1 & 0 \\ 0 & 1 \end{pmatrix} - \frac{dm(x)}{dx} \frac{1}{x} \begin{pmatrix} 1 & 0 \\ 0 & 0 \end{pmatrix}. \quad (4.20)$$

Let consider a vector whose components are  $(0, a)$  at  $(x, 0)$ . This vector is clearly tangential to the critical line at  $(x, 0)$ . Through the lens mapping, it is mapped onto

$$\begin{pmatrix} y_1 \\ y_2 \end{pmatrix} = A(x, 0) \begin{pmatrix} 0 \\ a \end{pmatrix} \quad (4.21)$$

Clearly the last term in Eq. 4.20 returns the null vector when applied to  $(0, a)$ . If  $(x, 0)$  lays on the tangential critical line, then  $(1 - m(x)/x^2) = 0$  and

$$\begin{pmatrix} y_1 \\ y_2 \end{pmatrix} = \left(1 - \frac{m}{x^2}\right) \begin{pmatrix} 0 \\ a \end{pmatrix} = \begin{pmatrix} 0 \\ 0 \end{pmatrix}. \quad (4.22)$$

Thus  $(0, a)$  is an eigenvector of  $A$  with 0 eigenvalue.

Consider now a vector  $(b, 0)$ , normal to the critical line at  $(x, 0)$ . Mapping it to the source plane we obtain:

$$\begin{pmatrix} y_1 \\ y_2 \end{pmatrix} = A(x, 0) \begin{pmatrix} b \\ 0 \end{pmatrix} = \left(1 + \frac{m(x)}{x^2} - \frac{1}{x} \frac{dm(x)}{dx}\right) \begin{pmatrix} b \\ 0 \end{pmatrix}. \quad (4.23)$$

If  $(x, 0)$  lays on the radial critical line, then  $[1 + m(x)/x^2 - m'(x)/x] = 0$ , thus  $(b, 0)$  is an eigenvector of  $A$  is 0 eigenvalue.

From the lens equation it can be easily seen that all the points along the tangential critical line are mapped on the point  $y = 0$  on the source plane. Indeed:

$$y = x \left(1 - \frac{m}{x^2}\right) = 0. \quad (4.24)$$

if  $x$  indicates a tangential critical point. Therefore, axially symmetric models have point tangential caustics. On the other hand, the points along the radial critical line are mapped onto a circular caustic on the source plane.

**Image distortions near the critical lines:**

Let us consider now how the images are distorted near the critical lines. Consider a point  $(x_c, 0)$  very close to the tangential critical line. At this point,

$$\frac{m(x)}{x^2} = 1 - \delta , \quad (4.25)$$

where  $\delta \ll 1$ .

Using Eq. 4.20, we see that near the tangential critical line the Jacobian is approximated by

$$A(x_c, 0) \simeq \begin{pmatrix} 2 - m'/x_c & 0 \\ 0 & \delta \end{pmatrix} . \quad (4.26)$$

In the first element of the matrix we have neglected  $\delta$ , being it small. Consider an ellipse around  $\vec{x}_c = (x_c, 0)$ ,

$$\vec{c}(\phi) = \vec{x}_c + \begin{pmatrix} \rho_1 \cos \phi \\ \rho_2 \sin \phi \end{pmatrix} . \quad (4.27)$$

Through the lens mapping, the source of this ellipse is

$$\vec{d}(\phi) = \vec{y}_c + \begin{pmatrix} \rho_1(2 - m'/x_c) \cos \phi \\ \rho_2 \delta \sin \phi \end{pmatrix} . \quad (4.28)$$

Suppose that  $\vec{d}(\phi)$  is a circle, i.e.  $\rho_1(2 - m'/x_c) = \rho_2 \delta$ . Then,

$$\frac{\rho_2}{\rho_1} = \frac{2 - m'/x_c}{\delta} \gg 1 . \quad (4.29)$$

Thus, the ellipse is strongly elongated along the  $x_2$  direction.

On the contrary, suppose that  $(x_c, 0)$  is very close to the radial critical line. In this case,

$$\frac{m'}{x_c} - \frac{m}{x_c^2} = 1 - \delta , \quad (4.30)$$

with  $\delta \ll 1$ . The Jacobian matrix at  $(x_c, 0)$  is then

$$A(x_c, 0) \simeq \begin{pmatrix} \delta & 0 \\ 0 & 1 - m/x_c^2 \end{pmatrix} . \quad (4.31)$$

The source corresponding to the ellipse in Eq. 4.27 is

$$\vec{d}(\phi) = \vec{y}_c + \begin{pmatrix} \rho_1 \delta \cos \phi \\ \rho_2(1 - m/x_c^2) \sin \phi \end{pmatrix} . \quad (4.32)$$

Thus, if  $\vec{d}(\phi)$  is a circle,

$$\frac{\rho_1}{\rho_2} = \frac{1 - m/x_c^2}{\delta} \gg 1 , \quad (4.33)$$

and the ellipse is now strongly elongated along the  $x_1$  direction.

Summarizing, any image near the tangential critical curve is strongly distorted tangentially to the curve itself. On the contrary, any image near the radial critical curve is radially distorted.

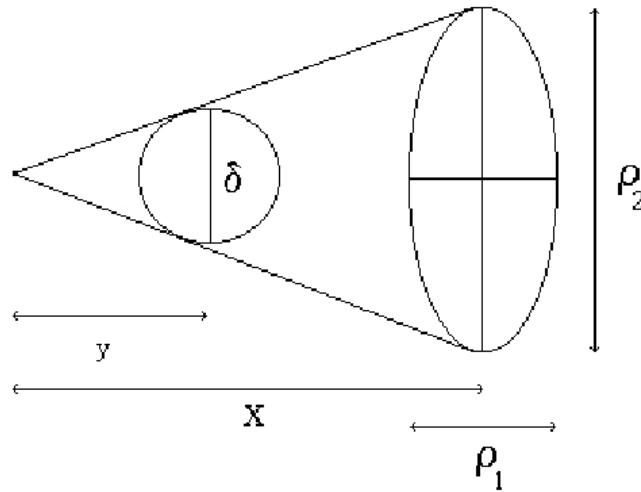


**Figure 4.1.2:** Sketch of the mapping of an infinitesimal circular source onto an elliptical image (Figure from Schneider et al., 1992).

#### Tangential and radial magnification of the images:

As was pointed out in the previous chapter, the eigenvalues of the Jacobian matrix give the inverse magnification of the image along the tangential and radial directions. Fig. (4.1.2) illustrates an infinitesimal source of diameter  $\delta$  at position  $y$  and its image, which is an ellipse, whose minor and major axes are  $\rho_1$  and  $\rho_2$  respectively, at position  $x$ . With respect to the origin of the reference frame on the source plane, the circular source subtends an angle  $\phi = \delta/y$ . Due to the axial symmetry of the lens,  $\phi = \rho_2/x$ . Using the lens equation, we thus obtain

$$\frac{\delta}{\rho_2} = 1 - \frac{m(x)}{x^2}. \quad (4.34)$$

The lens mapping gives  $\delta = \rho_1(dy/dx)$ , from which

$$\frac{\delta}{\rho_1} = 1 + \frac{m(x)}{x^2} - 2\kappa(x) \quad (4.35)$$

This means that the image is stretched in the tangential direction by a factor  $[1 - m(x)/x^2]^{-1}$  and in the radial direction by  $[1 + m(x)/x^2 - 2\kappa(x)]^{-1}$ .

## 4.2 Power-law lens

An extended lens is characterized by its surface density profile. As a first example, we consider the profile

$$\kappa(x) = \frac{3-n}{2}x^{1-n}. \quad (4.36)$$

### 4.2.1 Lenses with $1 < n < 2$

We consider lenses with  $1 < n < 2$  for the moment, which ensures that  $\kappa(x)$  is a decreasing function of  $x$ . The case  $n = 1$  corresponds to a lens with constant convergence.

**R** The normalization of this profile has been chosen such that

$$\begin{aligned} m(1) &= 2 \int_0^1 \kappa(x') x' dx' \\ &= (3-n) \int_0^1 x'^{2-n} \\ &= 1. \end{aligned} \tag{4.37}$$

This implies that the Einstein radius in dimensionless units is  $x = 1$ .

The mass profile is

$$m(x) = x^{3-n}. \tag{4.38}$$

Note that the mass cannot be negative, thus we can substitute  $x$  with its absolute value if  $x < 0$ .

The deflection angle is

$$\alpha(x) = \frac{m(x)}{x} = x^{2-n}. \tag{4.39}$$

Thus, this class of lenses have deflection angle profiles which monotonically increase with  $x$  and that are zero at the origin,  $\alpha(0) = 0$ .

### Critical lines and caustics

As for any axially symmetric lens, the tangential critical line of the power-law lens is a circle with radius  $x_t = 1$ . This is the Einstein ring, whose radius can be derived in angular units as follows.

On the tangential critical line, we have that  $m(x) = x^2$ . Thus,

$$M(\theta_E) = \pi \Sigma_{\text{cr}} \theta_E^2 D_L^2. \tag{4.40}$$

Substituting Eq. 2.17 into Eq. 4.40 and solving for  $\theta_E$ , we obtain

$$\theta_E = \sqrt{\frac{4GM(\theta_E)}{c^2} \frac{D_{\text{LS}}}{D_L D_S}}. \tag{4.41}$$

This equation is identical to Eq. 3.7, with the exception that the total mass  $M$  is now substituted by the mass within the Einstein radius,  $M(\theta_E)$ .

As seen earlier, inserting  $x_t$  into the lens equation leads to find that the tangential caustic is a point at  $y = 0$ .

Instead, the relative size of the radial critical line, with respect to the Einstein radius, depends on the index  $n$ , which in turn defines the logarithmic slope of the convergence profile,  $1 - n$ . By using Eqs. 4.39 and 4.45, we find that

$$1 - (2 - n)x_r^{1-n} = 1, \tag{4.42}$$

which can be solved to obtain

$$x_r = (2 - n)^{1/(n-1)}. \tag{4.43}$$

In Fig. 4.2.1, we show how the size of the radial critical line (in units of the Einstein radius) varies as a function of  $n$ . The figure shows that the radial critical line becomes smaller as  $n$  increases. In particular, the size is zero for  $n \rightarrow 2$ . Thus, lenses with steep profiles have small radial critical lines.

In the same Figure, we show also the size of the radial caustic. Contrary to the size of the radial critical line, the size of the radial caustic grows as a function of  $n$ . In particular, for  $n \rightarrow 2$ ,  $y_r \rightarrow 1$ .

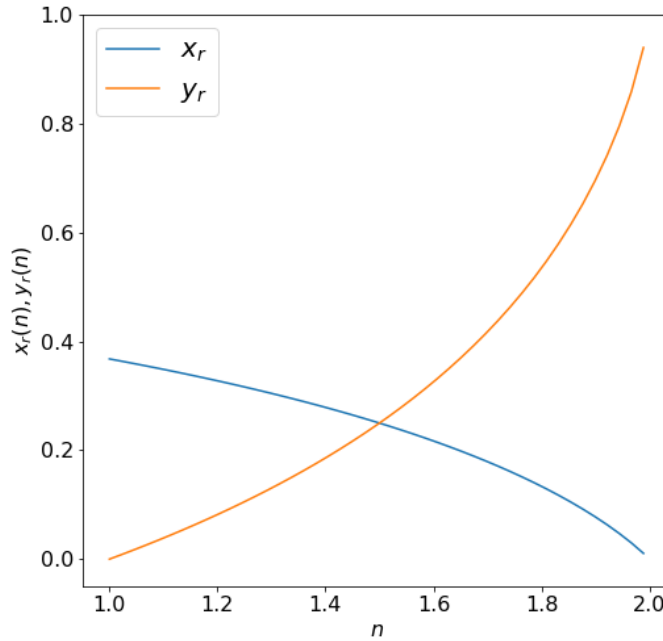


**Figure 4.2.1:** Size of the radial critical line and caustic (in units of the Einstein radius) as a function of the power-law index  $n$ .

### Multiple images

We may wonder how many images the power-law lens can produce. This can be readily discovered by inspecting the so called *image diagram*, shown in Fig. 4.2.2. The solid lines in the three panels show the curves  $\alpha(x)$  corresponding to  $n = 1.1, 1.5$  and  $1.9$ . The lens equation states that the images of a source at position  $y$  are at the interceptions of  $\alpha(x)$  and the lines  $f(x) = x - y$ . Some of these functions, corresponding to values of  $y$  increasing from  $0$  to  $1.2$ , are given by the colored dashed lines. The interceptions between the lines and  $\alpha(x)$  are marked with colored dots.

Clearly, the power-law lens can produce either three or one image of the background source, depending on whether  $y$  is smaller or larger than a particular value  $y_r$ . In fact, there exist a value of  $y = y_r$  such that the line  $f(x) = x - y_r$  is tangent to  $\alpha(x)$ . At the tangency point two images of the source merge, and for  $y > y_r$ , they no longer exist. Obviously,  $y_r$  is the radius of a caustic, and the solution of the equation

$$\alpha(x_r) = x_r - y_r \quad (4.44)$$

gives the radius of a critical line. Indeed, the tangency condition is

$$\left. \frac{d\alpha(x)}{dx} \right|_{x_r} = 1 , \quad (4.45)$$

which defines the *radial* critical line.

Thus, multiple images exist only if the source is inside the radial caustic,  $0 < y < y_r$ . One image form on the positive  $x$  axis, with  $x > y$ . Moreover, such image is outside the Einstein ring,  $x > 1$ . Two additional images, which have negative  $x$ , are inside the Einstein ring. Of these two

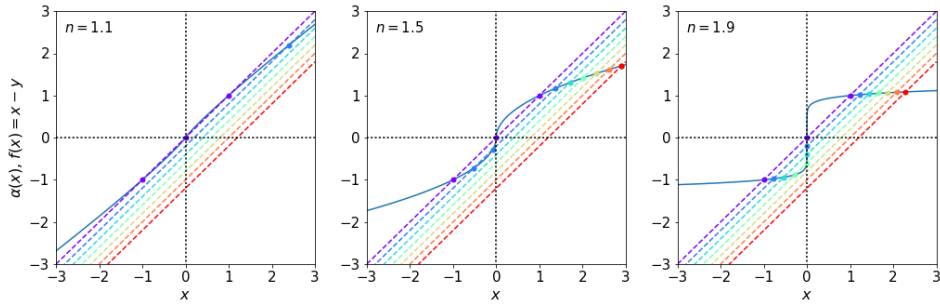


**Figure 4.2.2:** Image diagram for power-law lenses with  $n = 1.1$  (left panel),  $n = 1.5$  (central panel), and  $n = 1.9$  (right panel). The solid curves show the function  $\alpha(x)$ . The colored dashed lines show the function  $f(x) = x - y$  for a range of values of  $y \in [0, 1.2]$ .

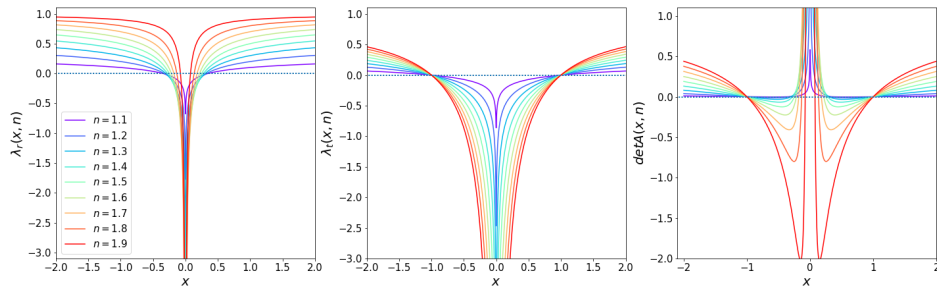


**Figure 4.2.3:** Left and central panels: Radial and tangential eigenvalues of the Jacobian matrix as a function of  $x$  for different values of  $n$ . Right panel: determinant of the lensing Jacobian, resulting from the product of the curves in the first two panels.

images, the inner one is inside the radial critical line,  $|x| < x_r$ . The other is between the radial and the tangential critical line.

**R** For  $y = 0$ , the innermost image form at  $x = 0$ . Thus, a source right behind a power-law lens with  $1 < n < 2$  is mapped onto an Einstein ring and a central image.

### Image magnification

The eigenvalues of the Jacobian matrix are readily derived

$$\lambda_t(x) = 1 - x^{1-n} \quad (4.46)$$

$$\lambda_r(x) = 1 - (2-n)x^{1-n}. \quad (4.47)$$

In the left and central panels of Fig. 4.2.6, these eigenvalues are shown as a function of  $x$ . The sign of each eigenvalue changes from outside to inside the critical lines. Thus, the overall parity of the images changes accordingly. In particular, the outermost image always have positive parity. Both eigenvalues are positive, meaning that this image correspond to a minimum of the time delay surface. The image forming in between the radial and the tangential critical lines has negative parity ( $\mu < 0$ ). Indeed, the eigenvalues of  $A$  have opposite signs, thus the image correspond to a saddle point of the time delay surface. The innermost image has again positive parity and the two eigenvalues are both negative. This image corresponds to the maximum of the time delay surface.

The right panel of Fig. 4.2.6 shows how the determinant of  $A$  varies as a function of  $x$ . For  $|\det A| < 1$ , the total magnification is larger than one. This is the case for the image outside the

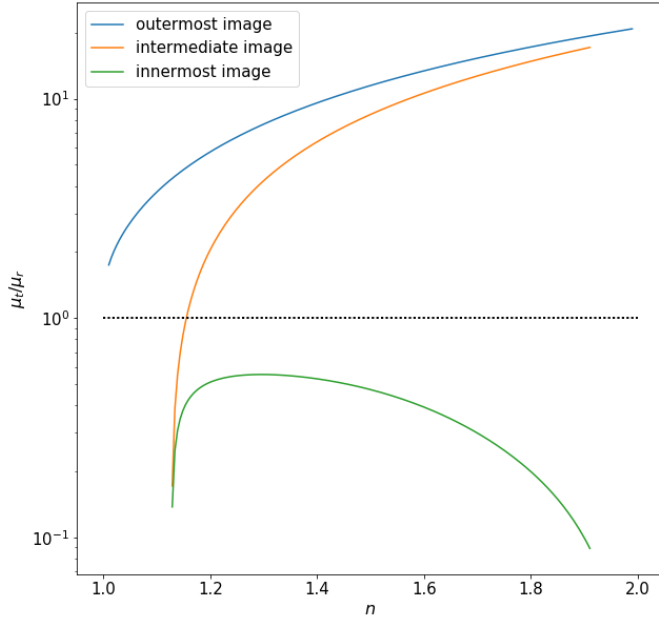


**Figure 4.2.4:** Magnification ratio at the position of the multiple images of a source at  $y = 0.2$ .

Einstein radius and for the inner images when they are close to the critical lines. On the contrary, the innermost image

In Fig. ??, we show the ratio of the tangential to radial magnification for each of the three images for a given value of  $y = 0.2$ . The outermost image is characterized by a tangential to radial magnification which always exceeds one. Thus the overall distortion of this image is always tangential. The innermost image is predominantly radially distorted. In the case shown in the Figure, the image is on the radial critical line for  $n \sim 1.13$ . For  $n$  smaller than this value, the source only has one image. Increasing  $n$ , the innermost image moves near the center (see Fig. 4.2.2), but so does the radial critical line. Consequently, the tangential-to-radial magnification ratio decreases also at large  $n$ . The intermediate image shows a transition from being predominantly radially to tangentially distorted as  $n$  increases. The reason is again that the radial critical line shrinks as  $n$  increases.

### 4.2.2 Lenses with $n > 2$

The power-law lenses with  $n \geq 2$  have the peculiarity that the deflection angle profile  $\alpha(x)$  is either flat ( $n = 2$ ) or singular  $n > 2$ . The case  $n = 2$  will be discussed in the next section. Here, we briefly discuss the case  $n > 2$ .

In particular, we focus on the image multiplicity. As shown in Fig. 4.2.5, such lenses always produce two images, one outside and one inside the Einstein radius. The image inside the Einstein radius approaches the lens center as  $y$  increases. For  $y = 0$ , the lens produces an Einstein ring. It can be easily seen that both images are radially

 Note that, for lenses of these kind the radial critical line does not exist.

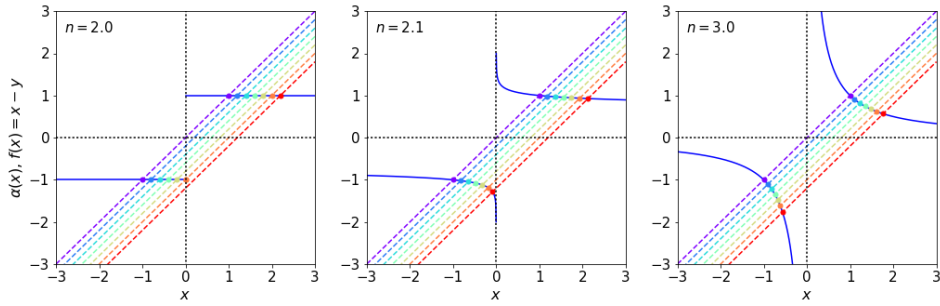


**Figure 4.2.5:** Image diagram for power-law lenses with  $n = 2.0$  (left panel),  $n = 2.1$  (central panel), and  $n = 3.0$  (right panel). The solid curves show the function  $\alpha(x)$ . The colored dashed lines show the function  $f(x) = x - y$  for a range of values of  $y \in [0, 1.2]$ .

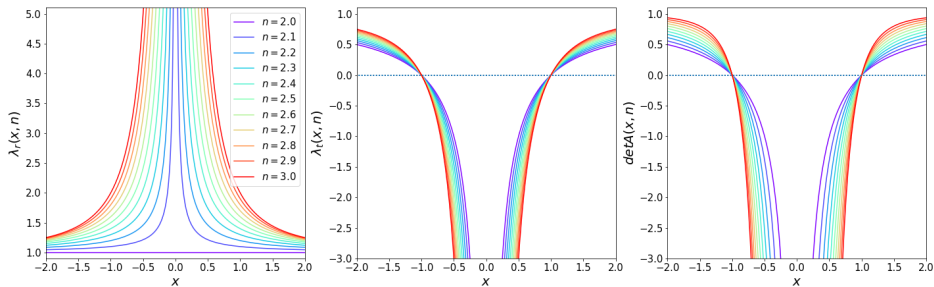


**Figure 4.2.6:** As in Fig. 4.2.6, but for  $n \geq 2$ .



Note that the case  $n = 3$  corresponds to the point-mass lens.

### 4.2.3 Singular Isothermal Sphere

One of the most widely used axially symmetric model is the Singular Isothermal Sphere (SIS hereafter). The density profile of this model can be derived assuming that the matter content of the lens behaves as an ideal gas confined by a spherically symmetric gravitational potential. This gas is taken to be in thermal and hydrostatic equilibrium. One of the two density profiles satisfying these sets of equations is given by

$$\rho(r) = \frac{\sigma_v^2}{2\pi G r^2}, \quad (4.48)$$

where  $\sigma_v$  is the velocity dispersion of the “gas” particles and  $r$  is the distance from the sphere center. By projecting the three-dimensional density along the line of sight, we obtain the corresponding surface density

$$\begin{aligned} \Sigma(\xi) &= 2 \frac{\sigma_v^2}{2\pi G} \int_0^\infty \frac{dz}{\xi^2 + z^2} \\ &= \frac{\sigma_v^2}{\pi G} \frac{1}{\xi} \left[ \arctan \frac{z}{\xi} \right]_0^\infty \\ &= \frac{\sigma_v^2}{2G\xi}. \end{aligned} \quad (4.49)$$

This density profile has a singularity at  $\xi = 0$ , where the density is ideally infinite. Nevertheless, it has been used to describe the matter distribution in galaxies, in particular because lensing

observations are consistent with the inner slope of this profile and because it can reproduce the flat rotation curves of spiral galaxies.

By choosing

$$\xi_0 = 4\pi \left(\frac{\sigma_v}{c}\right)^2 \frac{D_L D_{LS}}{D_S} \quad (4.50)$$

as the length scale on the lens plane, we obtain:

$$\Sigma(x) = \frac{\sigma_v^2}{2G\xi} \frac{\xi_0}{\xi_0} = \frac{1}{2x} \frac{c^2}{4\pi G} \frac{D_S}{D_L D_{LS}} = \frac{1}{2x} \Sigma_{cr}. \quad (4.51)$$

Thus, the convergence for the singular isothermal profile is

$$\kappa(x) = \frac{1}{2x}, \quad (4.52)$$

which shows that the SIS profile corresponds to the power-law lens with  $n = 2$ . Thus, the mass profile is

$$m(x) = |x|, \quad (4.53)$$

and the deflection angle is

$$\alpha(x) = \frac{x}{|x|}. \quad (4.54)$$

The lens equation reads

$$y = x - \frac{x}{|x|}. \quad (4.55)$$

As it can also be seen in the left panel of Fig. 4.2.5, if  $y < 1$ , two solutions of the lens equation exist. Their positions are  $x_- = y - 1$  and  $x_+ = y + 1$ , on opposite sides with respect to the lens center. The corresponding angular positions of the images are

$$\theta_\pm = \beta \pm \theta_E. \quad (4.56)$$

The angular separation between the two images is always  $\Delta(\theta) = 2\theta_E$ .

On the other hand, if  $y > 1$ , Eq. (4.55) has a unique solution,  $x_+ = y + 1$ . Thus, the circle of radius  $y = 1$  plays the same role of the radial caustic in the case of power-law lenses with  $1 < n < 2$ , separating the regions on the source plane corresponding to different image multiplicities. However, this circle is not a caustic, since  $d\alpha/dx = 0$  for any  $x$ , implying that  $\lambda_r = 1$ . The circle of radius  $y_c = 1$  is called the *cut*. We can see from the lens equation that

$$y_c = \lim_{x \rightarrow 0} y(x) = -\alpha(x). \quad (4.57)$$

The shear follows from Eqs. 4.13, 4.14, and 4.15. Since  $m(x)/x^2 = 1/x$ , the absolute value of  $\gamma$  is

$$\gamma(x) = \frac{m(x)}{x} - \kappa(x) = \frac{1}{2x}, \quad (4.58)$$

i.e. the shear and the convergence profiles coincide. The shear components are

$$\gamma_1 = -\frac{1}{2} \frac{\cos 2\phi}{x}, \quad (4.59)$$

$$\gamma_2 = -\frac{1}{2} \frac{\sin 2\phi}{x}. \quad (4.60)$$

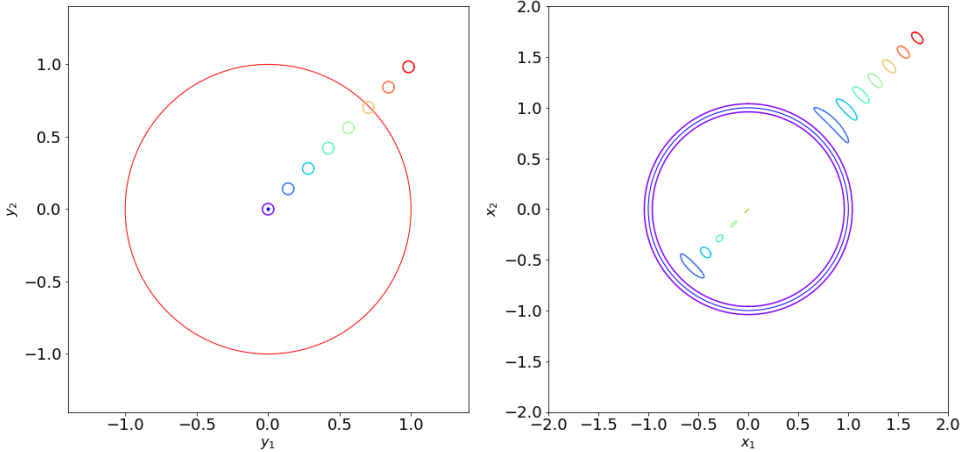


**Figure 4.2.7:** Imaging of extended sources by a SIS lens.

From Eq. (4.55), the magnification as a function of the image position is given by

$$\mu = \frac{|x|}{|x| - 1} . \quad (4.61)$$

Images are only magnified in the tangential direction, since the radial eigenvalue of the Jacobian matrix is unity everywhere.

If  $y < 1$ , the magnifications of the two images are

$$\mu_+ = \frac{y+1}{y} = 1 + \frac{1}{y} \quad ; \quad \mu_- = \frac{|y-1|}{|y-1|-1} = \frac{-y+1}{-y} = 1 - \frac{1}{y} , \quad (4.62)$$

from which we see that for  $y \rightarrow 1$ , the second image becomes weaker and weaker until it disappears at  $y = 1$ . On the other hand, for  $y \rightarrow \infty$ , the source magnification obviously tends to unity: sources which are at large distance from the lens can only be weakly magnified by gravitational lensing.

Note that  $\vec{x}_+$  is a minimum of the time-delay surface, being both eigenvalues of the Jacobian matrix positive at this location (positive parity). Instead,  $\vec{x}_-$ , is a saddle-point (negative parity), being the tangential eigenvalue negative.

In the left panel of Fig. 4.2.7, we show the cut (red circle) and the tangential caustic (blue point) of a SIS lens. In the same panel, several extended circular sources are displayed in different colors. In the right panel, the images of the same sources are shown, illustrating the results anticipated above. The blue circle is the tangential critical line, a.k.a. the Einstein ring. Note that a source placed on the caustic is imaged onto and extended Einstein ring.

### 4.3 Softened (Isothermal) Lenses

The class of lenses studied in the previous section is characterized by a central singularity in the convergence. Now, we discuss the properties of cored lenses. More precisely, we introduce a core in the SIS, obtaining a lens model which is often referenced as the Non-singular Isothermal Sphere (NIS).

The core is introduced in the surface density profile of the SIS as follows (1994A&A...284..285K):

$$\Sigma(\xi) = \frac{\sigma_v^2}{2G} \frac{1}{\sqrt{\xi^2 + \xi_c^2}} = \frac{\Sigma_0}{\sqrt{1 + \xi^2/\xi_c^2}} . \quad (4.63)$$

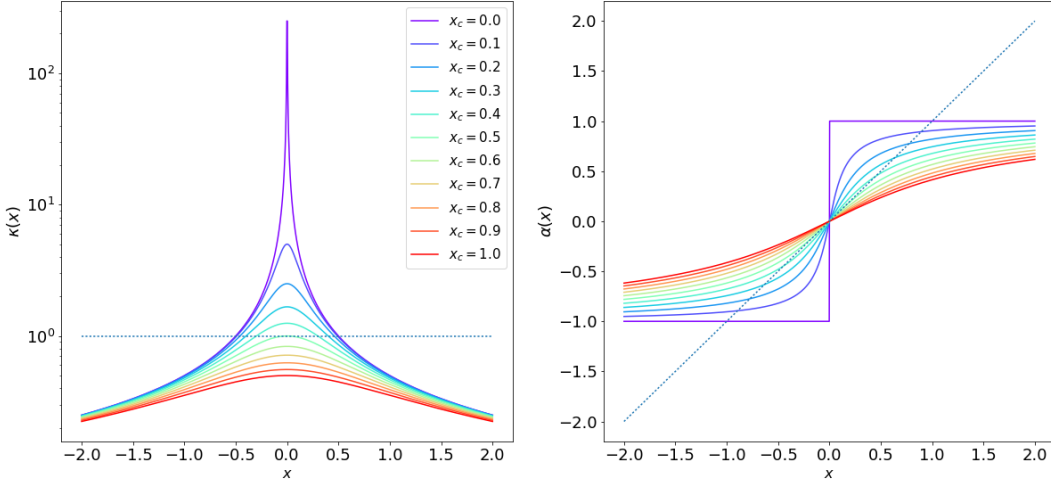


**Figure 4.3.1:** Convergence and deflection angle profiles of the NIS lens model. Different colors correspond to different values of the core radius  $x_c$ .

With this modification, the profile reaches a constant density

$$\Sigma_0 = \frac{\sigma_v^2}{2G\xi_c} \quad (4.64)$$

for  $\xi \ll \xi_c$ .

If we choose  $\xi_0 = 4\pi\sigma_v^2/c^2D_LD_{LS}/D_S$  (the Einstein radius of the SIS) to scale lengths on the lens plane, then

$$\kappa(x) = \frac{1}{2\sqrt{x^2 + x_c^2}} \quad (4.65)$$

It follows that the mass profile is

$$m(x) = 2 \int_0^x \kappa(x') x' dx' = \sqrt{x^2 + x_c^2} - x_c \quad (4.66)$$

and that the deflection angle profile is

$$\alpha(x) = \frac{m(x)}{x} = \sqrt{1 + \frac{x_c^2}{x^2}} - \frac{x_c}{x} \quad (4.67)$$

The convergence and the deflection angle profiles of the NIS lens model for different choices of  $x_c$  are shown in Fig 4.3.1. Note that in order to reach a central convergence  $\kappa(0) > 1$ , which implies that  $\Sigma(0) > \Sigma_{\text{cr}}$ , the core radius must be  $x_c < 1/2$ .

The shear can be derived with the usual relation given in Eq. 4.15, which gives

$$\gamma(x) = \frac{\sqrt{x^2 + x_c^2} - x_c}{x^2} - \frac{1}{2\sqrt{x^2 + x_c^2}} \quad (4.68)$$

Note that, since  $\xi_0$  is not the Einstein radius of the NIS, the radius of the tangential critical line does not satisfy the equation  $x_t = 1$ . Instead, it must be searched by solving the equation  $y/x = 0$ :

$$\sqrt{x^2 + x_c^2} - x_c = x^2, \quad (4.69)$$

which can be written as

$$x^2(x^2 + 2x_c - 1) = 0. \quad (4.70)$$

Discarding the solution  $x = 0$ , we find that

$$x_t = \sqrt{1 - 2x_c}. \quad (4.71)$$

Thus, the tangential critical line exists only for  $x_c < 1/2$ .

The radius of the radial critical line is found by solving the equation  $dy/dx = 0$ :

$$1 + \frac{\sqrt{x^2 + x_c^2} - x_c}{x^2} - \frac{1}{\sqrt{x^2 + x_c^2}} = 0 \quad (4.72)$$

which leads to

$$x_r^2 = \frac{1}{2} \left( 2x_c - x_c^2 - x_c \sqrt{x_c^2 + 4x_c} \right). \quad (4.73)$$

Note that  $x_r^2 \geq 0$  for  $x_c \leq 1/2$ . Thus, existence condition for the radial critical line is the same as for the tangential critical line.

While the tangential caustic is a point at  $y_t = 0$ , the radius of the radial caustic,  $y_r$ , can be obtained by inserting Eq. 4.73 into the lens equation.

The lens equation is

$$y = x - \frac{m(x)}{x} = x - \sqrt{1 + \frac{x_c^2}{x^2}} - \frac{x_c}{x}, \quad (4.74)$$

which can be reduced to the third order polynomial

$$x^3 - 2yx^2 + (y^2 + 2x_c - 1)x - 2yx_c = 0. \quad (4.75)$$

Thus, the NIS can produce up to three images of a source at distance  $y$  from the lens. Whether the images are three or less depends on  $y$  and on  $x_c$ . In particular, the right panel of Fig. 4.3.1 shows that if  $x_c > 1/2$ , which implies  $d\alpha/dx < 1$  for any  $x$ , there is no line  $f(x) = x - y$  which can intercept the function  $\alpha(x)$  more than once. Thus, the lens cannot produce multiple images independently on the position of the source with respect to the lens.

On the contrary, if  $x_c < 1/2$  multiple images exist whenever  $y < y_r$ . In the left panel of Fig. 4.3.3, some extended circular sources are placed at different distances  $y$  from the center of a NIS lens with  $x_c = 0.1$ . The blue point and the red circle show the tangential and the radial caustics. The right panel shows the corresponding critical lines (blue and red circles, respectively). The images of the sources displayed in the left panel are also shown. As seen for the power-law lens with  $1 < n < 2$ , one image form on the same side of the lens with respect to the source. This image, which corresponds to the minimum of the time-delay surface, is external to the Einstein ring. When the source is inside the radial caustic, two additional images form, one inside and one outside the radial critical line, which are located on the opposite side of the lens with respect to the source. As discussed earlier, the innermost image corresponds to the maximum of the time-delay surface, while the other image is at the saddle point. Thus the parity of this image is negative. If the source is overlapped to the radial caustic, these two image merge across the radial critical line, forming a radial arc. Bringing the source close to the tangential caustic causes the tangential distortion of the two outermost images to increase, until, when the source is exactly on the tangential caustic, the two image merge into the Einstein ring. The central image, instead is increasingly de-magnified and shifted to the center of the lens.

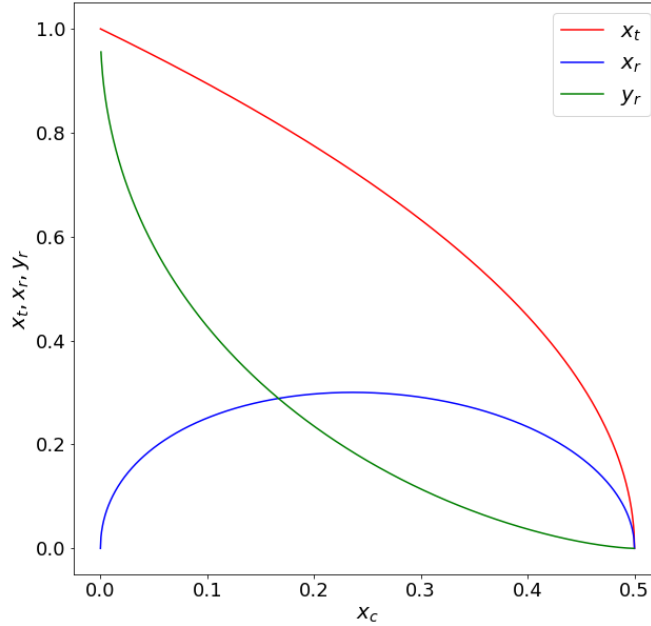


**Figure 4.3.2:** Radius of the radial and of the tangential critical lines as a function of the size of the core radius  $x_c$ . The green line shows the size of the radial caustic.

**R** We have shown that, if  $x_c > 1/2$ , the lens

- is sub-critical,  $\kappa(x) < 1$  for any  $x$ ;
- does not develop critical lines, i.e. is not capable of producing large distortions;
- does not produce multiple images.

Under these circumstances, the lens is considered *weak*. On the contrary, a *strong* lens is capable of producing large distortions and multiple images. As seen earlier, the number of these images depends on the position of the source with respect to the caustics. Sources which lie within the radial caustic produce three images. Sources outside the radial caustic have only one image. This is shown in Fig. ???. Since the tangential critical curve does not lead to a caustic curve, but the corresponding caustic degenerates to a single point  $\vec{y} = 0$ , the tangential critical curves have no influence on the image multiplicity. Thus, pairs of images can only be created or destroyed if the radial critical curve exists.

For non-singular axially symmetric lenses, whose surface density is piecewise continuous and falls off at large radii, such that it is bound, i.e.

$$0 \leq \kappa(x) \leq \kappa_{\max} \quad (4.76)$$

and

$$\lim_{x \rightarrow \infty} x \kappa(x) = 0. \quad (4.77)$$

it can be shown that the following properties hold (**1992grle.book.....S**), which generalize what shown earlier for NIS:

1. if the source is at  $y > 0$ , any image with  $x > 0$  is at  $x \geq y$ . This is easily seen from the lens equation:

$$x = y + \frac{m(x)}{x}. \quad (4.78)$$

Being  $m(x) \geq 0$  and  $x \geq 0$ , it follows that  $x \geq y$ ;

2. for sufficiently large  $y$ , there exists a single image. From Eq. 4.77, we see that there must be a constant  $c$  and a value  $a$  such that, for  $|x| > a$ ,  $\kappa(x) < c/|x|$ . This bounds the mass:

$$\begin{aligned} m(x) &= 2 \int_0^x x' \kappa(x') dx' \\ &= m(a) + 2 \int_a^{|x|} x' \kappa(x') dx' < m(a) + 2c(|x| - a). \end{aligned} \quad (4.79)$$

Thus,

$$\left| \frac{m(x)}{x} \right| < b. \quad (4.80)$$

If  $y$  is sufficiently large,  $y \geq b$ , the lens equation tells us that

$$x = y + \frac{m(x)}{x} > 0, \quad (4.81)$$

thus  $x \geq y$ . Moreover, if  $x > a$  then

$$\bar{\kappa} = \frac{m(x)}{x^2} = \frac{m(x)}{x} \frac{1}{x} < \frac{b}{x}. \quad (4.82)$$

Thus,

$$\lim_{x \rightarrow \infty} y = \lim_{x \rightarrow \infty} (1 - \bar{\kappa})x = x. \quad (4.83)$$

3. a lens can produce multiple images if and only if at least at one point  $1 - 2\kappa(x) + \bar{\kappa}(x) < 0$ : if  $1 - 2\kappa(x) + \bar{\kappa}(x) > 0$  throughout, a lens produces no multiple images, since  $y(x)$  increases monotonically. If on the other hand, there is a point where  $dy/dx < 0$ , there is at least one local maximum  $x_1$  and one local minimum  $x_2 > x_1$  of the curve  $y(x)$  since  $dy/dx \rightarrow 1$  for  $|x| \rightarrow \infty$ . For values of  $y$  such that  $y(x_2) < y < y(x_1)$ , there are at least three images;
4. a necessary condition for multiple images is that  $\kappa > 1/2$  at one point in the lens: if  $dy/dx < 0$  at one point, then  $\kappa > (1 + \bar{\kappa})/2 \geq 1/2$ ; a sufficient condition for multiple imaging is that  $\kappa > 1$  at one point. Indeed: if  $\kappa$  has a maximum at one point  $x_m$  where  $\kappa(x_m) > 1$ , then  $\bar{\kappa}(x_m) \leq \kappa(x_m)$  and  $dy/dx < 0$  at  $x_m$ . The statement then follows from (3);
5. if the surface density does not increase with  $x$ ,  $\kappa'(x) \leq 0$ ,  $\kappa(0) > 1$ : from (4) we know that it is sufficient that  $\kappa > 1$  at one point for having multiple images. On the other hand if  $\kappa(0) \leq 1$ , then, since  $y = x(1 - \bar{\kappa})$ , we have for  $x \geq 0$ :  $dy/dx = (1 - \bar{\kappa}) - x\bar{\kappa}'$ . Since

$$\bar{\kappa}(x) = 2 \int_0^1 du u \kappa(ux), \quad (4.84)$$

then

$$\frac{d\bar{\kappa}}{dx} = 2 \int_0^1 du u^2 \kappa'(ux) \leq 0 \quad (4.85)$$

and  $\bar{\kappa}(x) \leq \kappa(0) \leq 1$ , we see that  $dy/dx \geq 0$ , so that no multiple images can occur.

## 4.4 Time delays

As seen in Sect. 2.6, lensing introduces a delay in the time needed to photons to reach the observer after being emitted by the source. The delay, which has both a geometrical and a gravitational component is different for multiple images of the same source. While the absolute delay of each image cannot be measured, it is possible, in some particular cases, to measure the relative delay of the images. For example, time delays can be measured when the source is intrinsically variable, like e.g. AGNs or supernovae.

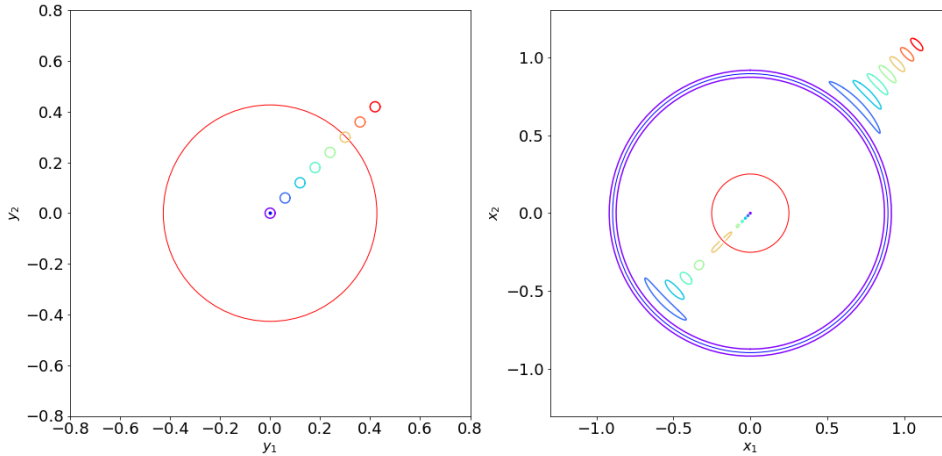


**Figure 4.3.3:** Imaging of extended sources by a NIS lens.

In this section, we compute the time delays between images for the lens models introduced above. The formula for the light travel time is

$$t(x) = \frac{(1+z_L)}{c} \frac{D_L D_S}{D_{LS}} \frac{\xi_0^2}{D_L^2} \left[ \frac{1}{2}(x-y)^2 - \Psi(x) \right] = \frac{(1+z_L)}{c} \frac{D_L D_S}{D_{LS}} \tau(x) \quad (4.86)$$

Obviously, in order to compute the light travel time, we need to provide the equations of the lensing potential.

For a power-law lens, the lensing potential is

$$\Psi(x) = \frac{1}{3-n} x^{3-n} \quad (4.87)$$

so that

$$\tau(x) = \frac{\xi_0^2}{D_L^2} \left[ \frac{1}{2}(x-y)^2 - \frac{1}{3-n} x^{3-n} \right] \quad (4.88)$$

At the image positions

$$x - y = \alpha(x) = x^{2-n} \quad (4.89)$$

thus

$$\tau(x_i) = \frac{\xi_0^2}{D_L^2} \left[ \frac{1}{2} x_i^{2(2-n)} - \frac{1}{3-n} x_i^{3-n} \right] \quad (4.90)$$

We can then compute the time delay between the images:

$$\Delta t_{ij} \propto \Delta \tau_{ij} = \frac{\xi_0^2}{D_L^2} \left[ \frac{1}{2} (x_j^{2(2-n)} - x_i^{2(2-n)}) - \frac{1}{3-n} (x_j^{3-n} - x_i^{3-n}) \right] \quad (4.91)$$

For  $n = 2$ , this formula gives:

$$\Delta \tau_{ij} = \frac{\xi_0^2}{D_L^2} (x_i - x_j) = \theta_E^2 \left( \frac{\theta_i}{\theta_E} - \frac{\theta_j}{\theta_E} \right) = \frac{1}{2} (\theta_i^2 - \theta_j^2) = \Delta \tau_{SIS} \quad (4.92)$$

Note that the lensing potential of the SIS lens is  $\Psi(x) = x$ .

A similar procedure can be followed to compute the time delays between the images in the case of a NIS lens. In this case, the lensing potential is given by

$$\Psi(x, x_c) = \sqrt{x^2 + x_c^2} - x_c \ln \left( x_c + \sqrt{x^2 + x_c^2} \right). \quad (4.93)$$

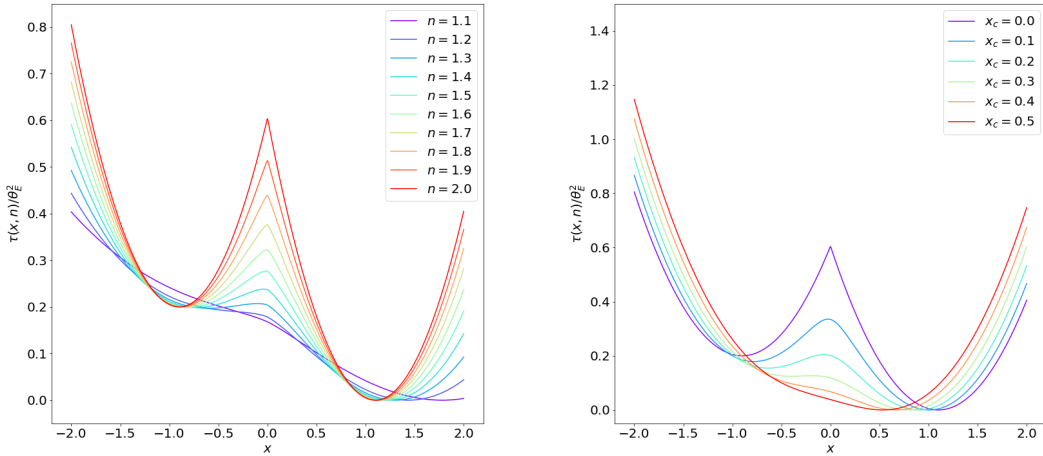


**Figure 4.4.1:** Time delay function for a number of power-law (left panel) and NIS lenses. In both cases the source is in  $y = 0.1$ .

Fig. 4.4.1 shows the time delay function for a source at  $y = 0.1$  for two classes of models, namely the power-law lens (left panel) and the NIS lens (right panel). In both panels, the delay is calculated with respect to outermost image (minimum of the time delay surface). As we can see, decreasing  $n$  and increasing  $x_c$  flattens-off the curves, thus reducing the time delays between the images.

## 4.5 Other profiles

### 4.5.1 The Navarro-Frenk-White model

**nfw97** (NFW hereafter) found that the density profile of dark matter halos numerically simulated in the framework of CDM cosmogony can be very well described by the radial function

$$\rho(r) = \frac{\rho_s}{(r/r_s)(1+r/r_s)^2}, \quad (4.94)$$

within the wide mass range  $3 \times 10^{11} \lesssim M_{vir}/(h^{-1}M_\odot) \lesssim 3 \times 10^{15}$ . The logarithmic slope of this density profile changes from  $-1$  at the center to  $-3$  at large radii. Therefore, it is flatter than that of the SIS in the inner part of the halo, and steeper in the outer part. The two parameters  $r_s$  and  $\rho_s$  are the scale radius and the characteristic density of the halo.

NFW parameterized dark matter halos by their masses  $M_{200}$ , i.e. the masses enclosed in spheres with radius  $r_{200}$  in which the average density is 200 times the critical density. The relationship between  $M_{200}$  and  $r_{200}$  is given by

$$r_{200} = 1.63 \times 10^{-2} \left( \frac{M_{200}}{h^{-1}M_\odot} \right)^{1/3} \left[ \frac{\Omega_0}{\Omega(z)} \right]^{-1/3} (1+z)^{-1} h^{-1} \text{ kpc}. \quad (4.95)$$

This definition depends on the redshift  $z$  at which the halo is identified as well as on the background cosmological model.

From the former definition of  $r_{200}$ , the *concentration*,  $c \equiv r_{200}/r_s$ , and the characteristic density are linked by the relation,

$$\rho_s = \frac{200}{3} \rho_{\text{cr}} \frac{c^3}{[\ln(1+c) - c/(1+c)]}. \quad (4.96)$$

Numerical simulations show that the scale radii of dark matter halos at any redshift  $z$  systematically change with mass in such a way that concentration is a characteristic function of  $M_{200}$ .

Several algorithms have been suggested for describing the concentration of dark matter halos. They are all based on the assumption that the central density of a halo reflects the mean cosmic density at the time when the halo formed. This is justified by numerical simulations of structure formation, which show that halos are the more concentrated the earlier they form. Originally, NFW devised the following approach. Each halo is assigned a collapse redshift, defined as the redshift at which half of the halo mass is contained in progenitors more massive than a fraction  $f_{\text{NFW}}$  of the final mass. Then, the characteristic density is taken to be some factor  $C$  times the mean cosmic density at the collapse redshift. For fitting the results of their numerical simulations, they use  $f_{\text{NFW}} = 0.01$  and  $C = 3 \times 10^3$ .

**bullock01** suggested a different definition, because they noticed that the concentrations of numerically simulated dark matter halos change more rapidly with redshift than predicted by the NFW approach. They define the collapse redshift such that the non-linear mass scale at that redshift is a fraction  $f_B$  of the final halo mass. The halo concentration is then assumed to be a factor  $K$  times the ratio of the scale factors at the redshift when the halo is identified and at the collapse redshift. The best fitting values they found when comparing to numerical simulations are  $f_B = 0.01$  and  $K = 4$ .

Finally, **eke01** suggested another different approach. The collapse redshift of a halo of mass  $M$  is defined such that the suitably defined amplitude of the linearly evolving power spectrum at the mass scale  $M$  matches a constant  $C_E^{-1}$ . The halo concentration is then obtained by setting the characteristic density equal to the spherical collapse density at the collapse epoch. Numerical results are well represented assuming  $C_E = 28$ .

The mass-dependence of the concentration parameter  $c$  is shown in Fig. (??) for all the definitions of halo concentration discussed before and for different cosmological models. The main features of these plots can be summarized as follows:

- although halo concentrations produced by these different algorithms differ in detail, they have in common that the concentration increases toward lower masses in all the cosmological models considered. This is a direct result of the higher collapse redshift of less massive systems;
- the concentration depends on cosmology. The collapse redshift is determined by  $\Omega_0$  and  $\Omega_{0\Lambda}$ : halos form earlier in open low-density universes, then in flat low-density universes and later in flat high-density universes. The concentration thus reflects the mean cosmic density at the time when they collapse. For example, halos in an OCDM model ( $\Omega_0 = 0.3$ ,  $\Omega_{0\Lambda} = 0$ ) are generally more concentrated than halos in  $\Lambda$ CDM ( $\Omega_0 = 0.3$ ,  $\Omega_{0\Lambda} = 0.7$ ) or SCDM ( $\Omega_0 = 1$ ,  $\Omega_{0\Lambda} = 0$ ) models, because they form earlier and the mean cosmic density is higher when they collapse. On the other hand, halos formed in a low-density  $\Lambda$ CDM model are less concentrated than those formed in the SCDM model: even if they have a higher collapse redshift, the mean cosmic density is lower when they form.

Several different aspects of lensing by halos with NFW or generalized NFW profiles can be found in Bartelmann **bartelmann96** Wright & Brainerd **wright00** Li & Ostriker **li02** Wyithe, Turner & Spergel **wyithe01** Perrotta et al. **perrotta02** Meneghetti et al. **meneghetti02** Bartelmann

et al. **bartelmann02a; bartelmann02b** If we take  $\xi_0 = r_s$ , the density profile (4.94) implies the surface mass density

$$\Sigma(x) = \frac{2\rho_s r_s}{x^2 - 1} f(x), \quad (4.97)$$

with

$$f(x) = \begin{cases} 1 - \frac{2}{\sqrt{x^2-1}} \arctan \sqrt{\frac{x-1}{x+1}} & (x > 1) \\ 1 - \frac{2}{\sqrt{1-x^2}} \operatorname{arctanh} \sqrt{\frac{1-x}{1+x}} & (x < 1) \\ 0 & (x = 1) \end{cases}. \quad (4.98)$$

The lensing potential is given by

$$\Psi(x) = 4\kappa_s g(x), \quad (4.99)$$

where

$$g(x) = \frac{1}{2} \ln^2 \frac{x}{2} + \begin{cases} 2 \arctan^2 \sqrt{\frac{x-1}{x+1}} & (x > 1) \\ -2 \operatorname{arctanh}^2 \sqrt{\frac{1-x}{1+x}} & (x < 1) \\ 0 & (x = 1) \end{cases}, \quad (4.100)$$

and  $\kappa_s \equiv \rho_s r_s \Sigma_{\text{cr}}^{-1}$ . This implies the deflection angle

$$\alpha(x) = \frac{4\kappa_s}{x} h(x), \quad (4.101)$$

with

$$h(x) = \ln \frac{x}{2} + \begin{cases} \frac{2}{\sqrt{x^2-1}} \arctan \sqrt{\frac{x-1}{x+1}} & (x > 1) \\ \frac{2}{\sqrt{1-x^2}} \operatorname{arctanh} \sqrt{\frac{1-x}{1+x}} & (x < 1) \\ 1 & (x = 1) \end{cases}. \quad (4.102)$$

It is an important feature of the NFW lensing potential [Eq. (4.99)] that its radial profile is considerably less curved near the center than the SIS profile [Eq. (??)]. Since the local imaging properties are determined by the curvature of  $\Psi$ , this immediately implies substantial changes to the lensing properties [see Fig. (??)].

The convergence can be written as

$$\kappa(x) = \frac{\Sigma(\xi_0 x)}{\Sigma_{\text{cr}}} = 2\kappa_s \frac{f(x)}{x^2 - 1}, \quad (4.103)$$

from which we obtain the dimensionless mass,

$$m(x) = 2 \int_0^x \kappa(x') x' dx' = 4\kappa_s h(x). \quad (4.104)$$

The lens equation for this kind of lens model can be solved by using numerical methods. At fixed halo mass, the critical curves of an NFW lens are closer to its center than for SIS lens because of its flatter density profile. There, the potential is less curved, thus the image magnification is larger and decreases more slowly away from the critical curves. Therefore NFW lenses are less efficient in image splitting than SIS lenses, but comparably efficient in image magnification.

#### 4.5.2 The Pseudo-Isothermal model

### 4.6 Elliptical lenses

Having explored the effects of changing the slope of the density profile and of including a central core, we consider now how ellipticity affects the lens properties. This of course removes the axial symmetry of the lens. Consequently, the tangential caustic is no longer a point at the center of the lens. Instead, it becomes an astroid-like kind of caustic which can have two or four cusps.

#### 4.6.1 Singular Isothermal Ellipsoid

As we have seen in the previous section, the singular isothermal profile is particularly tractable to derive its lensing properties. Similarly, it is quite straightforward to generalize to the elliptical case.

##### Convergence

As shown by **1994A&A...284..285K** the Singular Isothermal Ellipsoid model (SIE) can be derived from the SIS by making the substitution

$$\xi \Rightarrow \sqrt{\xi_1^2 + f^2 \xi_2^2}, \quad (4.105)$$

With this substitution,  $\Sigma(\xi)$  becomes

$$\Sigma(\vec{\xi}) = \frac{\sigma_v^2}{2G} \frac{\sqrt{f}}{\sqrt{\xi_1^2 + f^2 \xi_2^2}}, \quad (4.106)$$

which is constant on ellipses with minor axis  $\xi$  and major axis  $\xi/\sqrt{f}$ , oriented such that the major axis is along the  $\xi_2$  axis. In the above formulas,  $f$  is the axis ratio of the ellipses.

By choosing  $\xi_0 = \xi_{0,SIS}$  as reference scale, and using polar coordinates, we obtain

$$\kappa(x, \varphi) = \frac{\sqrt{f}}{2x\Delta(\varphi)}, \quad (4.107)$$

where

$$\Delta(\varphi) = \sqrt{\cos \varphi^2 + f^2 \sin \varphi^2}. \quad (4.108)$$

##### Lensing potential

The lensing potential can be found by solving the Poisson equation:

$$\frac{\partial^2 \psi}{\partial x^2} + \frac{1}{x} \frac{\partial \psi}{\partial x} + \frac{1}{x^2} \frac{\partial \psi}{\partial \varphi} = 2\kappa = \frac{\sqrt{f}}{\Delta(\varphi)}. \quad (4.109)$$

Making the ansatz  $\psi(x, \varphi) := x\tilde{\psi}(\varphi)$  and using Green's method, we find

$$\psi(x, \varphi) = x \frac{\sqrt{f}}{f'} [\sin \varphi \arcsin(f' \sin \varphi) + \cos \varphi \operatorname{arcsinh}(f'/f \cos \varphi)]. \quad (4.110)$$

In the formula above we introduced  $f' = \sqrt{1 - f^2}$ .

##### Deflection angle

The deflection angle can be derived as usual by taking the gradient of the lensing potential. It is convenient to operate in polar coordinates, so that

$$\frac{\partial}{\partial x_1} = \cos \varphi \frac{\partial}{\partial x} - \frac{\sin \varphi}{x} \frac{\partial}{\partial \varphi} \quad (4.111)$$

and

$$\frac{\partial}{\partial x_2} = \sin \varphi \frac{\partial}{\partial x} + \frac{\cos \varphi}{x} \frac{\partial}{\partial \varphi}. \quad (4.112)$$

Thus, the components of the deflection angle are

$$\begin{aligned} \alpha_1(\vec{x}) &= \frac{\sqrt{f}}{f'} \operatorname{arcsinh} \left( \frac{f'}{f} \cos \varphi \right) \\ \alpha_2(\vec{x}) &= \frac{\sqrt{f}}{f'} \operatorname{arcsin} (f' \sin \varphi) \end{aligned} \quad (4.113)$$

As found for the SIS, the deflection angle of the SIE does not depend on  $x$ .

### Shear

The further step is the derivation of the shear components. These can be derived by means of the derivatives of the deflection angle:

$$\begin{aligned} \gamma_1 &= \frac{1}{2} \left( \frac{\partial \alpha_1}{\partial x_1} - \frac{\partial \alpha_2}{\partial x_2} \right) \\ \gamma_2 &= \frac{\partial \alpha_1}{\partial x_2} \end{aligned} \quad (4.114)$$

Using the differential operators in polar coordinates and the results above, we find that

$$\begin{aligned} \gamma_1 &= -\frac{\sqrt{f}}{2x\Delta(\varphi)} \cos 2\varphi = -\kappa \cos 2\varphi \\ \gamma_2 &= -\frac{\sqrt{f}}{2x\Delta(\varphi)} \sin 2\varphi = -\kappa \sin 2\varphi, \end{aligned} \quad (4.115)$$

which shows that  $\gamma = \kappa$  as for the SIS.

### Critical lines

We can now compute the lensing Jacobian. This is

$$A = \begin{bmatrix} 1 - \kappa - \gamma_1 & -\gamma_2 \\ \gamma_2 & 1 - \kappa + \gamma_1 \end{bmatrix} = \begin{bmatrix} 1 - 2\kappa \sin^2 \varphi & \kappa \sin 2\varphi \\ \kappa \sin 2\varphi & 1 - 2\kappa \cos^2 \varphi \end{bmatrix} \quad (4.116)$$

and that the tangential and radial eigenvalues are

$$\lambda_t = 1 - \kappa - \gamma = 1 - 2\kappa \quad (4.117)$$

$$\lambda_r = 1 - \kappa + \gamma = 1. \quad (4.118)$$

It turns out that, as the SIS, even the SIE does not have a radial critical line, being the radial magnification always unity. Instead, the tangential critical line is the ellipse where

$$\kappa = \frac{1}{2}, \quad (4.119)$$

which can be parametrized as follows:

$$\vec{x}_t(\varphi) = \frac{\sqrt{f}}{\Delta(\varphi)} [\cos \varphi, \sin \varphi]. \quad (4.120)$$

The critical line for a SIE lens is shown in the left panel of Fig. ???. This line can be mapped onto the source plane using the lens equation, to obtain the tangential caustic:

$$\begin{aligned} y_{t,1} &= \frac{\sqrt{f}}{\Delta(\varphi)} \cos \varphi - \frac{\sqrt{f}}{f'} \operatorname{arcsinh} \left( \frac{f'}{f} \cos \varphi \right) \\ y_{t,2} &= \frac{\sqrt{f}}{\Delta(\varphi)} \sin \varphi - \frac{\sqrt{f}}{f'} \operatorname{arcsin} (f' \sin \varphi). \end{aligned} \quad (4.121)$$

### Cut and caustic

As for the SIS (see Eq. 4.57), we can now search for the *cut*, which is given by

$$\vec{y}_c = \lim_{x \rightarrow 0} \vec{y}(x, \varphi) = -\vec{\alpha}(\varphi). \quad (4.122)$$

Thus, we obtain

$$\begin{aligned} y_{c,1} &= -\frac{\sqrt{f}}{f'} \operatorname{arcsinh} \left( \frac{f'}{f} \cos \varphi \right) \\ y_{c,2} &= -\frac{\sqrt{f}}{f'} \operatorname{arcsin} (f' \sin \varphi). \end{aligned} \quad (4.123)$$

Both the caustic and the cut are shown in the right panel of Fig. ?? (red and blue curves, respectively).

The cut and the caustic intercept the  $y_1$  and the  $y_2$  axes in points that are symmetric with respect to the center of the lens. These points have coordinates

$$\begin{aligned} s_{1,\pm,c} &= [y_{c,1}(\varphi = 0, \pi), 0], \\ s_{2,\pm,c} &= [0, y_{c,2}(\varphi = \pi/2, -\pi/2)] \end{aligned} \quad (4.124)$$

for the cut, and

$$\begin{aligned} s_{1,\pm,t} &= [y_{t,1}(\varphi = 0, \pi), 0], \\ s_{1,\pm,t} &= [0, y_{t,2}(\varphi = \pi/2, -\pi/2)] \end{aligned} \quad (4.125)$$

for the caustic.

Fig. ?? shows how the axis intercepts  $s_1$  and  $s_2$  on the positive  $y_1$  and  $y_2$  axes of both the cut and the caustic vary as a function of  $f$ . Clearly,  $s_{1,c} > s_{1,t}$  for any  $f$ . On the contrary, there exists a value,  $f = f_0 = 0.3942$ , such that

$$\begin{aligned} s_{2,c} &\leq s_{2,t} \text{ for } f \leq f_0, \\ s_{2,c} &> s_{2,t} \text{ for } f > f_0. \end{aligned} \quad (4.126)$$

Therefore, the tangential caustic is not always contained by the cut. For large ellipticities, corresponding to lower values of  $f$ , the tangential caustic extends outside the cut along the  $y_2$  axis. The cusps which are not contained within the cut are called *naked*.

### Multiple images

Finding the multiple images of a source lensed by the SIE model requires using numerical methods. The implementation of one of such algorithms in python is discussed in Sect. 4.10.1.

In order to understand how the mapping between the lens and the source plane works, it is useful to inspect how pieces of the tangential critical line are mapped onto the caustic. In the left panel of Fig. ??, we divide the critical line in four parts, corresponding to the quadrants in the lens plane. Different colors are used to indicate the critical points with polar angles in the ranges  $[0, \pi/2]$ ,  $[\pi/2, \pi]$ ,  $[\pi, 3/2\pi]$ , and  $[3/2\pi, 2\pi]$  (see Eq. 4.120). In the right panel, the corresponding points on the caustic, obtained using Eq. 4.121, are shown using the same colors. We use the same color-code to visualize the points on the cut, depending on the polar angle  $\varphi$ .

We can see that the mapping of the critical points follows a left-right rule: the first and the fourth quadrants in the lens plane ( $\varphi \in [0, \pi/2]$  and  $\varphi \in [3/2\pi, 2\pi]$ ) are mapped onto the second and the third quadrants in the source plane, and vice versa.

The points on the cut, instead, follow a diagonal rule. For example, the portion of the cut in the first quadrant in the source plane, correspond to  $\varphi \in [\pi, 3/2\pi]$ .

**R** As seen earlier, in lenses which have a radial critical line, the cut becomes the radial caustic. Thus the same diagonal rule works for the mapping of the radial critical points onto the radial caustic.

**R** With this result in mind, we can easily guess where, on the source plane, a source originating images near some portion of the critical line is located.

The multiplicity of the images that a SIE lens can produce depends on the structure of the caustics and cut, and on the relative position of the source. The following rules apply. Compared to a source far away from the lens

- the number of images increases by one, if the source is inside the cut;
- the number of images increases by two, if the source is inside the caustic.

The two rules do not exclude each other, i.e. if the source is inside the cut AND the caustic, the number of images is increased by three. Thus, a SIE lens can produce up to four images of a single source. More precisely:

- if  $f > f_0$ , the lens can produce either 1, 2, or 4 images, depending on the source being outside the cut, between the cut and the caustic, or inside the caustic;
- if  $f \leq f_0$ , the lens can produce 1, 2, 3, or 4 images. Indeed, for such lenses, a source can be located within the caustic but be outside the cut. Thus, an image multiplicity of three is allowed in this case.

In Fig. ??, the image positions for sources at different locations with respect to the caustic and the cut are shown. The upper and the middle panels refer to a lens with  $f = 0.6$ , while the bottom panels refer to a lens with  $f = 0.2$ . The solid and the dashed red lines in left panels indicate the caustics and the cut, respectively. The colored stars mark the positions of several point sources. The corresponding images are shown in the right panels, where the tangential critical lines are given by the solid blue lines.

The upper panels show how the image geometry changes when the source is brought closer to the lens center by crossing the cut and the fold of the caustic. Sources outside the cut have only one image, which is located in the same quadrant of the image plane onto which the source position is projected. When the source crosses the cut, one additional image appears near the center of the lens. This is not surprising, given that the cut is given by Eq. 4.122. As the source is brought closer towards the caustic, the central image moves away from the lens center in the quadrant of the lens plane opposite to that where source is projected. In this case, the above mentioned diagonal rule applies. At the caustic crossing two images appear on opposite sides of the critical line. Note that, if the source is near the fold in the first quadrant of the source plane, these two images appear in the second quadrant of the lens plane, following the left-right mapping rule which applies to the tangential critical points. As the source is brought even closer to the center of the lens, the images reach a symmetric configuration which is called *Einstein cross*.

The middle panels refer to the same lens, but the source is moved from outside the cut towards the center of the lens passing through the cusp of the tangential caustic. In this case, three images meet at the critical line when the source is on the cusp. Again, the left-right rule applies.

Finally, the bottom panels show the image configurations of a source moved across the naked cusp. When the source is on the cusp, we find again that three images merge into a single image. As the source is inside the caustic but still outside the cut, the image multiplicity is three, as anticipated earlier.

### Distortion and parity of the images

We can now comment on the magnification and parity. From Eqs. 4.107 and 4.115, we obtain that

$$\mu = \frac{1}{1 - 2\kappa}, \quad (4.127)$$

meaning that  $\mu > 0$  for  $\kappa < 0.5$ . Therefore, the parity of the images is positive outside the critical line, negative otherwise.

Given the singularity of the lensing potential near the center, the images are either minima or saddle points of the time-delay surface. The images inside the critical line are saddle points. Those outside the critical line are minima.

The magnification of the images forming near the center of the lens is very small  $|\mu| \sim 0$ , being  $\kappa$  divergent. Because the radial magnification is always unity, this means that the images are tangentially squeezed if they are located near the center of the lens. Of course, the magnification of the images near the critical line diverges.

Magnification and distortion are better understood using extended sources. The examples in Fig. ?? show the images of circular sources at different positions with respect to the caustic and the cut. The procedure to numerically find these images is explained in Sect. 4.10.2. The figure shows how the images forming near the critical line are distorted tangentially to the mass distribution. The images are elongated and merge across the critical line. In the bottom panels, we can see that the largest gravitational arcs are the result of the merger of three images of sources near the cusp of the caustic.

In the examples shown in Fig. ?? the source size is 0.05 in units of  $\xi_0$ . In Fig. ??, we show how a source of radius 0.25 placed on the caustic is distorted to form a complete Einstein ring. Thus, the observed distortions depend on the size of the source relative to the size of the caustic. Thus, if the source size is comparable to the size of the lens caustic, the perturbation due to ellipticity is merely detectable as a distortion of the images compared to the case of an axially symmetric lens.

Fig. ?? illustrates how the parity of the images changes from inside to outside the critical line. Within each source in the left panel we mark four characteristic points. Starting from right-most and counting counter-clockwise, they are indicated by the symbols circle, triangle, square, and star. In the right panel, we can see that the same symbol sequence is preserved in images outside the critical line. On the other hand, in the images inside the critical line the circles and the squares are exchanged, following the left-right rule introduced above.

Note that half of the source overlapping with the fold of the caustic is outside the caustic itself. Therefore, only half of this source is mapped onto four images. For example, the points marked with the circle and the triangle in this source do not appear in the fold arc in the second quadrant of the lens plane.

### 4.6.2 Non-singular elliptical models

Nothing prevents from including a core in the SIE model. In this case, however, the model becomes not easily tractable analytically. A discussion on the properties of the Non-singular Isothermal Ellipsoid (NIE) is given in **1994A&A...284..285K** Similar complications arise from changing the slope of the density profile. A detailed description of the elliptical power-law lens can be found in **2015A&A...580A..79T**

Here, we limit to discuss the transformation of the critical lines and caustics in the case of the NIE, summarizing the results of **1994A&A...284..285K** The surface density of the NIE model is written as

$$\Sigma(\vec{\xi}) = \frac{\sigma^2}{2G} \frac{\sqrt{f}}{\sqrt{\xi_1^2 + f^2 \xi_2^2 + \xi_c^2}}, \quad (4.128)$$

where  $\xi_c$  is the core radius. With the usual choice of  $\xi_0 = \xi_{0,SIS}$ , the convergence profile becomes

$$\kappa(\vec{x}) = \frac{\sqrt{f}}{2\sqrt{x_1^2 + f^2 x_2^2 + x_c^2}}. \quad (4.129)$$

**1994A&A...284..285K** showed that the critical lines and caustics of the NIE can be derived analytically. Some examples are shown in Fig. ???. Depending on the values of  $f$  and of  $x_c$ , the lens can have two separate critical lines and caustics (one radial and one tangential), only one critical line and caustic (tangential), or no critical lines and caustics at all. In particular:

- if  $x_c < f^{3/2}/2$  there are two distinguished critical lines and caustics. One caustic is the tangential caustic and has four cusps. The other is the radial one and it has not cusps. The tangential caustic is completely contained within the radial caustic if the ellipticity is small ( $f$  is large). Even in the case of mildly elliptical lenses, the radial caustic contains the tangential caustic if the core is small enough;
- if  $f^{3/2}/2 < x_c < f^{3/2}/(1+f)$ , the radial caustic is contained within the tangential caustic. In addition both the radial and the tangential caustics have only two cusps;
- if  $f^{3/2}/(1+f) < x_c < f^{1/2}/(1+f)$ , the lens has only a tangential critical line and caustic. The radial critical lines and caustics disappear for  $x_c = f^{3/2}/(1+f)$ ;
- even the tangential caustic disappears if  $x_c = f^{1/2}/(1+f)$ . Thus, for  $x_c > f^{1/2}/(1+f)$  the lens does not have critical lines and caustics.

In the case of elliptical models with both the critical lines and caustics

#### 4.6.3 Pseudo-elliptical models

(1993ApJ...417..450K)

### 4.7 Environment

It is often necessary to embed a lens into an external shear field which is created by matter in the lens surroundings. A useful approach is to model this shear by means of a potential  $\Psi_\gamma$ , which must satisfy the following conditions:

$$\begin{aligned}\gamma_1 &= \frac{1}{2}(\Psi_{11} - \Psi_{22}) = \text{const.} \\ \gamma_2 &= \Psi_{12} = \text{const.} \\ \kappa &= \frac{1}{2}(\Psi_{11} + \Psi_{22}) = \text{const.}.\end{aligned}\quad (4.130)$$

If  $\Psi_{11} \pm \Psi_{22}$  are required to be constant,  $\Psi_{11}$  and  $\Psi_{22}$  must separately be constants, thus

$$\Psi_\gamma = Cx_1^2 + C'x_2^2 + Dx_1x_2 + E. \quad (4.131)$$

This requires

$$\begin{aligned}\frac{1}{2}(\Psi_{11} - \Psi_{22}) &= C - C' = \gamma_1 \\ \Psi_{12} &= D = \gamma_2 \\ \frac{1}{2}(\Psi_{11} + \Psi_{22}) &= C + C' = \kappa\end{aligned}\quad (4.132)$$

Imposing  $\kappa = 0$ , we obtain

$$C = -C' \Rightarrow C = \frac{\gamma_1}{2}. \quad (4.133)$$

Therefore,

$$\Psi_\gamma = \frac{\gamma_1}{2}(x_1^2 - x_2^2) + \gamma_2 x_1 x_2 \quad (4.134)$$

Likewise, if we want to place our lens on a sheet of constant surface-mass density, the shear of that sheet must be zero (because no direction can be preferred), and from Eq. 4.132 we find

$$\Psi_\kappa = \frac{\kappa}{2}(x_1^2 + x_2^2) . \quad (4.135)$$

Irrelevant constants have been suppressed above.

We can now embed e.g. a softened isothermal sphere into a constant shear field,

$$\Psi = \sqrt{x^2 + x_c^2} + \frac{\gamma_1}{2}(x_1^2 - x_2^2) + \gamma_2 x_1 x_2 \quad (4.136)$$

yielding the deflection angle

$$\begin{aligned} \vec{\nabla}\Psi &= \frac{\vec{x}}{\sqrt{x^2 + x_c^2}} + \begin{pmatrix} \gamma_1 x_1 + \gamma_2 x_2 \\ -\gamma_1 x_2 + \gamma_2 x_1 \end{pmatrix} \\ &= \frac{\vec{x}}{\sqrt{x^2 + x_c^2}} + \begin{pmatrix} \gamma_1 & \gamma_2 \\ \gamma_2 & -\gamma_1 \end{pmatrix} \vec{x} \end{aligned} \quad (4.137)$$

and the convergence remains unchanged by construction.

The deflection angle of a sheet of constant surface-mass density is

$$\vec{\alpha} = \vec{\nabla}\Psi_\kappa = \kappa \vec{x} . \quad (4.138)$$

Thus, the lens equation reads, in this case,

$$\vec{y} = \vec{x} - \vec{\alpha} = \vec{x}(1 - \kappa) . \quad (4.139)$$

If  $\kappa = 1$ ,  $y = 0$  for all images, i.e. this sheet focuses all light rays exactly on the origin. This gravitational lens thus has a well-defined focal point.

**R** When combining the potentials of the lens and of external perturbers the same scale  $\xi_0$  must be chosen if using dimensionless units.

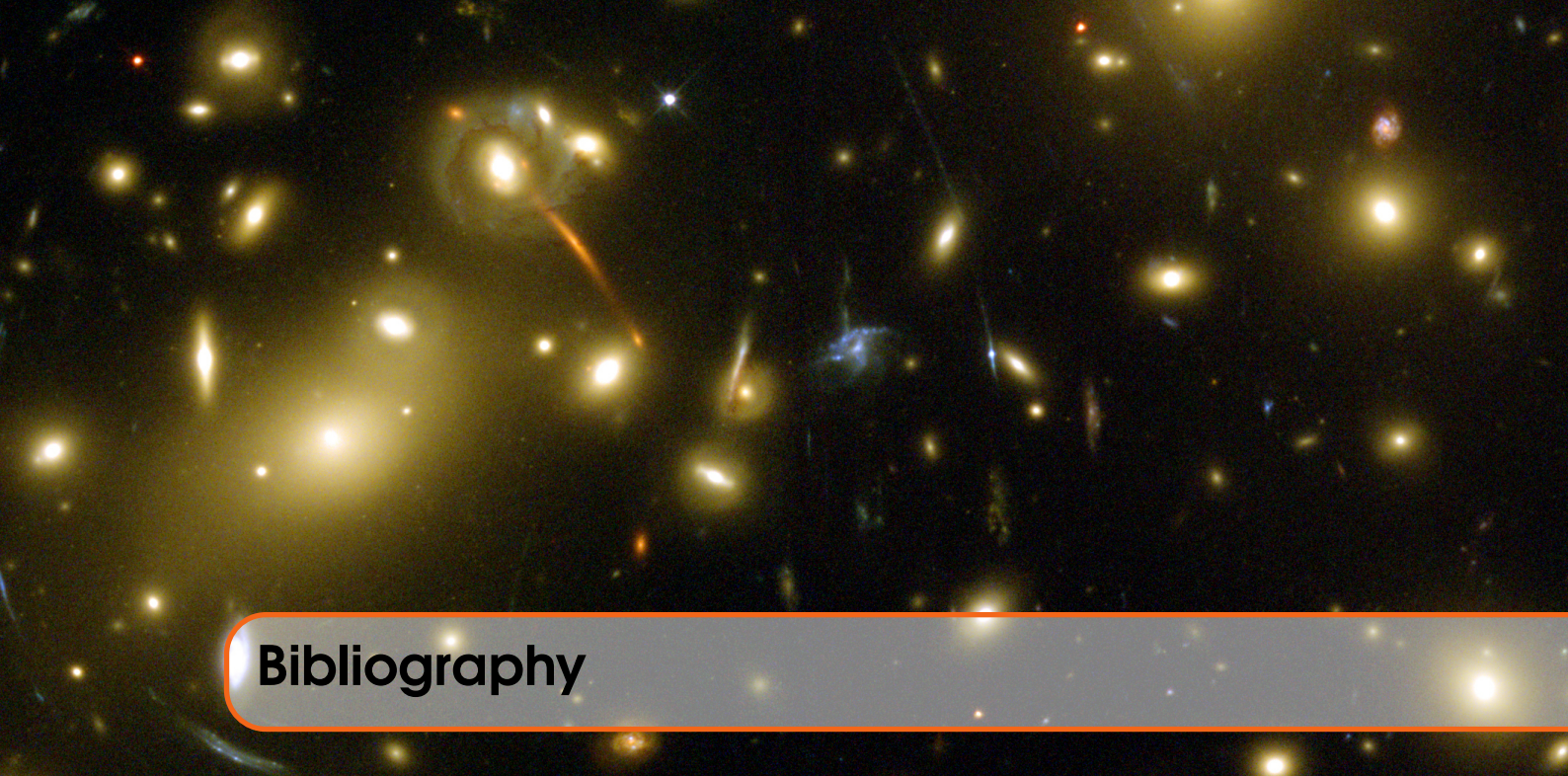
## 4.8 Substructures

## 4.9 Mass-sheet degeneracy

## 4.10 Python applications

### 4.10.1 Multiple images by SIE lenses

### 4.10.2 Images of extended sources



## Bibliography

- Aubert, D., A. Amara, and R. B. Metcalf (2007). “Smooth Particle Lensing”. In: *MNRAS* 376, pages 113–124. DOI: [10.1111/j.1365-2966.2006.11296.x](https://doi.org/10.1111/j.1365-2966.2006.11296.x). eprint: [astro-ph/0604360](https://arxiv.org/abs/astro-ph/0604360) (cited on page 18).
- Barnes, J. and P. Hut (1986). “A hierarchical O( $N \log N$ ) force-calculation algorithm”. In: *Nature* 324, pages 446–449. DOI: [10.1038/324446a0](https://doi.org/10.1038/324446a0) (cited on page 18).
- Bartelmann, M. and P. Schneider (2001). “Weak gravitational lensing”. In: *Phys.Rep.* 340, pages 291–472. DOI: [10.1016/S0370-1573\(00\)00082-X](https://doi.org/10.1016/S0370-1573(00)00082-X). eprint: [astro-ph/9912508](https://arxiv.org/abs/astro-ph/9912508) (cited on page 30).
- Bozza, V. (2010). “Gravitational lensing by black holes”. In: *General Relativity and Gravitation* 42, pages 2269–2300. DOI: [10.1007/s10714-010-0988-2](https://doi.org/10.1007/s10714-010-0988-2). arXiv: [0911.2187 \[gr-qc\]](https://arxiv.org/abs/0911.2187) (cited on page 17).
- Cooley, James W and John W Tukey (1965). “An algorithm for the machine calculation of complex Fourier series”. In: *Mathematics of computation* 19(90), pages 297–301 (cited on page 19).
- Darwin, C. (1959). “The Gravity Field of a Particle”. In: *Proceedings of the Royal Society of London Series A* 249, pages 180–194. DOI: [10.1098/rspa.1959.0015](https://doi.org/10.1098/rspa.1959.0015) (cited on page 17).
- Gould, A. (1994). “Proper motions of MACHOs”. In: *ApJL* 421, pages L71–L74. DOI: [10.1086/187190](https://doi.org/10.1086/187190) (cited on pages 55, 56).
- Hogg, D. W. (1999). “Distance measures in cosmology”. In: *ArXiv Astrophysics e-prints*. eprint: [astro-ph/9905116](https://arxiv.org/abs/astro-ph/9905116) (cited on page 29).
- Lee, C. -H. et al. (2009). “Finite source effects in microlensing: A precise, easy to implement, fast and numerical stable formalism”. In: *Astrophys. J.* 695, pages 200–207. DOI: [10.1088/0004-637X/695/1/200](https://doi.org/10.1088/0004-637X/695/1/200). arXiv: [0901.1316 \[astro-ph.GA\]](https://arxiv.org/abs/0901.1316) (cited on pages 55–57).
- Meneghetti, M. et al. (2010). “Weighing simulated galaxy clusters using lensing and X-ray”. In: *A & A* 514, A93, A93. DOI: [10.1051/0004-6361/200913222](https://doi.org/10.1051/0004-6361/200913222). arXiv: [0912.1343](https://arxiv.org/abs/0912.1343) (cited on page 18).
- Smith, James (2015). “Bending space–time: a commentary on Dyson, Eddington and Davidson (1920) - A determination of the deflection of light by the Sun’s gravitational field”. In: 373, page 2039 (cited on page 16).

Witt, H. J. and S. Mao (1994). “Can lensed stars be regarded as pointlike for microlensing by MACHOs?” In: *ApJ* 430, pages 505–510. doi: [10.1086/174426](https://doi.org/10.1086/174426) (cited on page 55).

# A. Python tutorial

## A.1 Installation

The codes discussed as part of these lectures have been developed and run using Anaconda python 2.7 by Continuum analytics. This is just one of the python distributions available for free and we expect that the codes proposed here should run without problems with any of them.

If the reader opts for the Anaconda distribution, she/he can download the installer, which is available for Windows, Mac OSX, and Linux platforms, from <https://www.continuum.io/downloads>.

Following the installation instructions, python should be ready for usage within few minutes.

## A.2 Documentation

There are many resources online and books to learn how to program in python. The list below is just a starting point and does not want to be complete:

- the online official documentation can be found at this url: <http://www.python.org/doc>;
- several platforms for e-learning propose courses to learn python. For example, Codeacademy offers [an excellent course](#), which can be completed in only 13 hours;
- Google also offers a [python class](#) online;
- a more extensive (and practical) guide to python is given by [Learn python the hard way](#)

## A.3 Running python

Python can be run in several ways:

- from the interactive interpreter: launch "python" in a shell. Quit with Ctrl+D or type "exit()" when finished.
- create your own script with an extension ".py" and run it in a shell by typing "python <script name>.py"
- use an Interactive Development Environment (IDE). These are software which include an editor for coding and capabilities for executing the code. There are several options available (e.g. spyder, Rodeo, etc.)

- We recommend to become familiar with [jupyter notebook](#), which is increasingly popular among python users for sharing code and ideas.

## A.4 Your first python code

Try running the code:

```
# your first python code -- this is a comment
print ("Hello World!")
```

Congratulations! You have run your first python code!

## A.5 Variables

Variables are names pointing to values or objects. Setting them in python is extremely easy, and you

```
int_var = 4
float_var = 7.89778
boolean_var = True
string_var = "My name is Python"
obj_var=some_class_name(par1,par2)
```

don't need to declare them before:

## A.6 Strings

String constants can be defined in three ways:

```
single_quotes = 'my name is Python'
double_quotes = "my name is Python"
triple_quotes = """my name is Python
and this is a multiline string.""" #This can contain
```

Note that you can combine single and double quotes when you want to define strings which contain quotes themselves:

```
double_quotes1 = 'my name is "Python"'
double_quotes2 = "don't"
double_quotes3 = 'don\t'
\end{python}
```

Strings can be sliced:

you have to use backslashes:

```
\begin{minted}[bgcolor=bg]{python}
my_name='Massimo Meneghetti'
name = my_name[:7]
surname = my_name[8:]
a_piece_of_my_name=my_name[4:7]
```

You can make many operations with strings. These are objects and have many methods. Check out this url to learn more: <https://docs.python.org/2/library/stdtypes.html>

Some examples:

- String concatenation: `back_to_my_full_name=name+" "+surname`
- Convert to upper case `my_name_uppercase=back_to_my_full_name.upper()`

The built-in function `str` converts numbers to strings:

```
my_int=2
my_float=2.0
str_int=str(my_int)
str_float=str(my_float)
```

Another way to include numbers in strings:

```
my_string1 = 'My integer is %.d.' % my_int
my_string2 = 'My float is %.f.' % my_float
my_string3 = 'My float is %.3.1f (with only one decimal
```

```
a = 2
b = 67
my_string4 = '%d + %d = %d' % (a, b, a+b)

With several variables, we need to use parentheses:

a = 2
b = 67.3
my_string5 = '%d + %5.2f = %5.1f' % (a, b, a+b)

s = '23'
i = int(s)
s = '23',
i = float(s)
```

Strip spaces at beginning and end of a string: `stripped = a_string.strip()`

Replace a substring inside a string: `newstring = a_string.replace('abc', 'def')`

Important note: a Python string is "immutable". In other words, it is a constant which cannot be changed in place. All string operations create a new string. This is strange for a C developer, but it is necessary for some properties of the language. In most cases this is not a problem.

## A.7 Lists

A list is a dynamic array of any objects. It is declared with square brackets: `a_list = [1, 2, 3, 'abc', 'def']`

Lists may contain lists: `another_list = [a_list, 'abc', a_list, [1, 2, 3]]`  
that `a_list` in this case is a pointer.

Access a specific element by index (index starts at zero): `elem = a_list[2]`  
`elem2 = another_list[3][1]`

easy to test if an item is in the list: `if 'abc' in a_list:  
 print 'bingo!'`

a part of a list is called slicing: `list2 = a_list[2:4] # returns a list with items 2 and 3 (not 4)`

list operations like appending: `a_list.append('ghi')`  
`a_list.remove('abc')`

list operations: <http://docs.python.org/lib/typesseq.html>

## A.8 Tuples

A tuple is similar to a list but it is a fixed-size, immutable array. This means that once a tuple has been created, its elements may not be changed, removed, appended or inserted.

It is declared using parentheses and comma-separated values: `a_tuple = (1, 2, 3, 'abc', 'def')`  
parentheses are optional: `another_tuple = 1, 2, 3, 'abc', 'def'`  
a tuple containing only one item must be declared using a comma, else it is not considered as a tuple: `a_single_item_tuple = ('one value',)`



Tuples are not constant lists – this is a common misconception. Lists are intended to be homogeneous sequences, while tuples are heterogeneous data structures.

In some sense, tuples may be regarded as simplified structures, in which position has semantic value [e.g. (name,surname,age,height,weight)]. For this reason they are immutable, contrary to lists.

## A.9 Dictionaries

A Dictionary (or "dict") is a way to store data just like a list, but instead of using only numbers to get the data, you can use almost anything. This lets you treat a dict like it's a database for storing and organizing data.

Dictionaries are initialized using curl brackets: `person = {'name': 'Massimo', 'surname': 'Meneghetti'}`  
 can access the elements of the dictionary by using the entry keys: `person['name']`  
 keys can also be numbers: `person = {'name': 'Massimo', 'surname': 'Meneghetti', 1: 'new data'}`  
`person[1]`

## A.10 Blocks and Indentation

Blocks of code are delimited using indentation, either spaces or tabs at the beginning of lines. This will become clearer in the next sections, when loops will be introduced.

Tip: NEVER mix tabs and spaces in a script, as this could generate bugs that are very difficult to be found.

## A.11 IF / ELIF / ELSE

```
if a == 3:
    print 'The value of a is:'
    print 'a=3'

if a == 'test':
    print 'The value of a is:'
    print 'a="test"'
    test_mode = True
else:
    print 'a!="test"'
    test_mode = False
    do_something_else()

if a == 1 or a == 2:
    pass # do nothing
elif a == 3 and b > 1:
    pass
elif a==3 and not b>1:
    pass
else:
    pass
```

Here is an example of how to implement an IF/ELIF/ELSE loop:

## A.12 While loops

```
a=1
while a<10:
    print a
    a += 1
```

### A.13 For loops

```
for a in range(10):
    print a

my_list = [2, 4, 8, 16, 32]
for a in my_list:
    print a
```

### A.14 Functions

Functions can be defined in python as follows:

```
def compute_sum(arg1,arg2):
    # implement function to calculate the sum of two numbers
    res=arg1+arg2
    return(res)
```

The function can be called by typing the function name. If the function returns a value or object, this is assigned to a variable as follows:

the function can just be called without setting it equal to any variable.

```
c=3

def change_global_c(val):
    # this function change the value of global variable c
    global c
    c=val

change_global_c(10)
```

### A.15 Classes

Classes are a way to group a set of functions inside a container. These can be accessed using the . operator. The main purpose of classes is to define objects of a certain type and the corresponding methods. For example, we may want to define a class called 'square', containing the methods to compute the square properties, such as the perimeter and the area. The object is initialized by means of a "constructor":

```
class square:

    #the constructor:
    def __init__(self,side):
        self.side=side

    #area of the square:
    def area(self):
        return(self.side*self.side)

    #perimeter of the square:
    def perimeter(self):
        return(4.0*self.side)
```

can then use the class to define a square object:

```
s=square(3.0) # a square with side length 3
print s.area()
print s.perimeter()
```

As in other languages (e.g. C++), python supports inheritance. A class can be used as an argument for another class. In this case the new class will inherit the methods of the parent class. For ex-

```

class geometricalFigure(object):

    def __init__(self, name):
        self.name=name

    def getName(self):
        print 'this is a %s' % self.name

class square(geometrical_figure):

    #the constructor:
    def __init__(self,side):
        geometricalFigure.__init__(self,'square')
        self.side=side

    #area of the square:
    def area(self):
        return(self.side*self.side)

    #perimeter of the square:
    def perimeter(self):
        return(4.0*self.side)

ample:                                         In

class circle(geometrical_figure):

    #the constructor:
    def __init__(self,radius):
        geometricalFigure.__init__(self,'circle')
        self.radius=radius

    #area of the square:
    def area(self):
        return(3.141592653*self.radius**2)

    #perimeter of the square:
    def perimeter(self):
        return(2.0*self.radius*3.141592653)

s=square(3.0)
c=circle(3.0)
s.getName()
c.getName()

```

the example above, `square` and `circle` are two examples of `geometricalFigure`. They have some specialized methods to compute the area and the perimeter, but both can access the method `getName`, which belongs to `geometricalFigure`, because they have inherited it from the parent class.

## A.16 Modules

A module is a file containing Python definitions and statements (constants, functions, classes, etc). The file name is the module name with the suffix .py appended.

Modules can be imported in another script by using the `import` statement:

```
import modulename
```

The functions and statements contained in the module can be accessed using the `.` operator.

Modules can import other modules. It is customary but not required to place all import statements at the beginning of a module (or script, for that matter).

There is a variant of the import statement that imports names from a module directly into the importing module's symbol table. For example: `from modulename import something`

## A.17 Importing packages

Packages can be added to your python distribution by using either the `pip` or `easy_install` utilities. Anaconda has its own utility for installing a (limited) set of supported packages, called `conda`. To learn more, check out <https://packaging.python.org/installing/>

Packages can be used by importing modules and classes in the code as discussed above.

Some packages that we will use a lot:

- `numpy`: fundamental package for scientific computing with Python (powerful N-dimensional array object, sophisticated functions, tools for integrating C/C++ and Fortran code, useful linear algebra, Fourier transform, and random number capabilities);
- `scipy`: provides many user-friendly and efficient numerical routines such as routines for numerical integration and optimization;
- `matplotlib`: a Python 2D plotting library which produces publication quality figures in a variety of hardcopy formats and interactive environments across platforms;
- `astropy`: a community effort to develop a single core package for Astronomy in Python and foster interoperability between Python astronomy packages.

Other packages will be introduced in the examples.